Hardware and Software Studies for the Alignment of the Proton CT
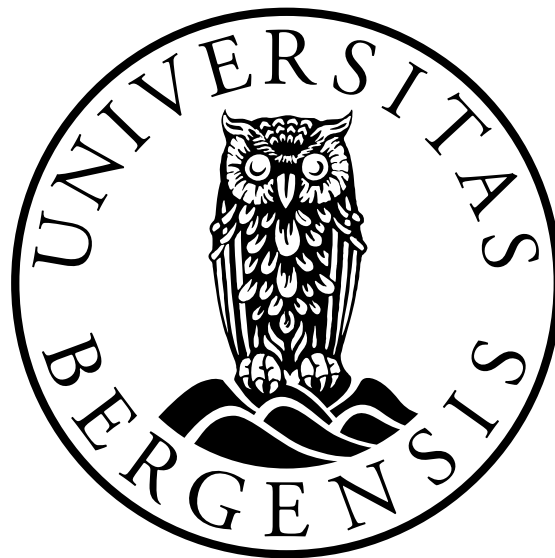
Alfred Abbasi

Supervisors:
Dieter Röhrich, Max Rauch and Matthias Richter
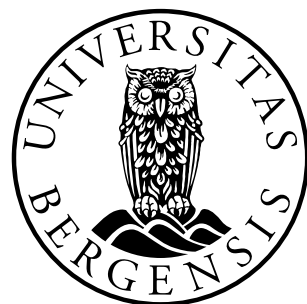
Scientific environment

This study was carried out at the Institute of Physics and Technology, Faculty of Mathematics and Natural Sciences, University of Bergen.

Acknowledgements

I would like to thank my supervisor Dieter Röhrich for making it possible for me to join the pCT team and learn a lot while doing my thesis. I would also like to thank my co-supervisors Max Rauch and Matthias Richter for helping me throughout the project with their advices and recommendations in our weekly meetings together. I would also like to thank Håvard Helstrup for his constructive criticisms which has helped me improve. Thank you all for your time and guidance.

<div align="right">

Alfred Abbasi
Bergen, 14/06/2023

</div>

Abstract

Proton therapy is a form of particle therapy using protons to irradiate tumors as a form of cancer treatment. It is becoming more and more popular around the world, including in Norway. To locate the tumor, conventional CT scan is used today, which uses x-ray beams. The proton energy deposition is then achieved by conversions that are not optimal.

Proton computed tomography has several important advantages over the conventional computed tomography. The two main advantages are giving a lower dose to the patient during imaging compared to the conventional method and eliminating the need for conversion of photon attenuation to stopping power for protons, which is a source of error. This is necessary in particle therapy, because the physical properties of photons and protons are very different. Using the same type of particles for both imaging and therapy will potentially increase the accuracy of particle therapy treatment plans. For proton CT to be possible, the detectors need to accurately detect the proton tracks and energy depositions and for that the layers of the proton detectors have to be aligned. This master's thesis is an attempt at finding a method for the purpose of alignment in a proton CT detector.

Contents

List of Figures

Chapter 1

Introduction

1.1 Motivation

In 2017, the Norwegian government decided to establish two proton therapy centers in Norway, one in the capital, Oslo, and the other one in Norway's second biggest city, Bergen [1]. In order to locate the tumor before the treatment, imaging modalities such as CT and MRI are used. The Bergen pCT collaboration is building a proton CT detector with multiple layers of sensors [2]. This thesis is a study for the alignment of the layers in a proton CT detector.

1.2 Problem Statement

Proton therapy needs a precise knowledge of the stopping power of the tissue, because protons lose most of their energy right before they are stopped in the tissue, producing a Bragg Peak which needs to be positioned in the tumor. Protons from a therapeutic proton beam enter the body and traverse some healthy tissue before reaching the tumor in which they will be stopped. Imaging modalities such as x-ray CT are used for locating the tumor before treatment. In proton CT, protons traverse the patient and scatter before reaching the detector. The first layer of the detector gives the position of the detected proton, and with two or more layers, the scattering angle of the proton can be measured as well. The scattering angle together with the position give the proton track. Proton energies are determined by how far the proton travels in the detector before it comes to a halt. To measure particle trajectories and particle energies as accurately as possible in a proton CT detector, the different layers of the detector must be aligned.

1.3 Objectives

Mechanically, it might be possible to reduce the misalignment of layers to about $100\,\mu\mathrm{m}$, but the requirement for the particle therapy and radiotherapy is there to be as little error as possible for the outgoing protons. It is not possible to achieve near perfect alignment mechanically. Aligning the layers must therefore be done through software. In a single layer, the resolution error is proportional to the pixel size, $\sigma_{res} = \frac{\text{pixel size}}{\sqrt{12}}$, which can be achieved in a perfectly aligned detector. The objective of this thesis is to

study the particle tracks traversing the layers of a prototype of the Bergen pCT detector (mTower) and the distances from the hits to the tracks (residuals). The results will be used to find the relative misalignments of these layers.

1.4 Contribution

The hardware that was used for this project was set up by other members of the Bergen proton CT collaboration, and some of the software developed by them was also used. For this thesis existing software was modified and improved which made it possible to mask the pixels in the ALPIDE sensors of the mTower at the hardware level. The most significant contribution was in the form of new software that can find tracks and residuals based on hits and clusters in the different layers of the ALPIDE sensors.

1.5 Citation principles

Citations come after a paragraph to refer to one or more statements in the previous paragraph.

1.6 Thesis outline

- Chapter 1 - Introduction - introduces the problem and the goal with the thesis

- Chapter 2 - Background and theory - briefly explains some principles in particle theory and how proton computed tomography works

- Chapter 3 - Description of hardware and software - presents the mTower and ALPIDE sensors and the test software used

- Chapter 4 - Data processing and track finding - explains how noisy pixels were detected and masked, how tracks were found, and what parameters were chosen further

- Chapter 5 - Data analysis - presents the total number of registered hits and the grouping of these hits in clusters

- Chapter 6 - Results and discussion - presents some of the tracks found by the two track finding algorithms and the offsets calculated based on the tracks found

- Chapter 7 - Conclusions and future work - summarizes the thesis and presents future work that needs to be done to achieve the goal of alignment bases on the discussion in the thesis

Chapter 2

Background

In this chapter, some physical properties of charged particles and photons will be briefly explained. The properties are important for the trajectories of the particles and the photons and their interactions with the sensors used for data acquisition. Computed tomography, proton computed tomography and the concept of misalignment will also be explained.

2.1 Charged particle energy loss and interactions

Electrons, positrons, protons and muons are charged particles. Some of their physical properties are presented and compared in this chapter.

2.1.1 Electrons

The total energy loss for electrons consists of the energy losses due to collision and the energy losses due to radiation. Electrons (and positrons) are physically different from heavy charged particles because of their size and their mass. Their trajectory changes much easier, and the particles with which they collide are usually other electrons and therefore indistinguishable from them [3].

Electrons interact with matter through the following interactions:

- Inelastic scattering with valence electrons

- Elastic collision with the atomic shell

- Elastic collision with nuclei

- Inelastic collision with nuclei

- Bremsstrahlung radiation

- Cerenkov radiation

- Transition radiation

Of these, the inelastic scattering with valence electrons dominates for low energy electrons and bremsstrahlung radiation becomes more and more important the more energy the incoming electrons have. At high energies ($> \approx 1$ GeV), bremsstrahlung is the most significant interaction of electrons with matter [3].

2.1.2 Multiple Coulomb scattering

The calculation of misalignments are based on particle trajectories and for this thesis, straight trajectories are needed which are called tracks in this document. As it was mentioned in the prior sections, charged particles interact with matter and can change their direction or energy in these interactions. Scatterings are small deflections of charged particles when passing through matter. The number of scatterings needs to be high, meaning more than 20 independent scatterings in order to be classified as Multiple Coulomb Scattering (MCS) [3], and then the problem of the electron trajectory and its deflection, can be treated by statistical means. This results in a probability distribution of the net angle of deflection [4].

The distribution of deflection angles for a large sample has a Gaussian form and the width of the Gaussian distribution for charged particles incident to the horizontal plane is given by eq.2.1 from [4]:

$$\theta_0 = \frac{13.6 \text{ MeV}}{\beta c p} z \sqrt{\frac{x}{X_0}} \left[1 + 0.038 \times ln \left(\frac{xz^2}{X_0 \beta^2} \right) \right] \tag{2.1}$$

Where p is the momentum, βc is the speed of the particle, z is the charge number of the incident particle and x/X_0 is the thickness of the scattering medium in radiation length. A radiation length is the mean distance, usually given in g/cm^2, where a high energy electron loses all but $1/e$ of its initial energy before traversing that medium through bremsstrahlung [4].

As it can be seen from eq.2.1, θ_0 is inversely proportional to both the momentum and the speed of the particle while its proportional to the charge of the particle. Since electrons are much lighter than heavy charged particles such as protons and muons (discussed in the next section), their momentum is much lower than heavy charged particles. This means that electrons have a much wider distribution of scattering angles and are therefore much less likely to follow a straight path in matter.

2.2 Heavy charged particles: charged particles that are heavier than the electron

Heavy charged particles passing through matter react with the latter in the following ways:

- Inelastic collisions with the atomic electrons of the material

- Elastic scattering from nuclei

- Other processes, which are rare:

    - Emission of Cherenkov radiation
    - Nuclear reactions
    - Bremsstrahlung

The biggest contributor of energy loss of heavy charged particles in matter is inelastic collisions with the atomic electrons of the material. The collisions cause either ionization or excitation of the matter in which the particle moves [3].

2.2.1 Protons

Protons are heavy charged particles because they are charged and much heavier than electrons. Due to inelastic collisions, a 10 MeV proton is stopped completely in 0.25 mm of copper with normal density. Elastic scatterings from nuclei are less frequent than inelastic collisions and are significant mostly when the charged particle in question is of comparable size to the nuclei of the material it is passing through. The other interactions of protons will not be discussed here because of their rarity [3] .

2.2.2 Muons

Muons are heavy charged particles. Their interactions with matter is similar to those of protons and radiative effects dominate only at rays with very high energies at several hundred GeV [5].

2.3 Stopping power of heavy charged particles

The mean stopping power of heavy charged particles is explained mainly by the Bethe-Bloch formula. In the Bethe-Bloch energy region, the mean rate of energy loss is almost entirely dependent on the β term of eq.2.2 [5]:

$$-<\frac{dE}{dx}> = K\rho\frac{Z}{A}\frac{z^2}{\beta^2}\left[ln\frac{2m_ec^2\beta^2\gamma^2W_{max}}{I^2} - 2\beta^2 - \delta - 2\frac{C}{Z}\right] \qquad (2.2)$$

Whose parameters are explained in table 2.1.

Table 2.1: *Definitions of symbols in the Bethe-Bloch formula and their units. See eq.2.2*

Symbol	Definition	Unit or value
r_e	Classical electron radius	2.817×10^{-13} cm
m_e	Electron mass	0.511 MeV/c^2
N_A	Avogadro's number	$6.0221415(10) \times 10^{23}$ 88 mol^{-1}
I	Mean excitation energy	eV
Z	Atomic number of absorber	
A	Atomic mass of absorber	g/mol
ρ	Density of absorbing material	
z	Charge of incident particle	
β	v/c	
γ	$1/\sqrt{1-\beta^2}$	
δ	Density correction	
C	Shell correction	
W_{max}	Maximum kinetic energy transfer	MeV
K	$2\pi N_A r_e^2 m_e c^2$	0.1535 MeVcm^2/g

From the Bethe-Bloch formula, it can be seen that the biggest dependence of the energy loss when a heavy charged particle passes through matter, is on the charge of the incident particle z, and β=v/c. The stopping power is proportional to the square

of the charge, while it is inversely proportional to the velocity of the charged particle. The approximations made to achieve the Bethe-Bloch formula are mostly valid for the region between the two vertical lines ($0.6 < \beta\gamma < 600$) in figure 2.1, which starts at momenta below 0.1 MeV and goes up to momenta of about 50 GeV. Before this energy range, nuclear losses dominate the energy losses and after this energy range radiation losses dominate [3].
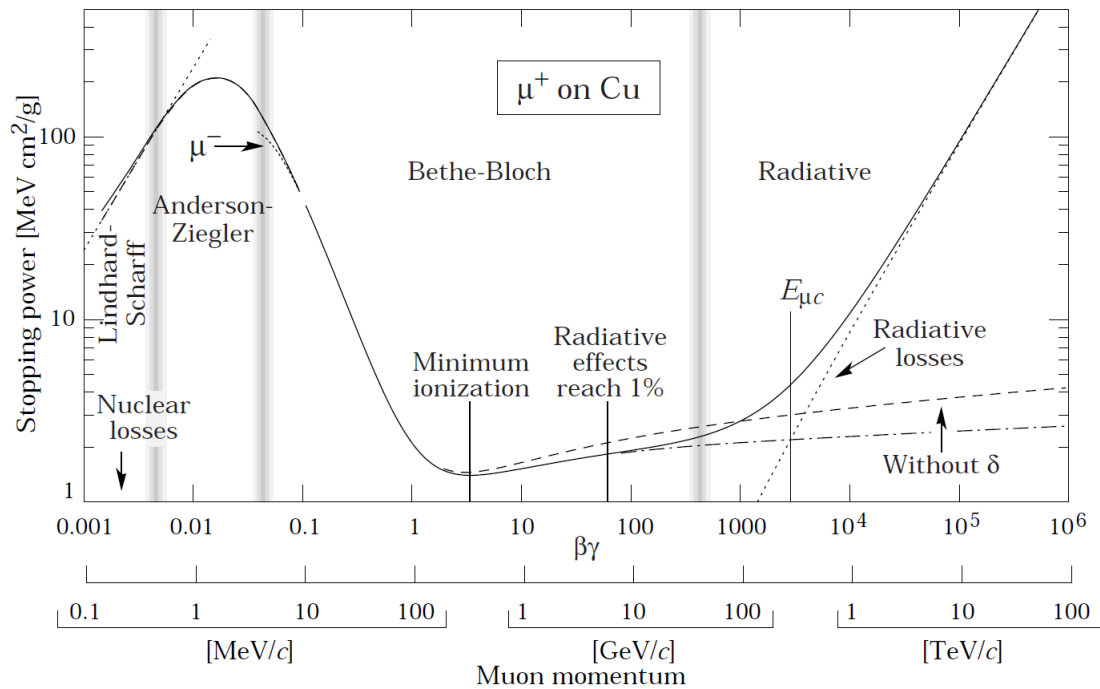
Figure 2.1: Total stopping power of muons. Figure 27.1 from [3].

Figure 2.1 shows the stopping power of a muons with muon momentum on the x-axis and stopping power on the y-axis. Below and beyond these momenta, the Bethe-Bloch equation is not enough to explain the majority of the loss of energy and other effects mentioned in the figure come into play [3] .

2.3.1 Bragg Peak

The Bragg Peak is the depth at which heavy charged particles such as protons have their maximum stopping power. The main reason for the use of particle therapy instead of the conventional radiotherapy using photons, is the difference in the dose distributions of the photons and heavy charged particles such as protons and carbon ions. Photons give more dose to the tissue surface than the tissues that are deeper for any given beam angle. To mitigate that, many dose plans with multiple angles are used to maximize the dose in the desired depth while minimizing the dose to the healthy tissues in the beam's path [6].

Figure 2.2 shows the distribution of dose in the tissue for protons vs photons at increasing depth. As it can be seen in the figure, the photons give dose to all the tissue in their path. They give much more dose to the tissues on and near the surface of the body compared to protons that completely stop at a certain range right after the Bragg Peak.
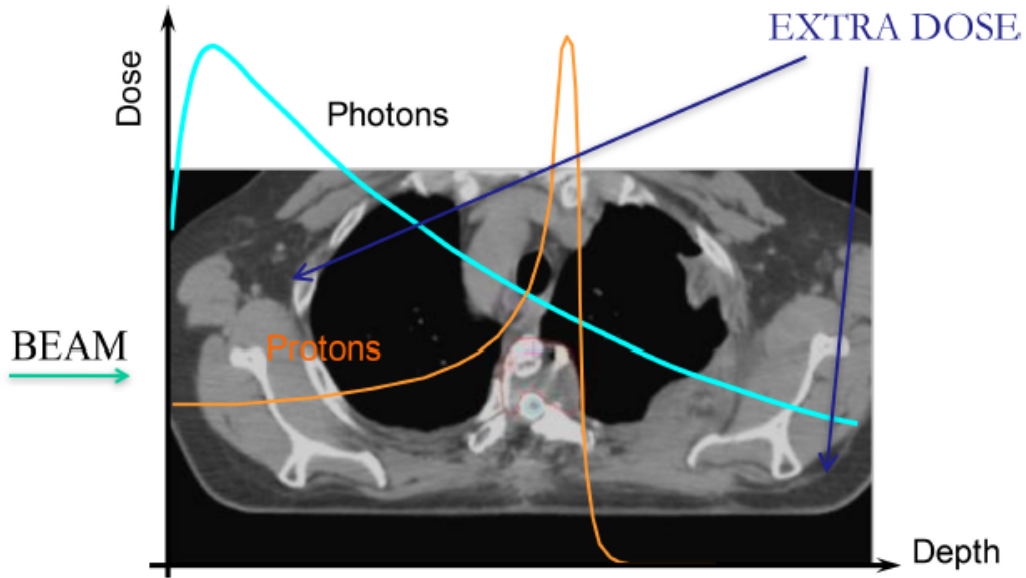
Figure 2.2: Depth-dose distribution for photons and protons. Figure 1 from [6]

Protons and heavy ions' behavior is mostly explained by the Bethe-Bloch equation (in a certain energy/momentum range see the Bethe-Bloch paragraph), with the decrease of the particle's speed, the loss of energy per unit length increases and most of the energy loss happens right before the particle is fully stopped.
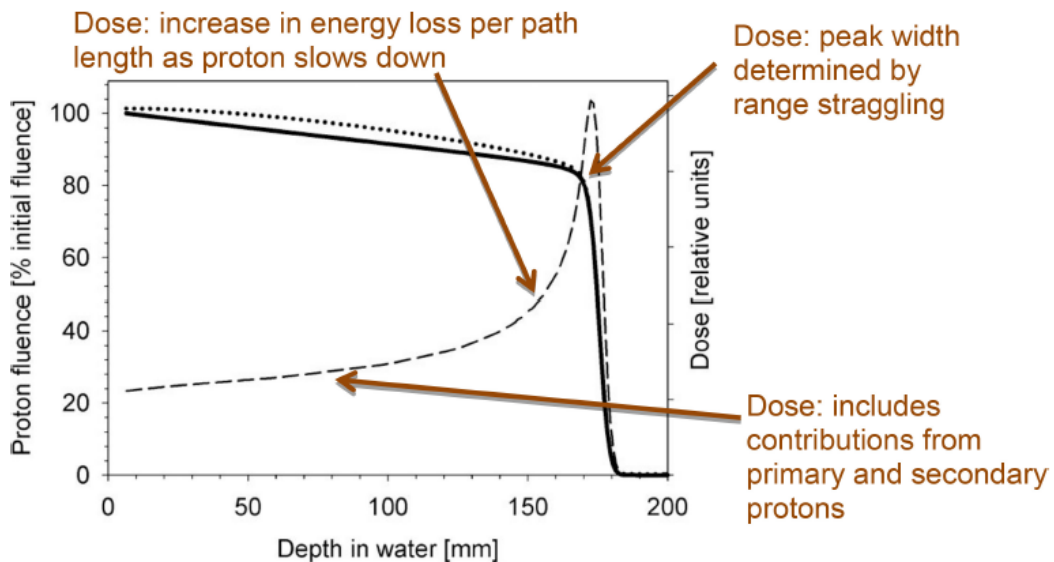
Figure 2.3: Proton flux as a function of depth in water - Figure 2 from [6]

Figure 2.3 shows a one-dimensional depth dose distribution for a 160 MeV proton beam (right axis) and the proton flux as a function of depth in water (left axis) for the same proton beam. The Bragg Peak can be seen at the depth of ≈ 175 mm.

2.4   Stopping power of electrons

To describe the stopping power of electrons, the Bethe-Bloch formula needs to be modified. The reason for this is the importance of the mass of the electron and that they are indistinguishable from each other. The latter becomes important when describing the interactions between electrons from a beam with atomic electrons. The Bethe-Bloch formula for electrons is given by eq.2.3 [3]:

$$-<\frac{dE}{dx}> = K\rho\frac{A}{Z}\frac{1}{\beta^2}\left[ln(\frac{\tau^2(\tau+2)}{2(I/m_ec^2)^2} - F(\tau) - \delta - 2\frac{C}{Z}\right] \quad (2.3)$$

Where τ is the kinetic energy of the particle in units of m_ec^2,

$$F(\tau) = 1 - \beta^2 + \frac{\frac{\tau^2}{8} - (2r+1)\ln 2}{(\tau+1)^2} \quad (2.4)$$

The rest of the variables in eq.2.3 are the same as in eq.2.2 and are explained in table 2.1. Radiation losses for electrons (and positrons) contribute more to total energy loss with increasing energy than in the case of heavy charged particles. The energy losses of electrons due to radiation and collision losses are shown in figure 2.4. The total energy loss for electrons is given by eq.2.5 [3]:

$$\left\langle\frac{dE}{dx}\right\rangle_{tot} = \left\langle\frac{dE}{dx}\right\rangle_{rad} + \left\langle\frac{dE}{dx}\right\rangle_{coll} \quad (2.5)$$

Which means that both radiation and collision losses need to be considered for electrons especially near the critical energy which is where radiation and collision losses are equal. See figure 2.4.

2.5   Range of charged particles

The range of a charged particle in matter is defined as the distance it travels in that matter before it comes to a complete stop. It is not very easy to measure the range of a single particle, because ionizations caused by the particle result in a larger signal near the exact stopping position and this results in an uncertainty of the aforementioned position in the detectors used for the measurement [7]. The general expression of range has the form shown in eq.2.6 [7]:

$$R = \int_0^R dx = \int_0^E \left(-\frac{dE}{dx}\right)^{-1} dE \quad (2.6)$$

Where dE/dx is given by eq.2.2 or eq.2.3, the Bethe-Bloch formula for the charged particle in question.

While a photon beam cannot be stopped (only its intensity attenuates exponentially), particles come to a halt when they lose all of their kinetic energy. For heavy charged particles, this happens right after the Bragg Peak. In comparison to protons, electrons undergo many more interactions while traversing matter. The range of electrons is more uncertain than protons because they undergo more interactions per unit length, but the range of electrons can still be calculated using an expression derived from eq.2.3 and eq.2.6 [3].
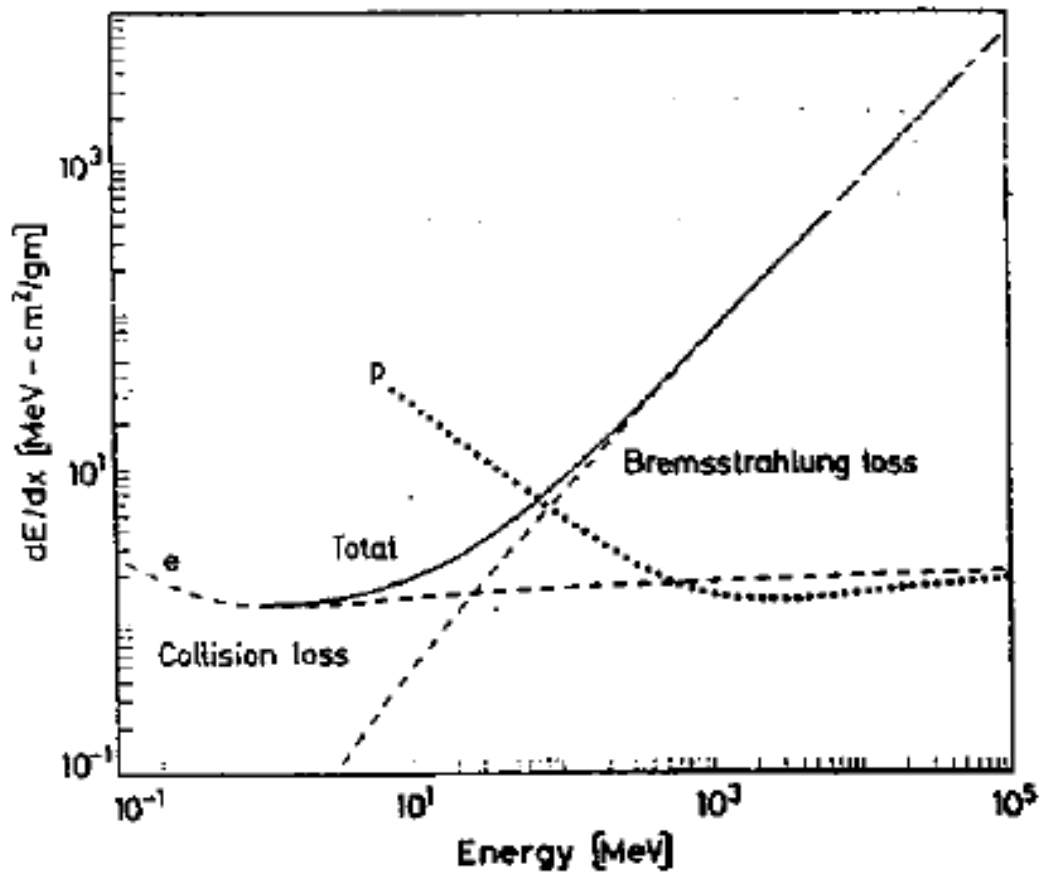
Figure 2.4: Energy loss due to collisions (dashed curve marked with e) and Bremsstrahlung (the dashed line) and sum of the two causes (the non-dashed curve) in copper as a function of energy. The dashed curve marked P shows the energy loss of protons in copper for comparison. Figure 2.10 from [3]

2.6   Radiotherapy with protons

In order to treat a tumor with protons, the protons have to first be accelerated to achieve the desired kinetic energy for the treatment. This energy is typically between 60 and 250 MeV. Three types of accelerators exist for this purpose; synchrotron, cyclotron and linac (linear accelerator). The synchrotron can change the energy of the protons in under a second, while the cyclotron usually only produces a beam of one single energy [6, 8].

In proton therapy, modulated treatment plans are widely used, such as Intensity Modulated Proton Therapy (IMPT) and these need proton beams with different energies in order to give a uniform dose to the tumor. To achieve this with cyclotrons, absorbers need to be used, but synchrotrons and linacs have the advantage of being more flexible with the energy of the protons in the beam they produce [6, 8]. Absorber materials cause the beam to widen and give a more spread out Bragg Peak (larger position uncertainty), but there are techniques that reduce this spread [6].

2.7   Radiography and computed tomography with photons

A CT scan utilizes the differences in the abilities of various tissues to absorb x-rays, as does planar x-ray radiography. In conventional computed tomography, an x-ray tube is placed on a rotating circular structure and detectors are placed on the opposite side of that circle. The patient is placed within the circle and can be moved in and out of the tunnel whose opening is the circle. The x-rays traverse the patient and are detected afterwards by the detectors. What is detected by the detectors depends on the detector configuration. It can be a line or several lines which are made into 2D images using various mathematical methods, such as back-projection. Many x-ray images are taken of the patient from different angles while the x-ray gantry (where the x-ray beams are produced) rotates around the patient and the patient is moved further into the CT scanner's tunnel. When these 2D images are put together by a computer, a 3D representation of the scanned area can be reconstructed and analyzed [9]. A CT scanner, the concept of spiral CT scan and a result of a CT scan are shown in figure 2.5.
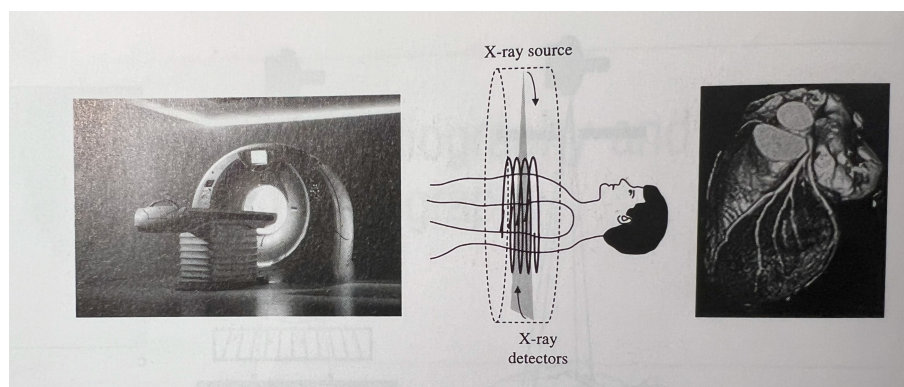
Figure 2.5: From left, a CT scanner, spiral CT scan, a CT scan of the heart. Figure 2.2 from [9].

2.8 Proton computed tomography

Proton Computed Tomography (pCT) gives similar results as Computed Tomography (CT) using photons. It also results in a 3D representation of the scanned area of the body by combining image slices. The biggest difference is that in pCT, protons and in conventional CT, photons are used, which have very different physical properties [10]. Photon beams give the highest dose to the first tissue they encounter, but protons give their highest dose at a certain depth according to the Bethe-Bloch formula and their Bragg Peak which is located outside the body and inside the detector. This allows for lower dose to the patient while conducting a pCT scan compared to conventional CT [10]. A design for a pCT system with four tracking layers (PSDs) and a Residual Energy Range Detector (RERD) is shown in figure 2.6. If the proton beam has a very well defined range of energy and angle, the first two tracking layers may not be necessary [10].
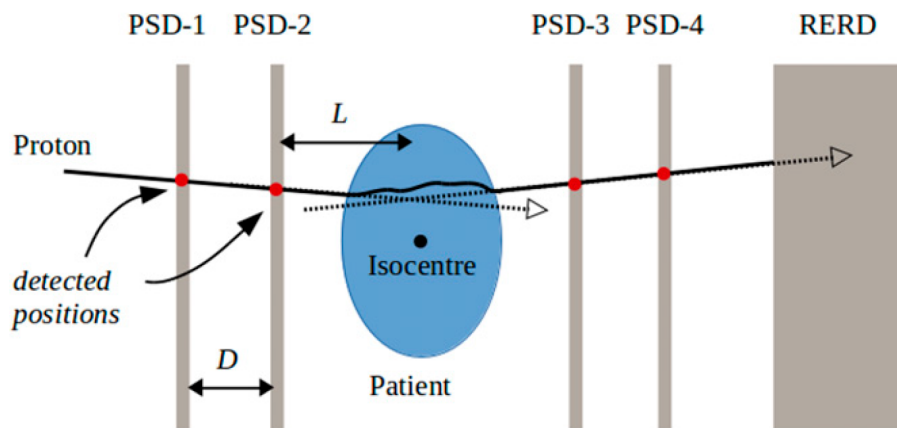
Figure 2.6: This is an example of a proton CT setup, where there are two tracking detectors (PSD-1 and PSD-2) before the patient and two after (PSD-3 and PSD-4) before the protons reach the calorimeter (PERD) on the right. Figure 5 from [10].

Bergen pCT

The Bergen proton CT collaboration project aims to make a scanner with which it is possible to image the human anatomy in order to improve the accuracy of proton therapy treatment plans with removing the conversion need from conventional CT images to proton dose distribution. At the same time, the project needs to make this prototype scanner's image reconstruction fast. The image reconstruction methods used in such imaging modality need high precision in order to construct images with acceptable resolution [2]. Proton beams of high energy are used, and they will therefore penetrate matter and go quite far inside the detector layers while losing their kinetic energy until they eventually stop. What is needed for the image reconstruction is the path taken through the detector by each proton that enters and also the energy deposition of said proton. Both are done by the same device which is a Digital Tracking Calorimeter (DTC) [2]. The working of the DTC is as follows, first tracks of protons are detected, that is straight lines going through the detector which has 41 layers of monolithic pixel sensors (ALPIDE chips) with absorber layers between them. Each layer is made up of

many ALPIDE chips, which are first arranged in strings of 9 chips (STAVEs) and then several STAVEs that are vertically arranged, make a layer. Each ALPIDE chip has 1024 x 512 pixels which record the deposition of energy over a given threshold, this number of pixels in each layer makes it possible to detect several protons at the same time and since track information and energy deposition are all done by the same device, the cost and time needed for the imaging is reduced [2].
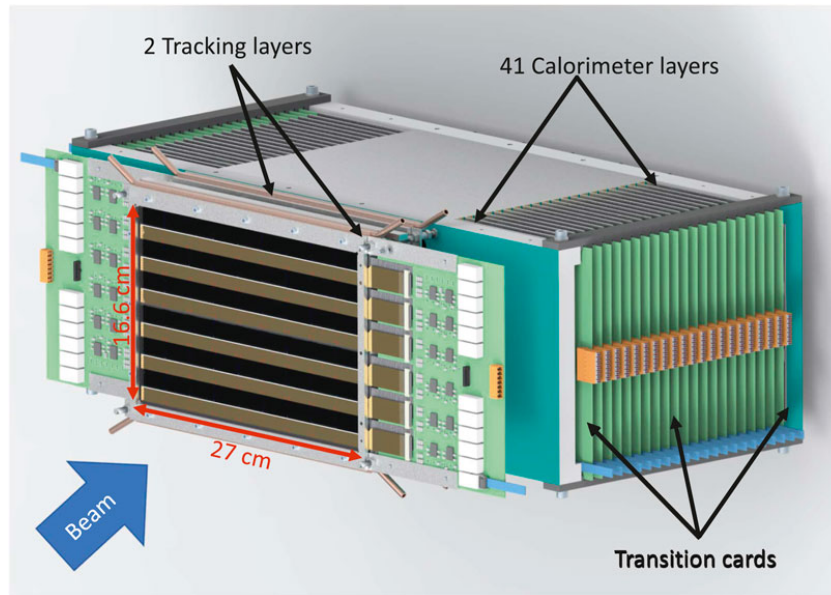
Figure 2.7: Bergen pCT collaboration's scanner design. The covers are removed on one side to allow viewing of the inner parts, such as a layer of ALPIDEs to be visible. Figure 2 from [2].

In order to reduce multiple Coulomb scatterings, the two first layers are made out of ultra-thin carbon fiber sheets [2]. A sketch of the scanner with its dimensions is shown in figure 2.7.
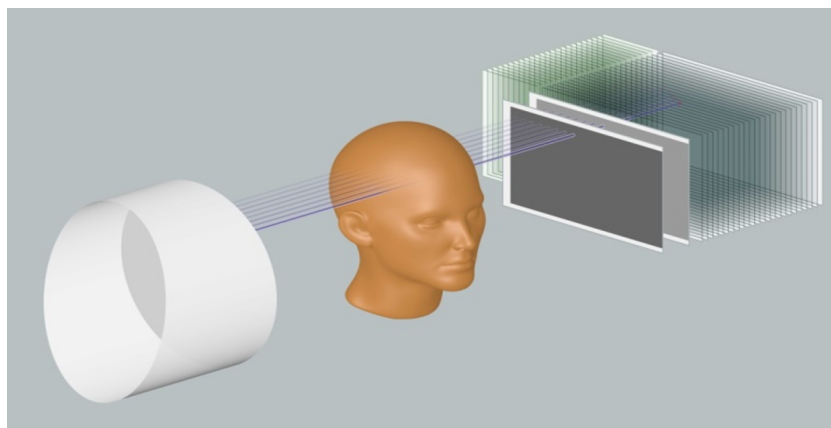
Figure 2.8: the concept of proton computed tomography. The beam enters the phantom/patient's head, traverses it and then leaves the phantom to then enter the detector and be slowed down until it stops in one of the layers of the detector. The figure is from [11].

The concept of the pCT scanner from the Bergen pCT collaboration is different from figure 2.6 in that the tracking of protons does not start before the protons have traversed the patient (phantom in the sketch) as it can be seen in figure 2.8.

While for one chip, it's possible to achieve sub-millimeter precision, because of how the chips are put together, these layers cannot be perfectly aligned mechanically with a precision of 29.24 and 26.88 µm which are the dimensions of a pixel in an ALPIDE chip [2, 12]. Software must therefore be used to adjust the different layers after the misalignments are found.

2.9 Misalignment

The goal of this thesis is to study the alignment of layers of sensors in a proton CT detector. It is therefore crucial to define what alignment and misalignments are.

The problem of alignment is about coordinate systems that are not in agreement with each other. In a detector such as the one being made by the Bergen pCT collaboration, there are many sensors which have their own coordinate systems. These chips are mounted next to each other in a single layer (xy plane) and these layers on mounted with the same distance between each two layers (z direction), it can be assumed that the assembly can be fairly consistent with the distance between the sensors in the same layer. The bigger problem is in the direction incident to the layer planes (z direction). Figure 2.9 shows a detector with misaligned sensors registering hits from a particle track and a global coordinate system outside of the sensors.
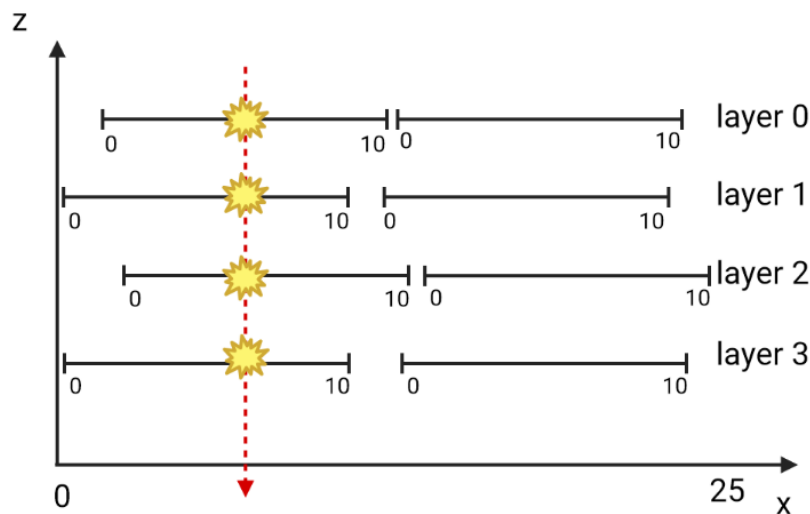
Figure 2.9: A sketch of a misaligned multi-layer detector registering hits from a particle traversing it (red dotted line). The distances are exaggerated.

As it can be seen in figure 2.9, the distances between the sensors in each layer is not consistent with the next. The left side of the layers also have different distances to the z-axis. When the hits are plotted, data is taken from the local coordinate systems of the sensors and an attempt to reconstruct the track is made in the global coordinate system outside of the sensors. The result of this would be a plot as the one shown in figure 2.10, where the hits can no longer make a straight line.

If the distances from the sensors to the z axis and the distance between all the layers in the z direction, were to be found accurately, in the reconstruction of the track, the hits from the sensors could be adjusted to represent their true spatial position. For example,
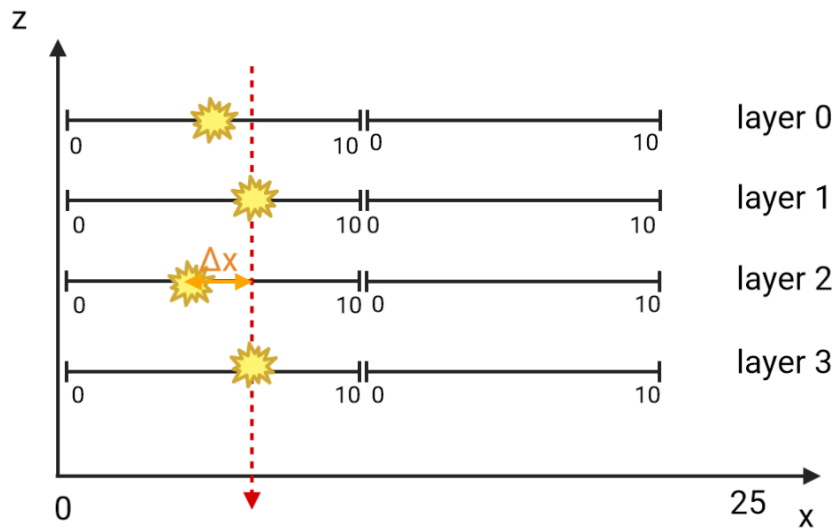
Figure 2.10: A sketch of the representation of hits from a track (red dotted line) in a misaligned multi-layer detector. The distances are exaggerated.

all the hits on the left side of layer 2, would be added a value Δx so that the hit in layer 2, shown in figure 2.10, would be placed on the track to the right of it, and that it would represent its true spatial position in the detector. If the hit was positioned to the right of the track in the reconstruction, a negative value for Δx had to be added to the hits in that layer to push the hit to the left. The distance from the hit to the track is referred to as residual and the value with which each layer needs to be shifted so that all the layers are aligned, is referred to as the offset.

Chapter 3

Hardware and software

In this chapter the relevant technologies to the thesis and the setup used to acquire data is explained.

3.1   Description of the experiment setup

The results of this thesis were achieved using a setup, consisting a telescope of sensors sensitive to radiation, and other equipment used for powering the sensors and reading the data from them. The different parts of the telescope, especially the sensors, are explained in more detail in the following sections of this chapter.

3.2   mTower

The pCT DTC was not ready at the time of writing this thesis, instead a telescope of four layers, each with two ALPIDE chips was used for this thesis. In the last layer, a bug in the ALPIDE chip with ID 7 caused it to broadcast to all ALPIDEs in the setup. To avoid this from happening, since it would reset the settings for all the other ALPIDEs, this ALPIDE chip was not used. The layers are shown in figures 3.6-3.7, where chip ID 7 was never used due to the bug mentioned above and only the half with chip ID 6 was functional in layer 3. These layers of ALPIDE are connected to a PCB transition card which is also shown in figure 3.6. The transition card itself is connected to the Xilinx VCU118 Evaluation board. The evaluation board is connected to the power supply, and a computer which controls the setup through software (see section 3.4). In figures 3.1, 3.6 and 3.7, there are two additional layers, but the setup can only handle four layers at a time with a single FireFly cable (the blue cable in figure 3.1) , so those two additional layers were not used.

   The components of the test setup are listed in table 3.1 and the mTower, transition card, evaluation board and power supply are shown in figures 3.1, 3.3, 3.4 and 3.5. The table also refers to some documentation for the parts of the setups where this was possible.

   The sketches in figures 3.2a and 3.2b show the layers of the mTower setup together with its dimensions and pixel numbering conventions (x and y values). The figures are not to scale. In order to make the correct representation of the hits in the ALPIDEs, the

Table 3.1: The components of the test setup

Name	Description	Documentation
mTower	Telescope of ALPIDEs	Similar setup [13]
PC	Running CentOS 7 (64-bit)	
mTower transition card	See figure 3.3	
Evaluation board	Xilinx VCU118	Data sheet [14]
Power supply	TTi QL355TP	Data sheet [15]
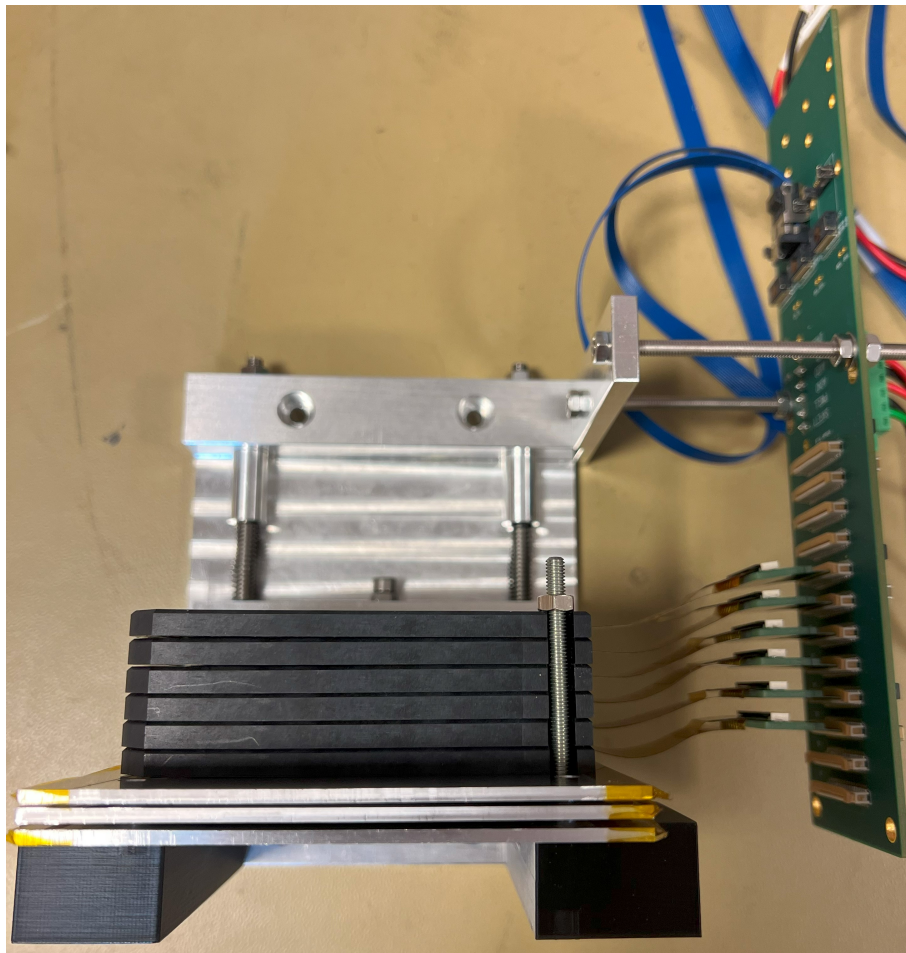
Figure 3.1: mTower in horisontal position

pixel numbering and layers had to be taken into account. For example, y values in the plots that represent the hits, go from 0 to 1023.
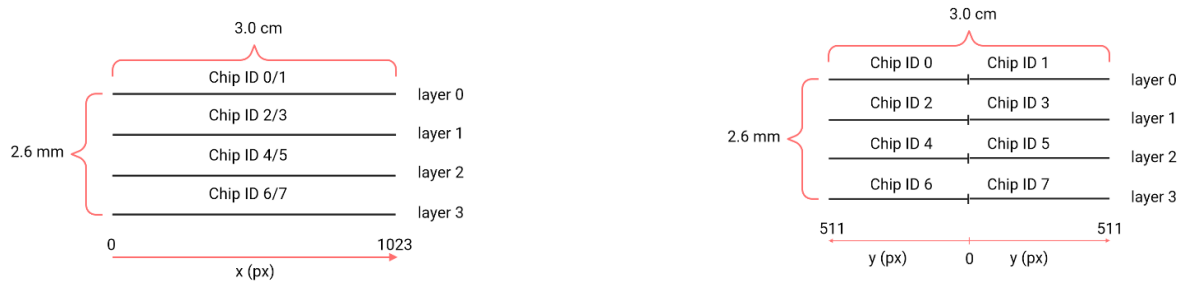
(a) Sketch of the mTower showing the column side (x) of the ALPIDEs. Not to scale.

(b) Sketch of the mTower showing the row side (y) of the ALPIDEs.

Figure 3.2: Sketches of the mTower. Not to scale.

3.3 The sensor

In this section, a brief explanation of the P-N junction and Monolithic Active Pixel Sensors is given. After that the ALPIDE sensor, which is the central part of the mTower is explained in more detail.

3.3.1 P-N junction

A negatively doped and a positively doped semiconductor (n-type and p-type for short) can be made into a diode. Since the n-type semiconductor has free electrons and the p-type one has free holes and the concentration of both electron and holes are different in the two semiconductors, the electrons will diffuse into the p-type region and recombine with the closest holes in the p-type region, and the holes will diffuse into the n-type region where they recombine with the closest free electrons, as soon as the two semiconductors come into contact [17]. This is shown in figure 3.8 .

At the junction of the two semiconductors, the n-type part becomes positively charged and the p-type one will become negatively charged. This generates an electric field across the junction which is known as the depletion zone because it is depleted of free charge carriers [17]. The depletion zone can be seen in figure 3.9.

3.3.2 Monolithic active pixel sensors

Monolithic Active Pixel Sensors (MAPS) are a type of silicon pixel detectors that combine the sensor and the electronics in one single unit, which avoids issues with connections. These sensors have low power consumption, high speed and high radiation resistance and have the advantage of reducing capacitance of each pixel, which reduces noise. MAPS are "active" because there is an amplifier in each of the pixels of this type [19].

Figure 3.10 is an illustration that shows how charge is collected in a monolithic active pixel sensor. The epitaxial layer is the active part of the detector. The depletion zone is shown in white. The electric field is not strong in most of the epitaxial
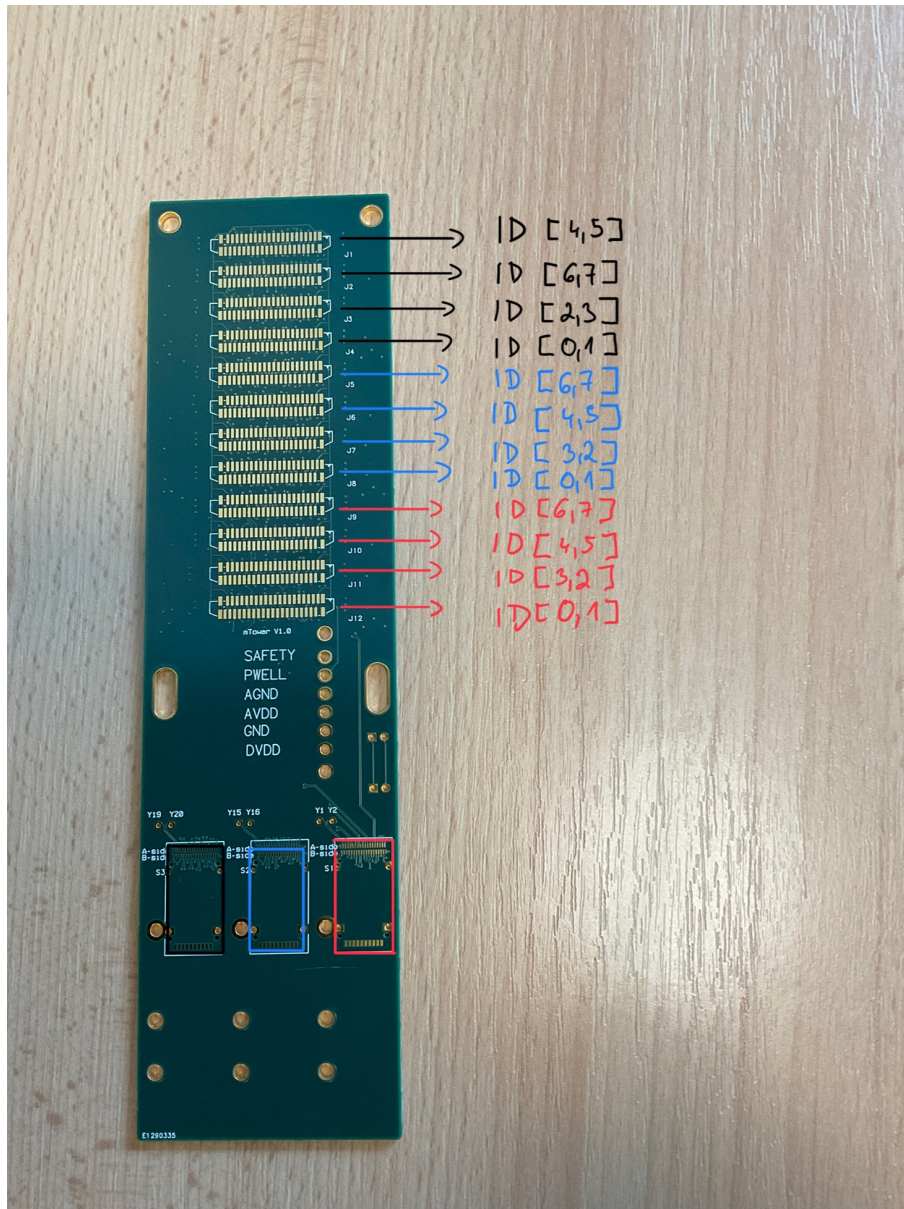
Figure 3.3: mTower transition card detached from the rest of the mTower. Each set of chip IDs (represented by the same color) needs a dedicated FireFly cable. The correct representation of chip ID positions is given in 3.2b. Figure from [16].
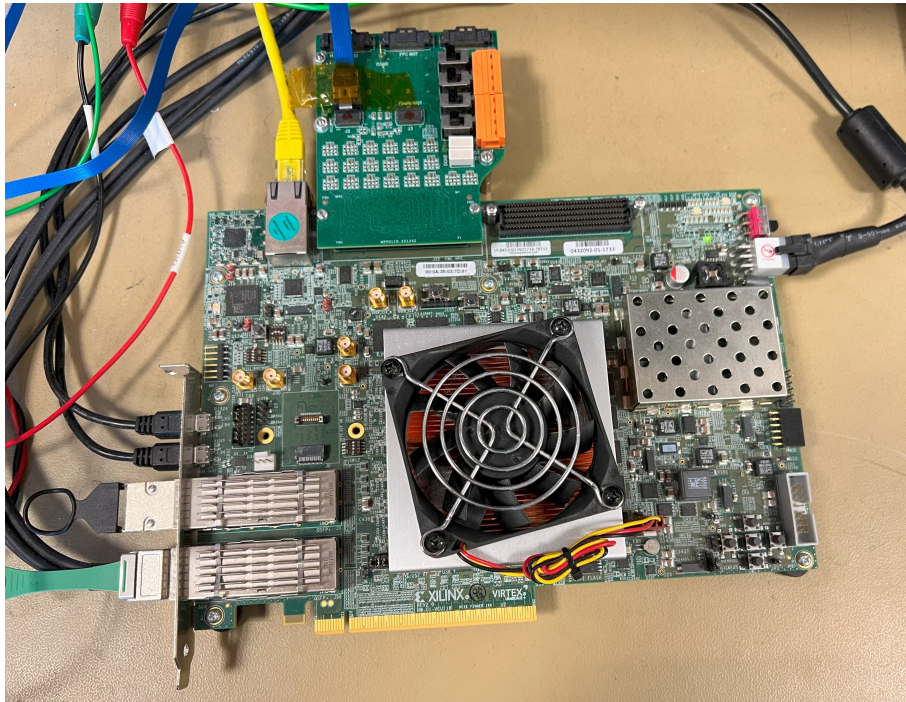
Figure 3.4: VCU118 Evaluation Kit
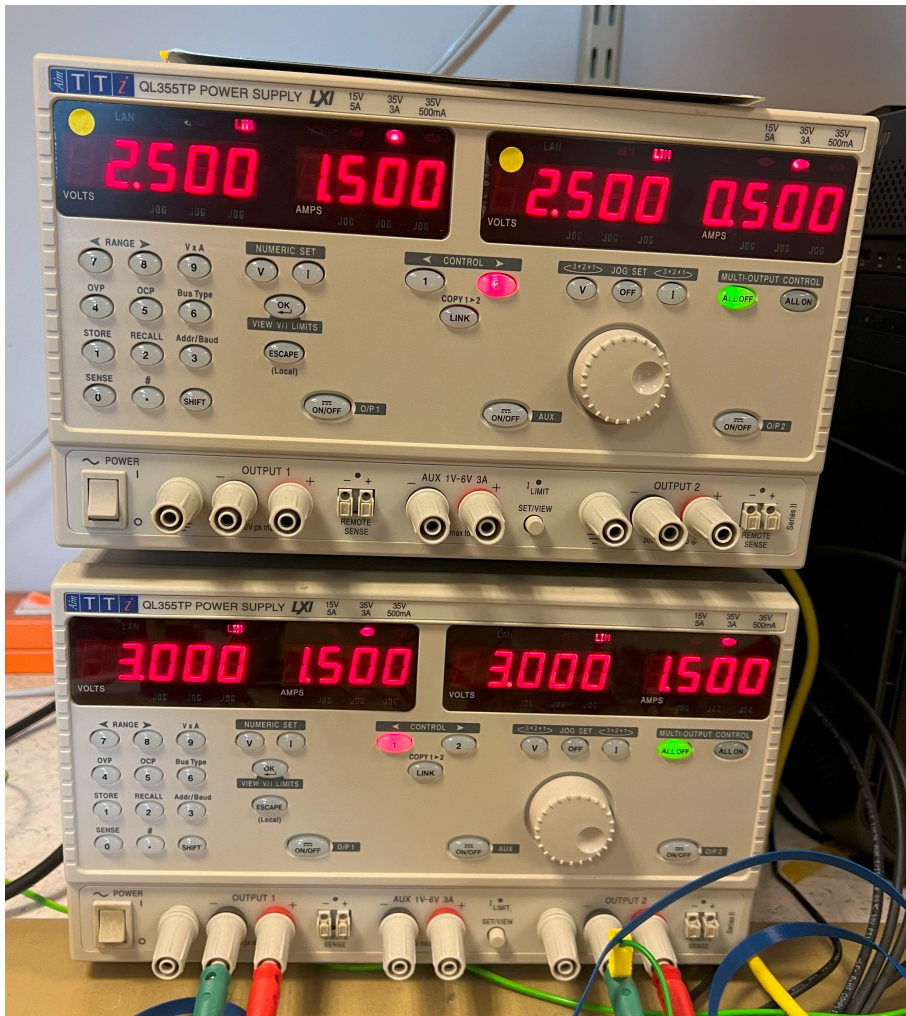
Figure 3.5: Two TTi QL355TP Power Supplies (only the bottom one was used)
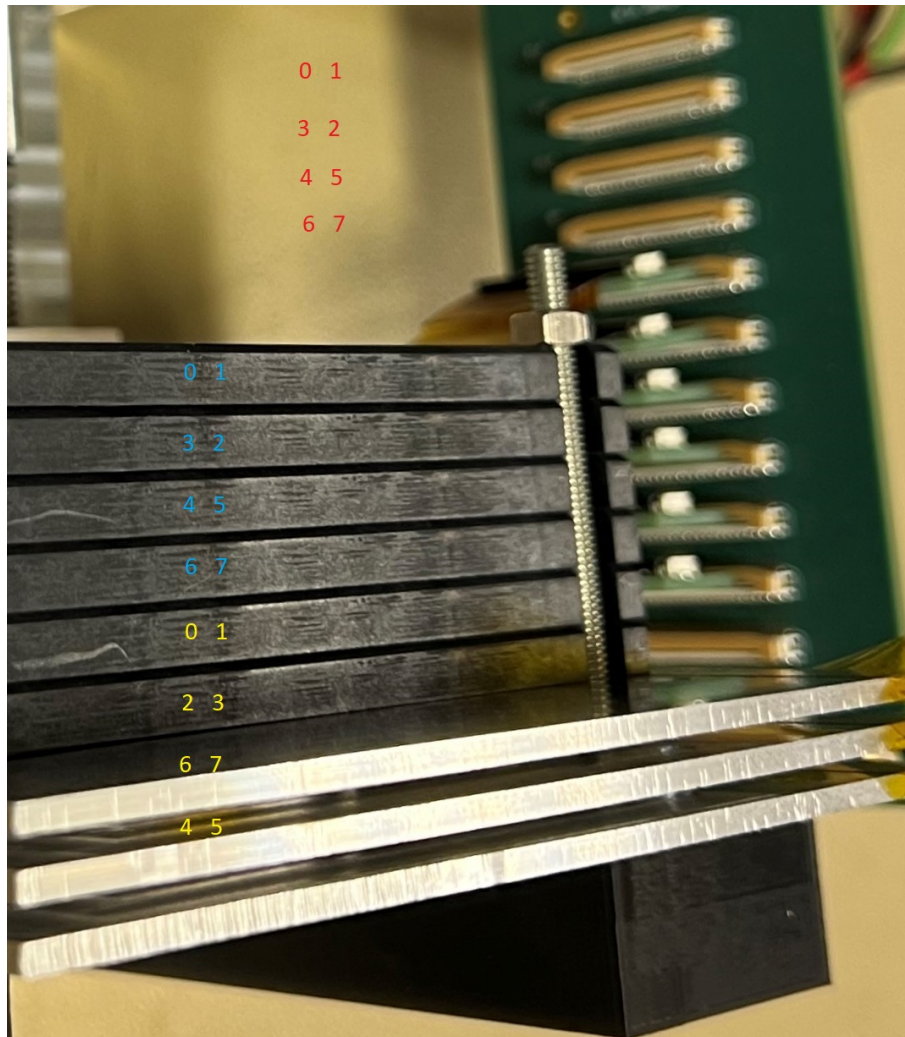
Figure 3.6: The chipIDs in the four layers of ALPIDE chips in the mTower. Only the ones in blue were used after 25th of January 2023. The correct representation of chip ID positions is given in 3.2b
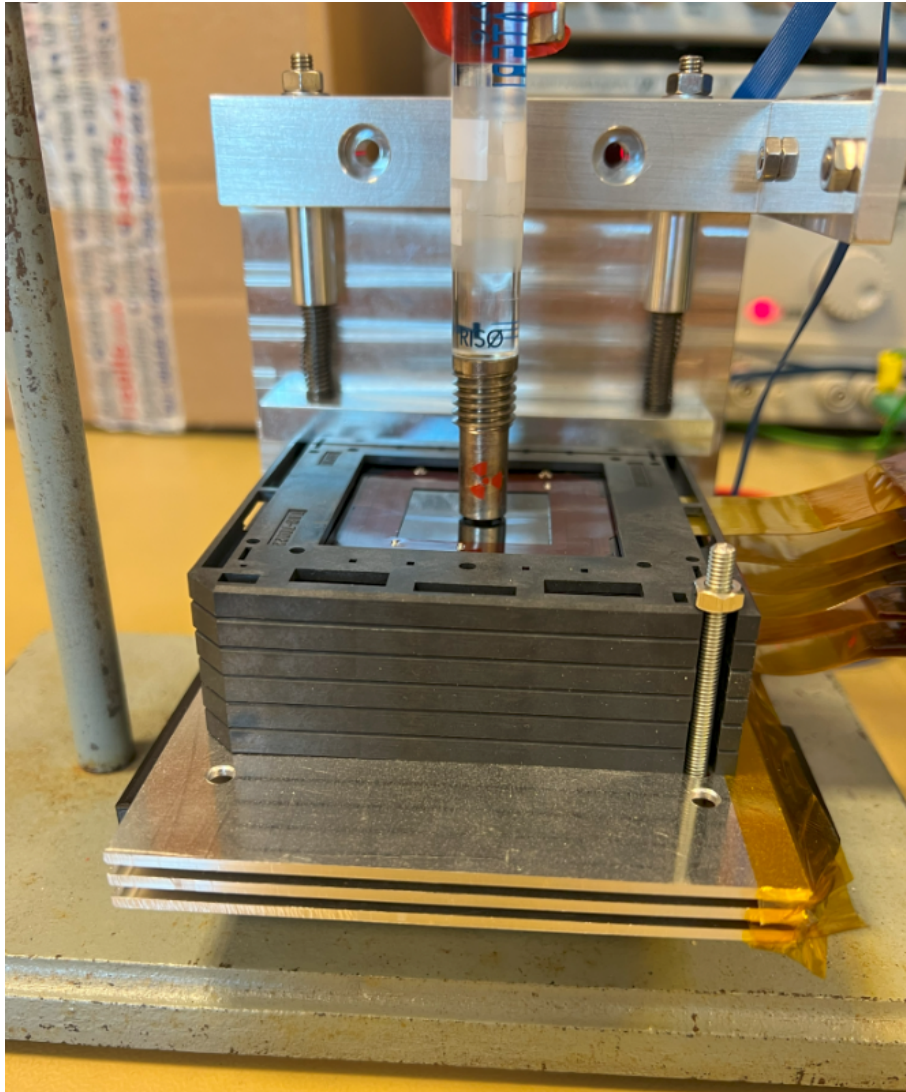
Figure 3.7: The mTower with the Strontium 90 source at a distance of ca. 1 mm from layer 0
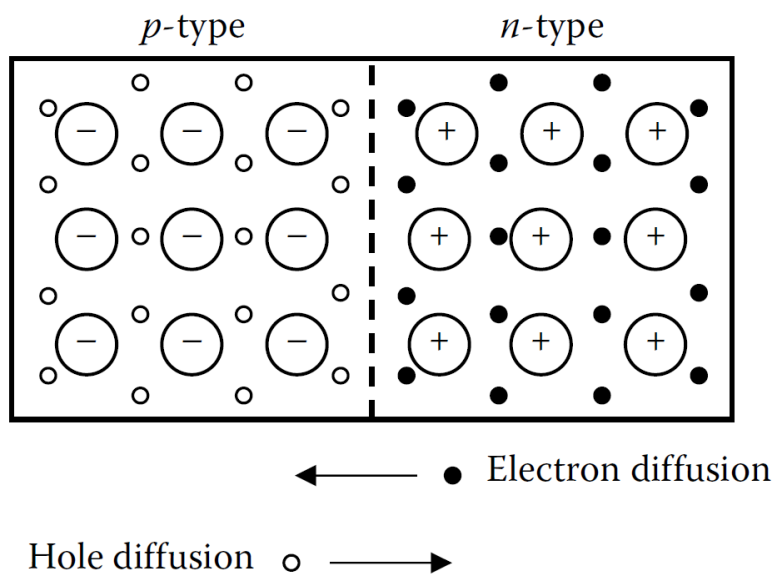
Figure 3.8: Schematic of a PN-junction. Figure 3.1.1 from [17]
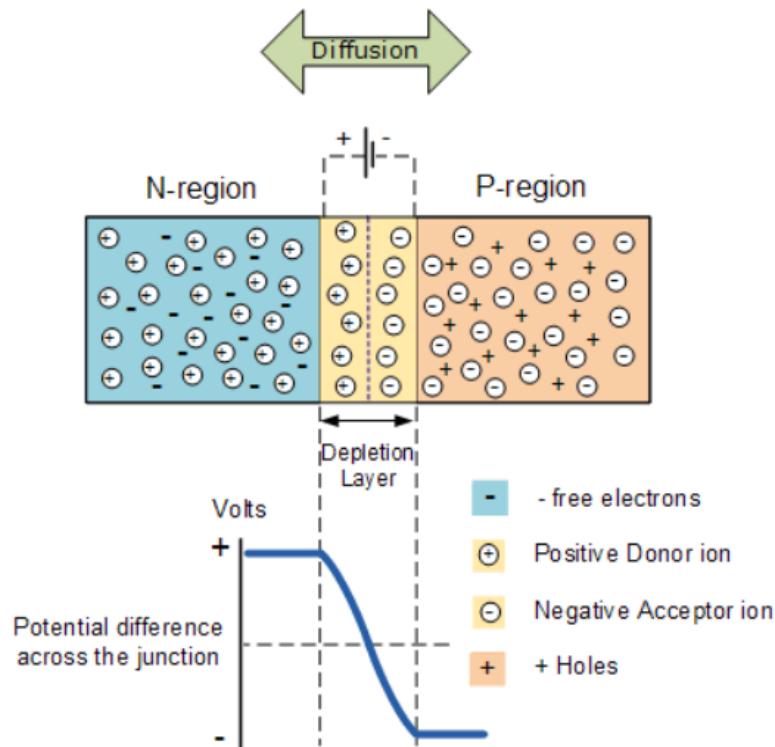
Figure 3.9: Illustration showing the depletion zone and the electric field (potential difference) across a P-N junction. Retrieved from [18].

layer, because of this, charge carriers (electrons and holes) reach the collection diodes, established by the p-type/n-well epitaxial layer junction, by thermal diffusion [20].

3.3.3 Clusters

A cluster is a group of pixels that registers the same particle, even though the particle is smaller than a single pixel. The reason for this is the diffusion of charge from one pixel to another [22].

Clusters can vary in size, for example if a particle passes between two pixels of the pixel detector, the charge will be shared among them resulting in one hit for each of the pixels and a particle passing near the corner of a pixel, results in four pixels registering a hit each [20].

The cluster size varies with charge threshold settings for the detector, lowering it results in more hits being registered and therefore bigger clusters. Cluster centers are the most likely position at which the ionizing particle that caused the cluster passed through, as it can be seen from the figures showing cluster formation in [23].

An elongated cluster from the beta emitting source, Strontium-90 is shown in figure 3.11. The elongated shape indicates that the electron did not come directly from above the firing pixels of the ALPIDE chip it hit, and several pixels were ionized by the particle itself, which formed a line from which the charge spread to other pixels. Another cluster from cosmic muons is shown in figure 3.12. The muon most likely hit the middle of the cluster and the charge spread to the other pixels that registered the hit afterwards.
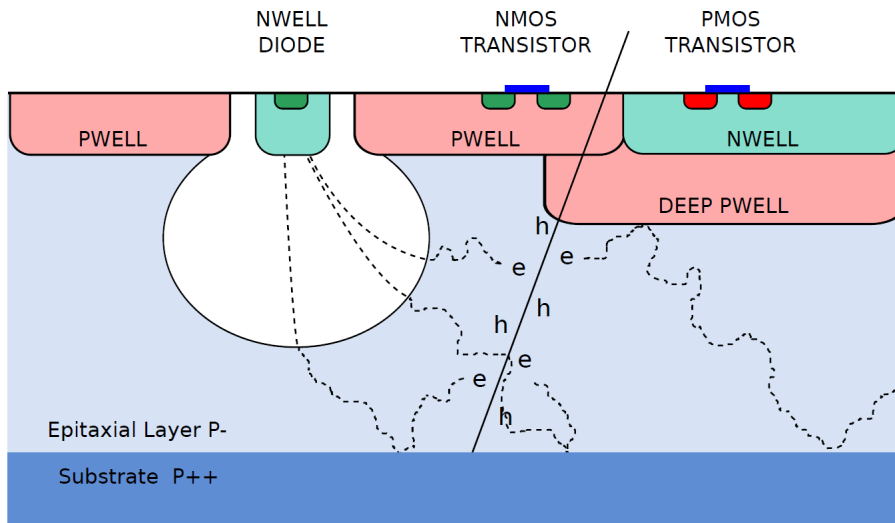
Figure 3.10: Illustration that shows the cross section of a MAPS pixel in the TowerJazz 0.18 µm imaging CMOS with the deep p-well feature. Figure 2.2 from [21].
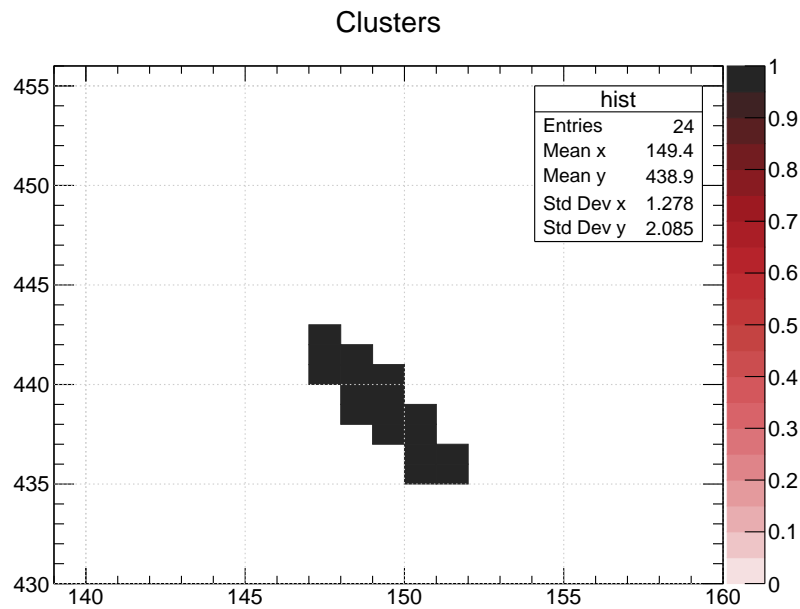
Figure 3.11: A single cluster from data taken with the Strontium-90 beta emitter source.
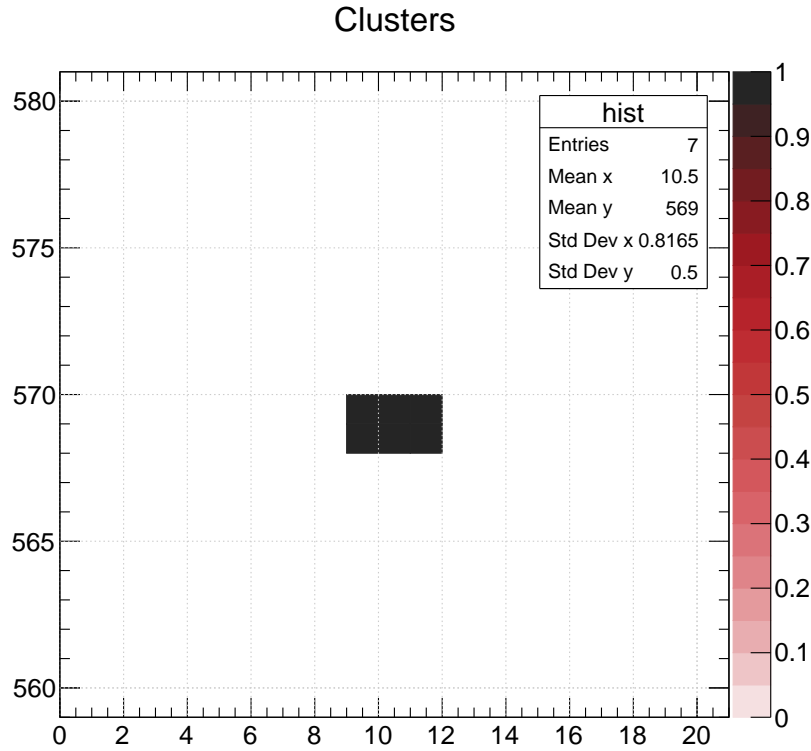
Clusters

Figure 3.12: A single cluster from data taken with cosmic rays.

3.3.4   The ALICE pixel detector

The ALICE Pixel Detector (the ALPIDE chip) is a high granularity (many pixels) Monolithic Active Pixel Sensor (MAPS) developed for the upgrade of the Inner Tracking System (ITS) for the ALICE (A Large Hadron Collider Experiment) at CERN and it was built using Complementary Metal-Oxide- Semiconductor (CMOS) technology [24].

After testing several chip designs the ALPIDE chip was chosen for the upgrade since it passed the requirements of having a detection efficiency of more than 99%, a special resolution of 5 µm and a fake hit probability of less than 10^{-5} [25].

Detection of ionizing radiation, both from muons and electrons was performed by the ALPIDE chip for this thesis. The ALPIDE chip's specifications are given in table 3.2 [12].

Table 3.2: specifications of the ALPIDE chip [12]

Variable	Value
Thickness [26]	50 µm
Length (along x-axis)	30 mm
Width (along y-axis)	15 mm
Pixel dimension x (column)	29.24 µm
Pixel dimension y (row)	26.88 µm
Number of pixels in x direction	1024
Number of pixels in y direction	512

3.3.5 ALPIDE architecture

The 512x1024 pixel matrix of the ALPIDE chip is divided into 32 read-out regions. Each of these contains 16 double columns and each double column has a priority encoder in the middle of it [12]. The periphery circuit region of the chip is located below the last row of pixels on the bottom. It includes readout and control and it measures 1.2 mm x 30 mm [12]. The columns and rows of the ALPIDE chip are referred to as x and y, respectively, as shown in in 3.2 and schematic of them with the periphery circuit region is shown in figure 3.13.
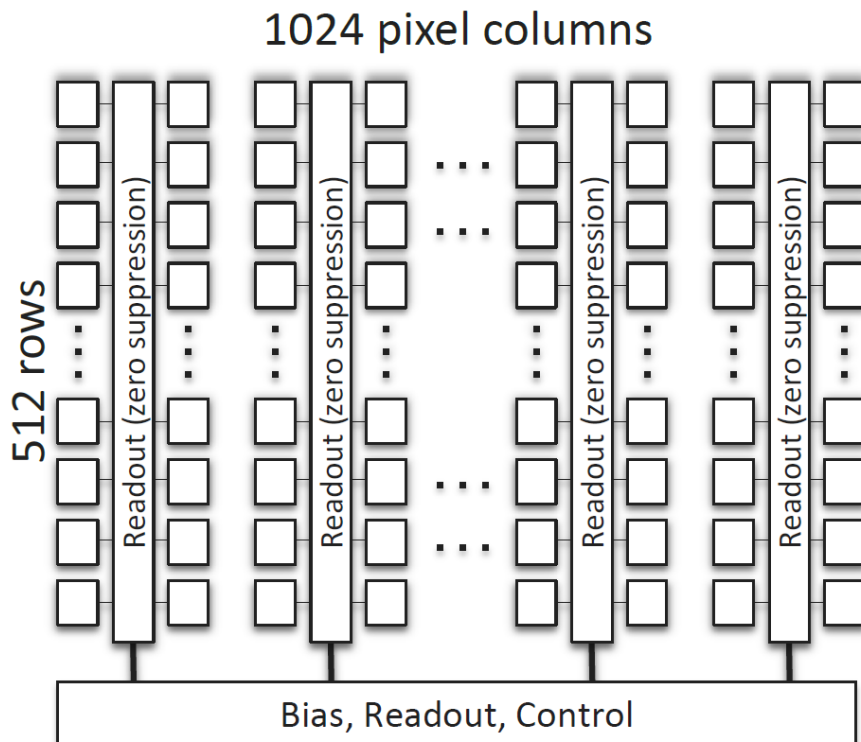
Figure 3.13: Schematic of the architecture of the ALPIDE chip. Figure 1.1 from [12].

3.3.6 Operation modes of ALPIDE

The ALPIDE can be operated in several modes, which can handle different amounts of data. For the experiments in this thesis and for pCT, the Inner Barrel Mode is used, which is the mode that can handle the largest rate of data [23].

In the ALPIDE chip, each pixel contains the following:

- a sensing diode

- a front-end amplifying stage

- a front-end shaping stage

- a discriminator

- a digital section

The front-end and the discriminator are continuously active. The digital section is where the three hit storage registers (Multi Event Buffer), a pixel masking register and pulsing logic are located. The peaking time (the time for the signal to build up to its maximum value) of the front-end is about $2\,\mu s$ and the discriminated pulse's duration is typically $10\,\mu s$ [12]. A block diagram for a pixel cell is shown in figure 3.14.
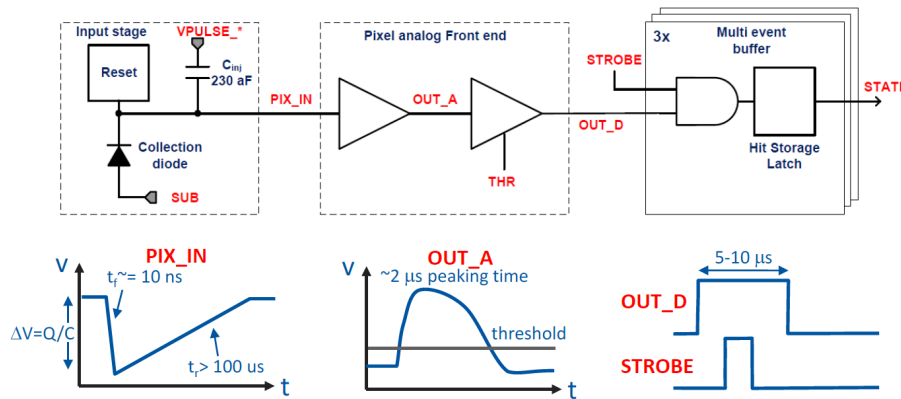
Figure 3.14: *block diagram for a pixel cell in an ALPIDE chip. Figure 1.2 from [12].*

A common threshold level is applied to all the pixels. The latching of the discriminated hits in the storage registers are controlled by the global STROBE signals. In order for a pixel hit to latch into one of the three in-pixel memory cells, a STROBE pulse needs to be applied to that cell while the front-end output is above the threshold level. At the periphery, three distinct STROBE signals are generated and applied globally to all pixels. These control the storage of pixel hit information in the pixel event buffers [12].

Each pixel contains a Mask and a Pulse Enable register. The Mask register can reduce the digital output of the pixel by making the read-out skip the pixel and not appear in event frames. The Pulse Enable registers are used to enable test pulsing functionalities. Through analog pulsing, a hit can be forced by using a test charge injection capacitor or through digital pulsing which is done by directly setting the pixel state register [12].

3.3.7 Triggering and framing

A frame contains the states of all the pixels at a particular time. A frame is generated after a TRIGGER is received. Since the ALPIDE pixels all have a Multi Event Buffer (MEB), three distinct in-pixel storage elements, they can store three full-frames without the completion of the full matrix read-out and without the loss of any data [12].

Writing and reading of frames is based on the management of the aforementioned MEBs in the chip pixels. The Framing and Management Unit (FROMU) manages the MEBs and the frames [12]. The management scheme is shown in figure 3.15.

Three global signals, distributed to all pixels from the periphery, control the recording of the pixel discriminator outputs in the storage registers. An internally or externally generated TRIGGER initiates the timed assertions of the STROBE signals. The output of the latches in the pixels, belonging to one bank of registers at a time, can be connected to the Priority Encoder. This is controlled by three global signals (MEMSEL).
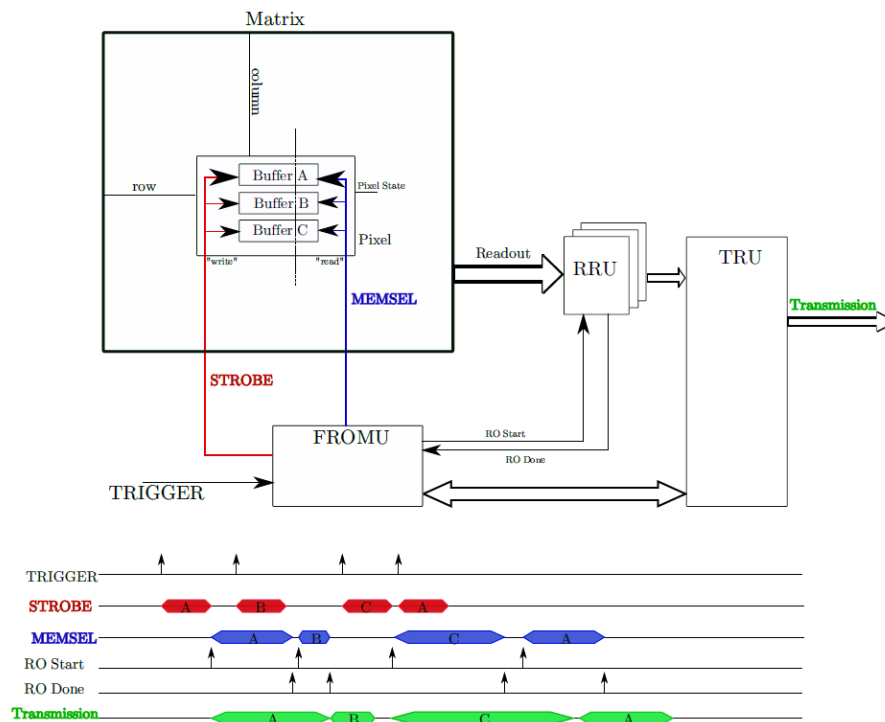
Figure 3.15: The management scheme of MEBs by the Framing and Management Unit [12].

STROBE and MEMSEL signals are the write and read signals, respectively and they are controlled by the FROMU [12].

The readout of a pixel buffer starts at the end of the corresponding STROBE assertion with the MEMSEL signal. The 32 matrix regions are read out at the same time by 32 Region Read-out Units (RRUs). Each RRU stores the data in local memories. The Top Read-out Unit (TRU) is responsible for fetching the information from each RRU and transmitting it off the chip. The ALPIDE gives the possibility for two MEB management schemes, called read-out modes, which are the triggered and continuous modes [12].

3.3.8 Read-out Modes

The two read-out modes or MEB management schemes for the ALPIDE are as follows:

The triggered mode uses very short strobe windows, the time between two STROBE signals (a few hundredths of nanoseconds), and is intended to sample over a relatively short interval of time. The trigger mode prioritizes read-out over new hit registration [12].

The continuous mode uses longer strobe windows ($> 2\,\mu s$) and is intended to provide the readout of pixel hits sampled during periodically repeating strobing intervals of the same length. The continuous mode prioritizes the registration of new hits over finishing the read-out of the entire matrix [12].

The continuous mode was used for the data acquisitions in this thesis.

3.4   Software

Testing and data acquisition was done using the scripts written by members of Bergen pCT collaboration. These scripts use Python and C++ programming languages. The analysis in this thesis uses the ROOT framework, which is a framework for data analysis built by scientists at CERN, mainly for use in CERN projects and is based on the C++ programming language [27].

3.4.1   ROOT - an object-oriented data analysis framework

.root files

The ROOT framework enables saving data in root files. These are compressed binary files that can store any data and any C++ object. The data and objects stored in a root file can be accessed fast and easy through the ROOT framework. An especially useful way of storing data as a ROOT-file is a called a tree which per ROOT's usual naming scheme for objects is called a TTree [27].

TTree

A TTree object is used for columnar data storage and is optimized for reduced disk space usage, high through-put with reduced memory usage [27]. As a columnar data storage object, the TTree has columns which are called branches and each element of the branch is called a leaf. A branch has a data type and an address, which it is given to and these need to be used when storing and reading from it. Each row in a TTree is an entry which has values for the various columns [27].

3.4.2   Tests

To ensure that the setup was working properly, two of the tests among the Bergen pCT production tests were used. The scripts for the tests are available on GitLab in the production_tests repository [28].

Register test

The register test is used to check and evaluate the communication between the computer and the ALPIDE chips. The test is programmed to write to all the registers on the ALPIDE and then read from them to confirm that the writing was successful [29].

   The register test is run from a Python script which results in a classification of the chosen ALPIDE chips as NOK (not okay) or GOLD (ok) based on the number of problematic pixels in each ALPIDE [29].

Analog Scan

The analog Scan tests the analog front-end of the ALPIDE chips. After configuring them to have threshold X, it injects the ALPIDEs with a charge $C1 << x$ in order to look for noisy pixels in the pixel-matrix. A pixel is taken to be noisy, if it reports a hit when C1 is lower than X. To check for dead pixels, a charge $C2 >> X$ is injected to

the pixels and the pixels without a response will be considered dead, by this test. By default the analog scan, tests every 50th row, but it can also test the entire matrix if needed [29].

Analog scan produces a root-file containing a TTree, where it stores the results of the test and it also produces a plot from these results. In a similar way as the register test, ALPIDEs get a classification, but for the analog scan the classes are the following: NOK (the worst), BRONZE, SILVER and GOLD (the best) [29].

3.4.3 Data acquisition

As mentioned earlier, the data acquisition was done using a Python script. This script can also be utilized to perform a fake hit rate test to provide a masking pattern for later data acquisition. The read-out units send triggers to the ALPIDEs in this case [29].

The script needs to receive several parameters to run, these are listed with a short explanation in table 3.3 [29]. The board that was used for this thesis was the VCU118 and 7 ALPIDE chips were used to acquire data for the alignment, because of that the STAVE option was used the most. Although the script accepts any positive integer as the number of triggers and STROBE_DURATION, these values are in DAC unit which represents time in increments of 25 µs. The TRAINS parameter was always set to 1 and TRAINS_DELAY to 0 for this thesis. The total time for data acquisition in seconds is given by eq.3.1.

$$\text{acquisition time} = NUM\_TRIGGERS \times TRIGGER\_DELAY \times 25 \cdot 10^{-6} \text{s} \qquad (3.1)$$

Table 3.3: Explanation of parameters necessary to run data acquisition

Parameter	Explanation	Accepted values
BOARD	Two possible options	PTB or VCU118
CHIPS	One of more chip IDs to be used	0,1,2,3,4,5,6,8,9 or STAVE
NUM_TRIGGERS	Number of triggers to start a frame and acquire data in	$\geq$1 (DAC)
TRIGGER_DELAY	Time between two consequent triggers	$\geq$1 (DAC)
STROBE_DURATION	The time between the two triggers wehre data is actually acquired	>1 and <TRIGGER_DELAY (DAC)
MASKING	Turning masking on or off using a given list of pixels to mask	TRUE or FALSE
TRAINS	Number of trigger packages to be sent with a TRAINS_DELAY between them	>1 (no unit)
TRAINS_DELAY	Time between the end of a train of triggers and the beginning of another train	$\geq$0 (DAC)

The results of data acquisition are stored in a TTree object called alpide_pixel in a root-file which gets its name from the date and the time it was produced. The branches that contain the hit information are the frame_id, chip_id, column and row. Each entry has exactly one frame_id and chip_id, because it was read from one ALPIDE in the period specified by the frame, but column and row are arrays of x and y coordinates of the hits, respectively. A frame in this case is a period of time where the ALPIDE is actively registering hits and storing them in one of the MEBs. The length of a frame is specified by the test parameter, STROBE_DURATION. The TTree alpide_pixel has the following branches:

- ru_id

- frame_id

- stave_id

- chip_id

- abs_time

- spill_id

- bunch_counter

- busy

- column

- row

Of these branches, chip_id, frame_id, column and row were used for the analysis included in this thesis, these will therefore be explained. Each ALPIDE sensor in the mTower and the pCT detector that is being built has an ID with which it can be addressed, this is the chip_id. There were 7 working ALPIDEs used for this thesis and their IDs are from 0 to 6, the chip with ID 7 was not used because of a bug in the ALPIDE which makes it broadcast to all chips when ID 7 is addressed. Each frame is given an ID to be distinguishable from the others and filters or TCuts as they are called in ROOT, can be used to filter data based on a branch or the value of a branch.

The data acquisition script produces an integrated hitmap for all the hits in all the selected chips from the resulting root-file's TTree. A masking pattern as a txt file containing the chip IDs and the pixel coordinates, is needed when MASKING is set to TRUE [29].
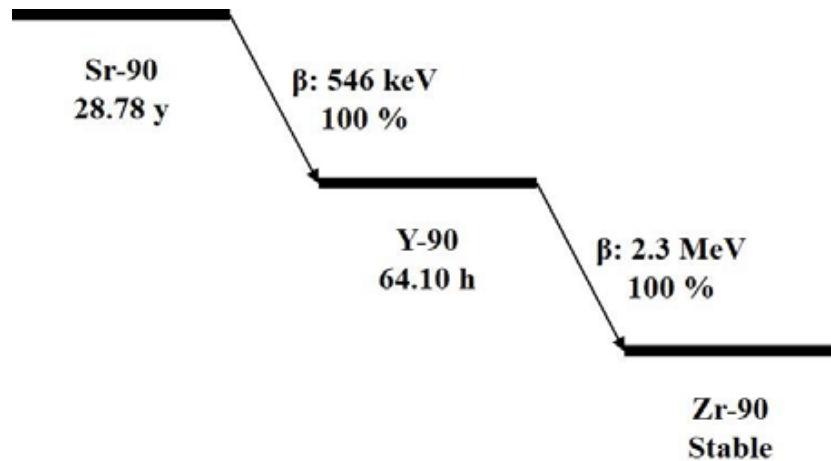
Figure 3.16: The decay scheme of Strontium-90. Figure 8 from [30].

3.5 Radiation sources

3.5.1 Beta source

A Strontium-90 with the half-life 28.8 years was used, which is a β^- emitting source. The activity of the source used was 37 kBq in 1976, the year it was purchased at the University of Bergen, and the tests shown in this document were conducted in the spring of 2023, which is 47 years since 1976. The activity of the source was therefore estimated to be reduced to about 12 kBq. The decay scheme of Strontium-90 is shown in figure 3.16. It consists of two β^- decays, one from Strontium-90 to Yttrium-90, which frees 546 keV (q-value), and one from Yttrium-90 to Zirconium-90 (stable), which frees 2.3 MeV (q-value) [30].

The range of electrons with the kinetic energy of 0.55 MeV is 0.25 g/cm^2 in silicon [31]. This with the density of 2.39 g/cm^3 of silicon [31] gives the range 1.0 mm for these electrons in silicon, which is the main component of ALPIDE chips (see 3.3.2). Stacking all the ALPIDEs in the setup on top of each other would give a thickness of less than 0.2 mm, therefore, the electrons from the Strontium-90 source should be able to traverse all the layers of the setup if they have the right angle. The results of data acquisition when exposing the mTower to this source are shown in chapter 6.

The energy spectrum of electrons from a Strontium-90 source is shown in figure 3.17. The figure shows both electrons from Sr-90 to Y-90 decay, starting from 0 and ending at around 0.55 MeV, and continues with the second decay from Y-90 to Zr-90, which ends at ca. 2.3 MeV. Charged particle's scatterings are energy dependent. The widths of the distributions of scattering angles for electrons at three different energies were calculated and converted to the widths of the residual distributions as listed in table 3.4. The widths are calculated for a thickness of 50 µm, equating the thich ness of 1 layer of ALPIDEs. As it can be seen in the table, the width of the distribution decreases with increasing momentum and energy of the incoming electrons.

In order to detect electrons from the Strontium-90 source, the mTower was positioned vertically (ALPIDE layers were parallell to the surface underneath the mTower) and data acquisition was done with a short TRIGGER_DELAY of 10 µs. The resulting hit maps, tracks and residuals are shown in chapters 5 and 6.
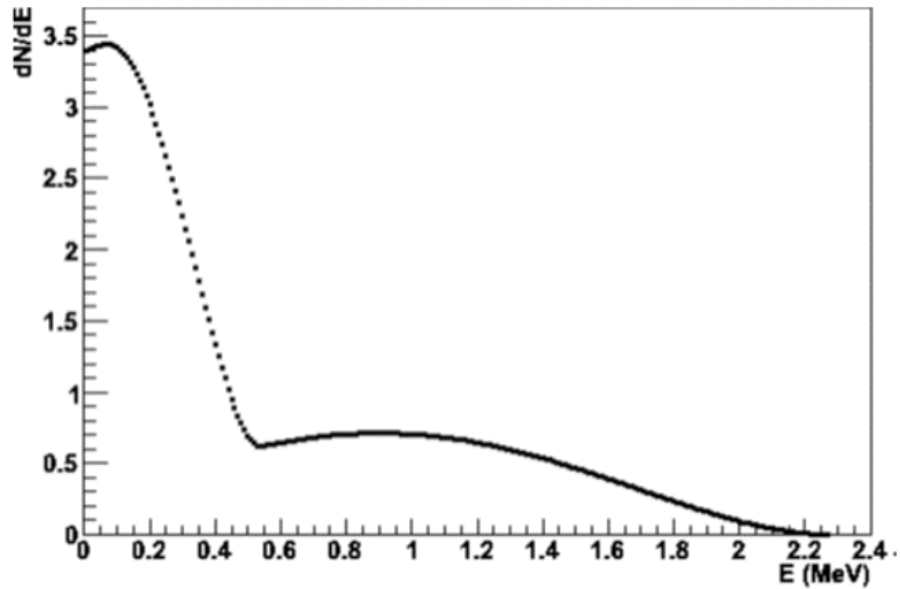
Figure 3.17: Energy spectrum of electrons emitted by a strontium-90 source. Figure 3 from [32].

Table 3.4: Theoretical width of the residual distributions for electrons at different energies. The variances, σ, were calculated from θ_0 values calculated using eq.2.1 multiplied by 5200 μm which is the distance between two layers.

Energy [MeV]	v/c	Momentum [MeV/c]	σ [μm]
0,50	0,86	0,87	1623
1,00	0,94	1,42	885
2,00	0,98	2,46	487

3.5.2 Cosmic muons

The other radiation source used for detection of tracks was cosmic radiation. Every day the planet earth is bombarded by cosmic rays of different kinds. Muons make up the majority of these particles of at sea level [33]. Cosmic muon flux at sea level for muons with momenta more than 1 GeV/c, is around 170 Hz/m^2 or 9 per minute in 9 cm^2, which is the surface area of two ALPIDEs next to each other (see table 3.2) ([33] approximates data given in tables in [34]).

Muons have been used for alignment purposes for many years, because on average, they follow a straight vertical path towards the ground [33]. However they can also get to the ground at other angles. The energy spectrum of muons at sea level for two angles is shown in figure 3.18, where the x-axis shows muon energy in form of muon momentum and the y-axis tells the occurrence of muons with the momentum given on the x-axis. As it can be seen from the figure, the mean momentum of muons that reach sea level at $\theta = 70°$ is higher than that of $\theta = 0°$. This increase is because at larger angles, low energy muons decay before reaching sea level and high energy pions decay before they interact [4].
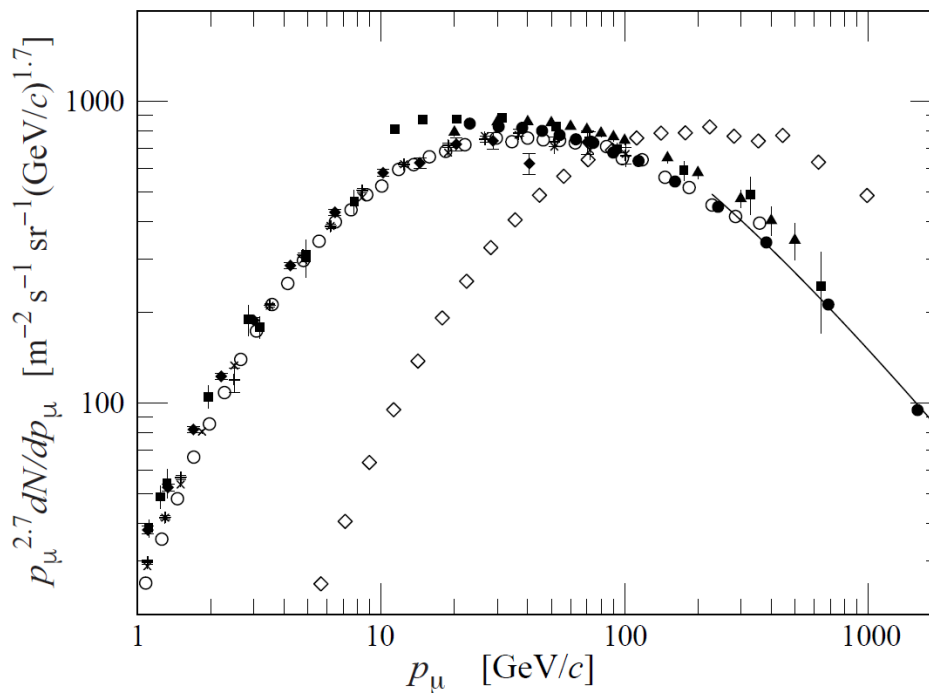
Figure 3.18: Energy spectrum of muons at sea level for $\theta = 70°$ angle (data points shown as hollow squares) and $\theta = 0°$ (all symbols except hollow squares). Figure 30.6 from [4].

The distribution of residuals from a muon source has a Gaussian form and the width of this distribution can be calculated using 2.1 as it was done for the electrons. The widths of the residual distributions for two muon energies is given in table 3.5. It can be seen that the widths of the distributions become much smaller than the ones for electrons, going from 1623 μm to 1.2 μm for 1 layer, and the main reason for this is the much larger energy of the muons. This energy makes the muons scatter much less compared to electrons.

In order to detect muons, the mTower was positioned vertically (as it was the

Table 3.5: Theoretical width of the residual distributions for muons at two energies. The widths (σ) were calculated in the same way as the ones for electrons.

Energy [MeV]	v/c	Momentum [MeV/c]	σ [µm]
900	0,9945	1000	1,2
5895	0,9998	6000	0,19

case for data taking with electrons) and data acquisition was done with a long TRIG-GER_DELAY of 1 ms. The resulting hit maps, tracks and residuals are shown in chapters 5 and 6.

Chapter 4

Data processing and track finding

The final goal of this thesis is to study the alignment of sensors using track trajectories of ionizing radiation, as mentioned earlier. For this purpose, the raw data needed to be processed to remove as much noise as possible, before attempting to find the track trajectories. In the following, the data processing and track finding steps are explained. The source code for the different scripts that do the data processing and track finding are stored in a repository on GitLab [28] and can be made available on request.

4.1 Detection of noisy pixels

After running the register test and the analog scan to make sure that the communications and the ALPIDEs were working properly, the data acquisition was run to find the fake hit rate and detect noisy pixels. Noisy pixels were to be masked in order to reduce the file sizes from the longer data acquisition runs.

The mTower was positioned vertically, similar to how it is positioned in figure 3.7. Data was taken without any source and with 100,000 triggers and 1 ms between each two triggers (TRIGGER_DELAY = 40000). The strobe window was slightly shorter than 1 ms (STROBE_DURATION = 39996) to avoid frame extension, something that can happen if a new STROBE signal is received in the ALPIDE before the reading of the end of the previous frame [12, 23]. A histogram showing the number of hits registered by the pixels of all the ALPIDEs in the mTower is shown in figure 4.1.

Based on figure 4.1, the threshold 10^{-5} of the maximum count for each ALPIDE was chosen to minimize noisy pixels in the data set. All pixels above this threshold were deemed noisy, which for all the ALPIDEs in the mTower (excluding the non-working ALPIDE with chip ID 7) resulted in 1437 noisy pixels. This is about 0.27% of the total number of pixels ($7 \times 1024 \times 512$). The number of noisy pixels found with the thresholds 10^{-4}, 10^{-3} and 10^{-2} were 624, 378 and 222, respectively.

4.1.1 Verification of noise reduction

The largest number of pixels that were deemed noisy (10^{-5} threshold), were masked when taking data without a source (for detection of muons) and with the Strontium-90 source in order to get the cleanest possible data set with the least amount of noise. The masking was done on the hardware level using the built-in masking capabilities of the

Normalized histograms of hit counts per pixel
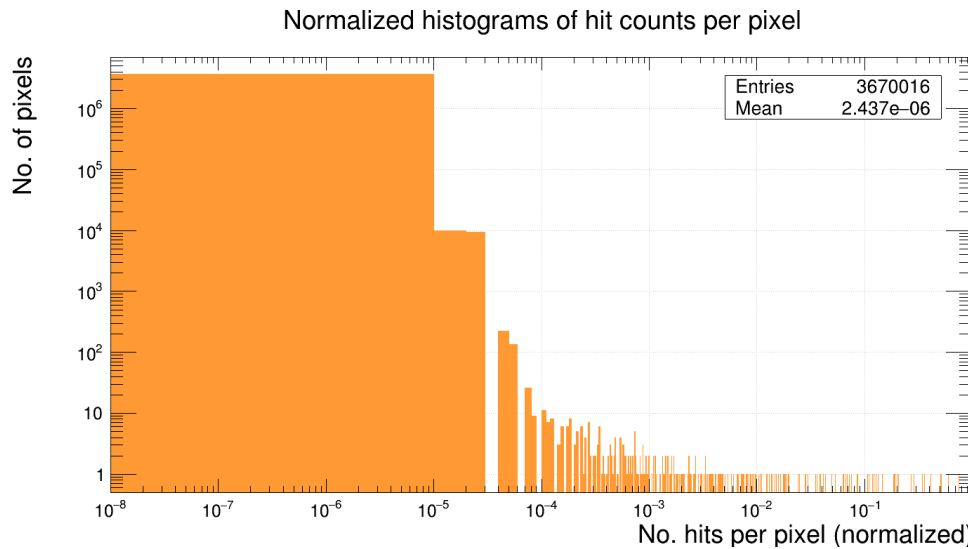
Figure 4.1: X-axis: number of hits per pixel, normalized to the maximum number of hits per pixel in the data set. Y-axis: number of pixels that registered the different number of hits given on the X-axis.

ALPIDE sensors which means that the masked pixels were skipped at read-out. The file size reduced from ≈ 16 megabytes to ≈ 3 megabytes, which is a decrease of about 81%. A plot showing the number of hits per pixel with the same data acquisition parameters as in section 4.1 is shown in figure 4.2. The two data sets are from two different data acquisition runs without any source of radioactivity except for background radiation. As figure 4.2 shows, the number of noisy pixels, that is pixels above the noisy threshold,

Normalized histograms of hit counts per pixel
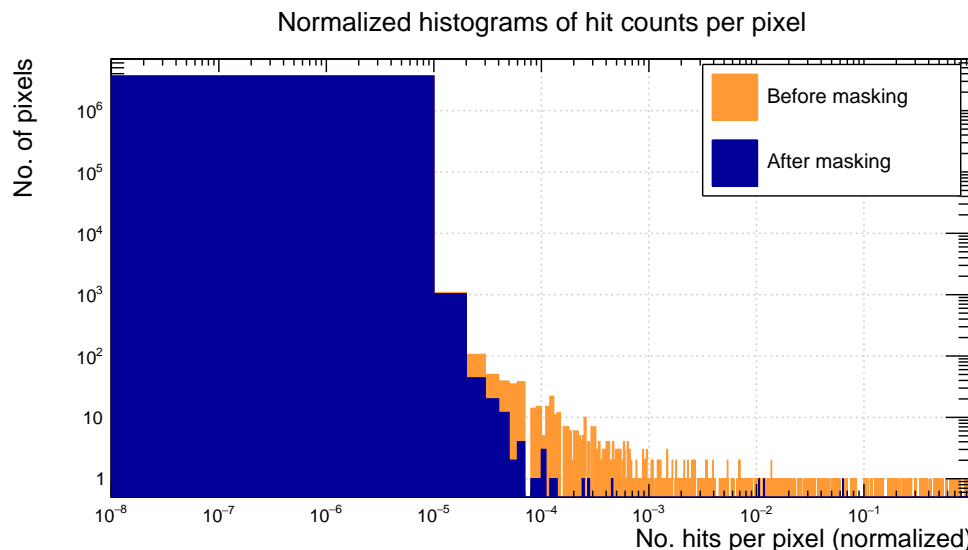
Figure 4.2: the not-masked histogram (orange) is the same as in figure 4.1, a second masked histogram with the same data acquisition parameters except for masking (blue) is superimposed on the first one. The x-axis is normalized to the maximum number of hits in the non-masked data set.

is reduced drastically, but due to statistical probabilities 95 non-masked pixels had more hits than the threshold set. This means that potentially more pixels could have been masked, but a new and longer data taking might be necessary to find these non-masked noisy pixels.

4.2   Track finding

A track is a series of hits registered in three or more layers that make a straight line through space. A straight line in one dimension is given by the following equation:

$$y = a \times x + b \tag{4.1}$$

Where a is the slope and b is the y value when $x = 0$. A line in three dimensions can also be described by eq. 4.1, but instead of scalars, the parameters y, a, x and b have to be vectors. Eq. 4.2 is the general equation for a line in three dimensions, and it can also be written in the form shown in eq. 4.3. Here vector Z is the sum of vector B and the result of the multiplication (dot product) between vectors A and XY.

$$\vec{Z} = \vec{A} \cdot \vec{XY}^{-1} + \vec{B} \tag{4.2}$$

$$\begin{bmatrix} z_1 \\ z_2 \end{bmatrix} = \begin{bmatrix} a_1 \\ a_2 \end{bmatrix} \cdot \begin{bmatrix} x & y \end{bmatrix} + \begin{bmatrix} b_1 \\ b_2 \end{bmatrix} \tag{4.3}$$

In order to align the different layers of the mTower, tracks needed to be found and then with the assumption of a straight path for the majority of the particles that were able to traverse at least three layers of ALPIDEs, residuals of the intermediate layers were found.

4.2.1   Data processing steps

Several steps were taken from having the raw data to calculating residuals. They are shown in a flow diagram in figure 4.3. First, noisy pixels had to be identified (see section 4.1) and then masked (see section 4.1.1). After that, data was acquired while exposing the mTower to β^- radiation from Strontium-90 (see section 3.5.1 and figure 5.1).

In order to find the tracks caused by the β-particles, the populated frames (frames with enough hits to make a track, see section 3.3.7) were found by looping through all the entries of the tree from the data acquisition (see section 3.4.3) and counting the number of layers with hits. The populated frames were then added to a C++ vector, a sequence container that encapsulates dynamic size arrays.

In the next loop, a threshold based on the number of layers with hits was set to decide which entries and frames to process. This was to reduce the running time of the code and avoid processing frames without enough hits to make a track when at least three points in different layers were needed. The processing consisted of storing the hits of these selected frames in C++ vectors, finding clusters from these hits and then storing the cluster centers. All the hits from a processed frame were stored in the vector pixelhits. The cluster centers (see section 3.3.3) that were found from these hits were stored in another vector called allhits. The structures of these vectors are shown in figures 4.4 and 4.5. The sketches show the structure and types of the vectors. The dotted lines indicate increasing index in the direction of the arrow.

The third and last processing loop went through the allhits for the the populated frames. In this loop, the task of finding the track in a single frame was done by a
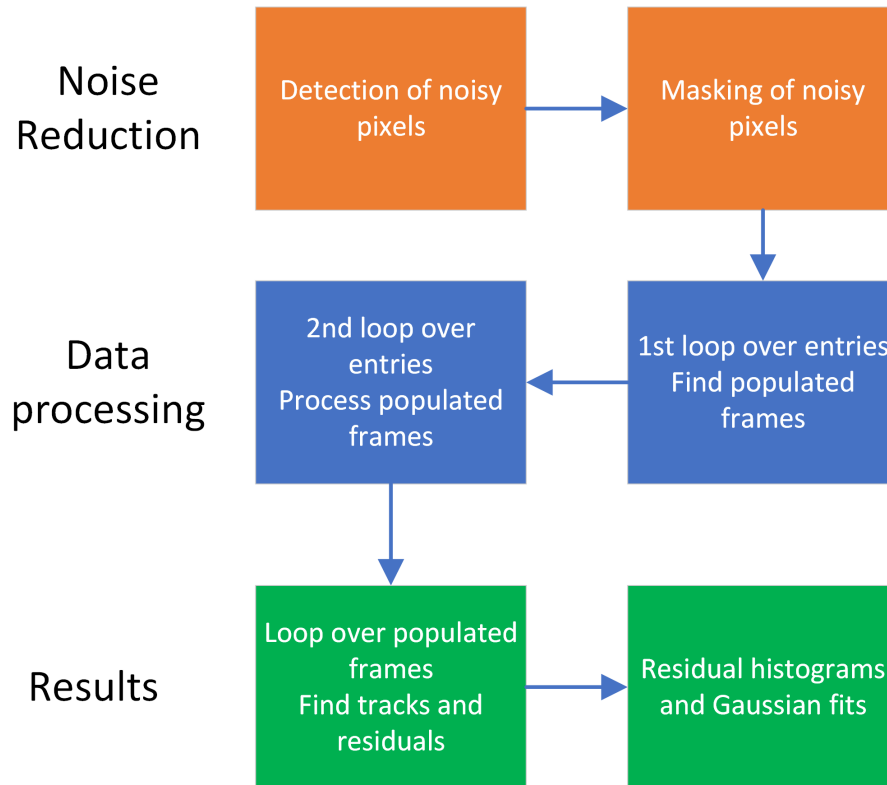
Figure 4.3: Flow diagram showing the data processing steps taken from noise detection to offset histograms.
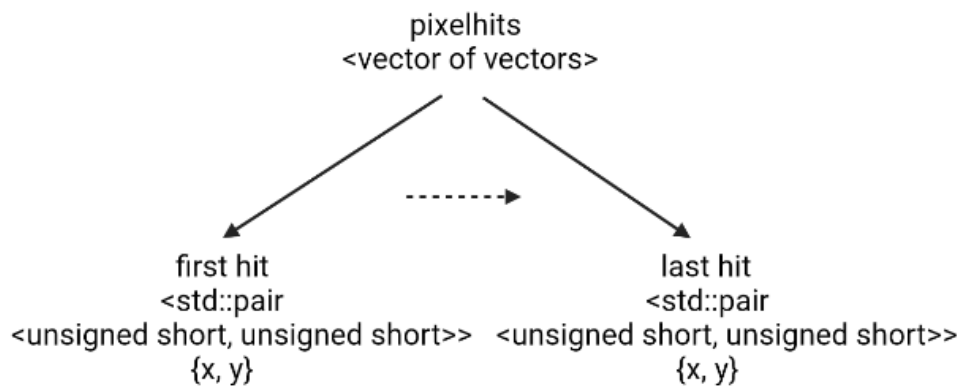
Figure 4.4: The structure and types of the vector containing hits from a processed frame.
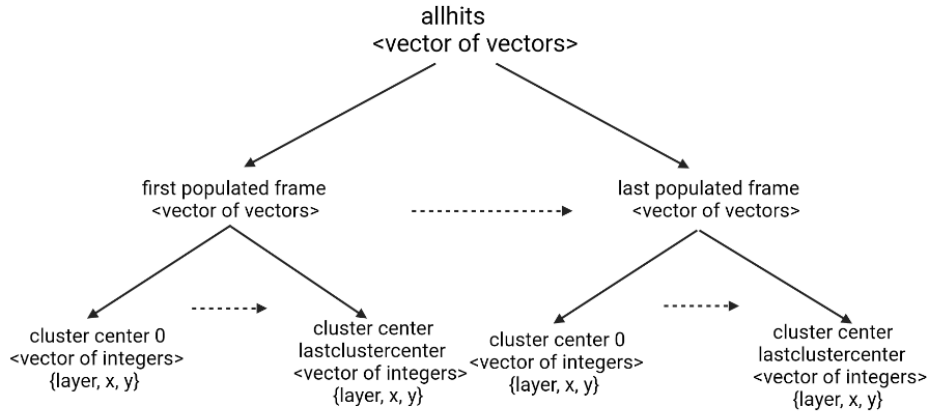
Figure 4.5: The structure and types of the vector containing all cluster centers.

function called track which needs a C++ vector containing the layer, and x and y coordinates for at least three hits. The contents of allhits for a single frame were given to the track function and a vector containing the tracks found was returned. In track finding, only clusters were used. Single pixel hits were omitted because they are unlikely to be caused by either an electron or a muon.

4.2.2 Straight line approach to track finding

This track function sorts the hits in four different vectors, one for each layer, and proceeds to find tracks. In the straight line approach, a straight line is found from two pixels, one in the first layer (layer 0) and the other in the third layer (layer 2). Since the track passes through these pixels in these two layers, the distance from these points to the track is zero, but the distance from the track in layer 1 can be calculated.

To not include random noise as part of the track, the maximum angle with which a particle can hit the layers of the mTower and still traverse all of them, ϕ, is calculated and hits that are beyond it are not included. This was done by finding the maximum and the minimum a_1 and a_2 in eq.4.3 and rejecting tracks that were outside of this range. The calculation of the minimum and maximum value of slope (the calculations are the same for a_1 and a_2) is shown in eq. 4.4 and 4.5, respectively. In the calculation of the slope, d is the number of layers that the track must be able to traverse before it can leave the setup. Two values of d were used; $d = 3$, which makes the maximum allowed angle $\phi_{max} = 160°$ and $d = 40$, which was the highest value used and approximates the number of layers in Bergen pCT's DTC. When $d = 40$, $\phi_{max} = 8.5°$. A sketch is shown in figure 4.7 to visualize this, where the angle ϕ depicts all the allowed track trajectories based on the starting point. This is true for both x and y directions, but the maximum angles can have different values in the two cases.

$$a_{min} = \frac{-x}{d - 0} \tag{4.4}$$

$$a_{max} = \frac{x_{max} - x}{d - 0} \tag{4.5}$$
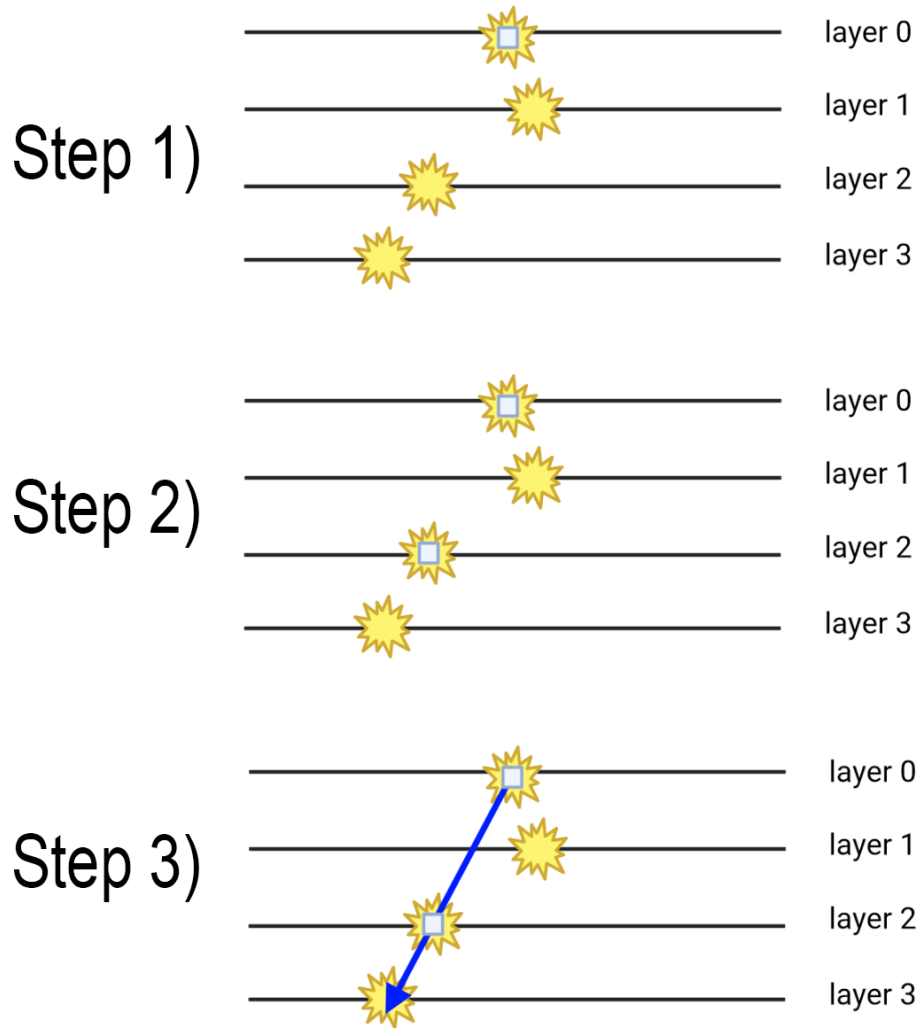
Figure 4.6: A sketch showing the different steps of finding a track in the straight line approach. Step 1) The start of a track is always at layer 0. Step 2) The track calculation needs a point in layer 2. Step 3) The slope is calculated and the intercept is the x and y value of the starting point of the track. The track is now complete.
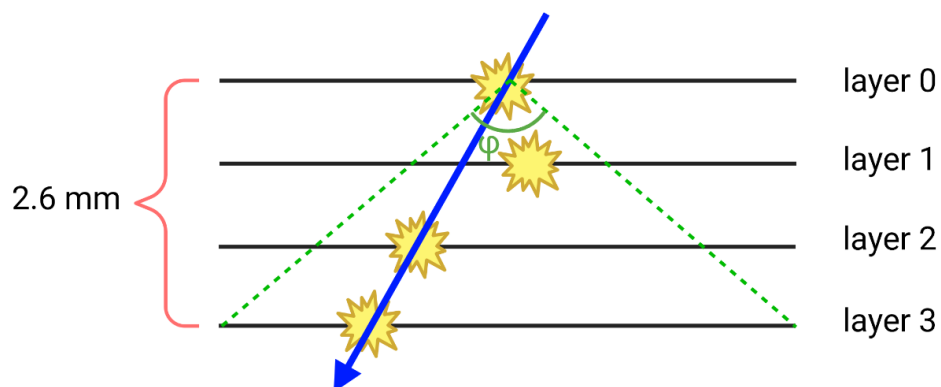
Figure 4.7: Sketch showing how a limit to the angle of tracks with the vertical line perpendicular to the layers of the mTower was set.

A global limit for offset in x and y was also set to not include points that were too far from a track as part of it when calculating residuals. This is shown for the x direction in the sketch in figure 4.8, but the same applies for the y direction. As it is possible to see a misalignment of ≈ 1 mm without using any instruments, this was the limit used for the distance from the track.
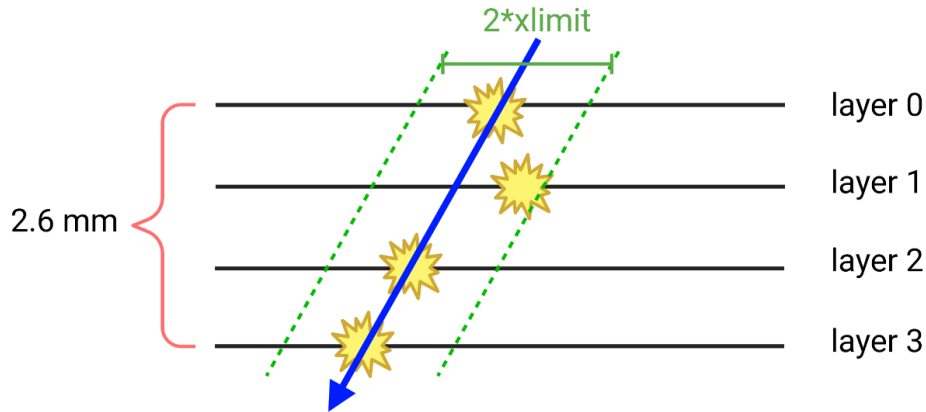
Figure 4.8: Sketch showing which hits are included based on distance from the track.

The distance of the point in layer 1 from the track was calculated for all points in that layer. This was done separately for x and y direction. For each point, the distances to the track in x and y were combined using eq.4.6, which calculates the root mean square.

$$RMS = \sqrt{\frac{(dx)^2 + (dy)^2}{2}} \tag{4.6}$$

In case more than one point met the criteria to be part of the track, only the closest one to the track (the smallest RMS) was used in calculating the distance to the track.

All the possible tracks in a frame are stored and returned by the track function that performs the track finding and the calculation of the residual, as long as they meet the angle and distance limits. An example of a track found by this approach is shown in figure 4.9.
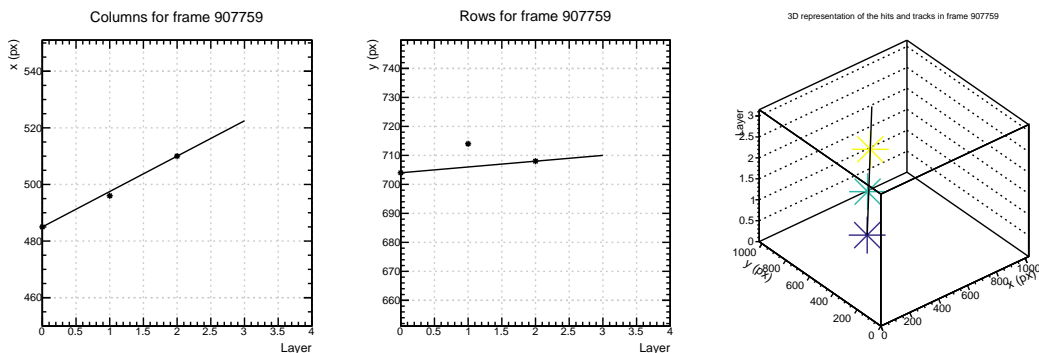
Figure 4.9: Example of a single track found by the straight line track finding approach.

4.2.3 Fit approach to track finding

In another approach to track finding, fitting was done using ROOT's built-in fit functionality for a graph with points. The fit finds the line that gives the smallest total distance from the points. For every three points in layers 0, 1 and 2, a linear fit was done, the distances dx and dy to the track were calculated for all possible layers (three if there were three points and four if layer 3 also had a hit). Then these residuals were compared with the specified xlimit and ylimit values (both were set to 1 mm, see figure 4.8 and section 4.2.2). If the dx in any layer was larger than the xlimit value, the track would be rejected. The same limitation was done for dy and ylimit. The sketch in figure 4.10 visualizes this approach to track finding. The same applies to the y direction.
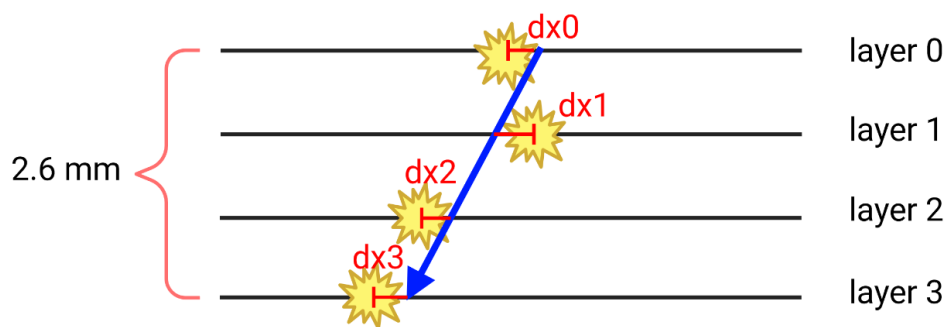
Figure 4.10: Sketch of the second approach to track finding. The layers of the mTower, a series of hits in different layer and a fitted track are shown, together with the offsets calculated for each layer.

The slope (angle) limitation done from the straight line approach (see figure 4.7), was also implemented in the second approach. An example of a track found by this approach is shown in figure 4.11. As it can be seen from the figure, the fit tries to minimize the residuals for all the three layers.
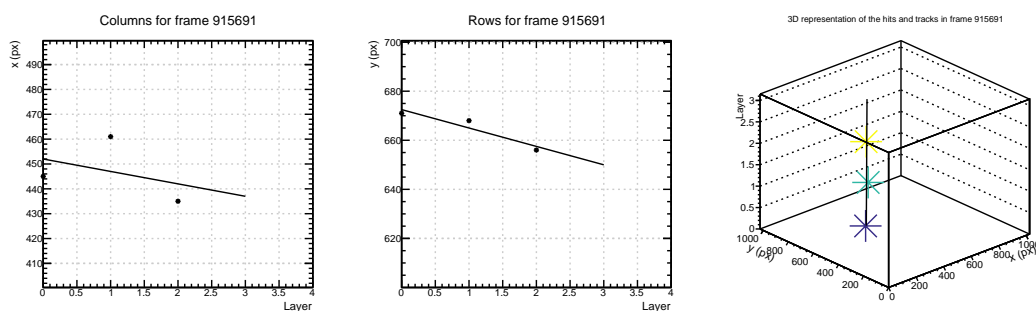
Figure 4.11: Example of a single track found by the fit track finding approach.

4.3   Offset calculation

For each track finding approach, the residuals found are first added to a one dimensional histogram for x and y separately for each layer. Then the histogram is fitted by a Gaussian weighted fit. The weighting means that the fit gives more importance to values with less uncertainty than ones with higher uncertainty. The mean of the fit represents the offset, which is the misalignment of the layer relative to the coordinate system made by the tracks and would be 0 in a perfectly aligned detector, and the variance (σ) of the fit represents the uncertainty of the mean. This uncertainty is a caused by a combination of the resolution error and the particle scatterings inside the mTower. A sketch of a residual distribution showing the mean (μ), variance (σ) and the offset is shown in figure 4.12.
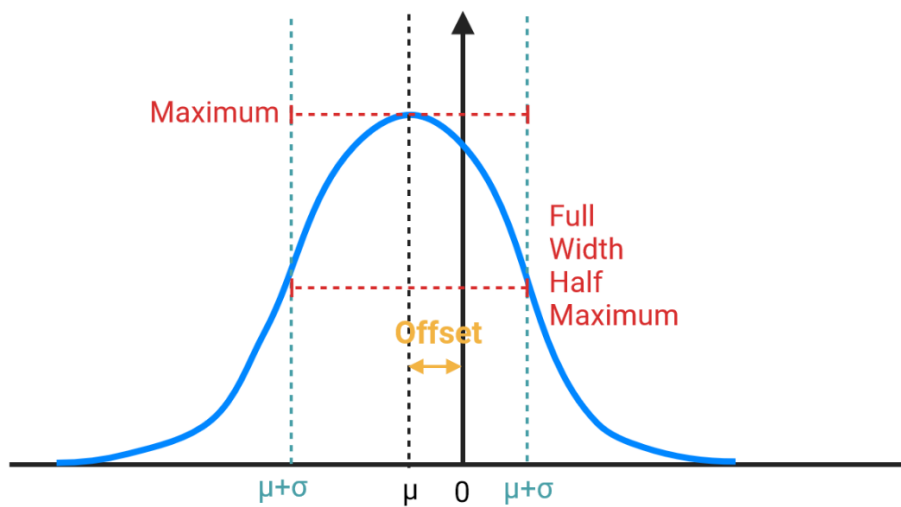
Figure 4.12: A sketch of a residual distribution used to find the offset.

The fits are superimposed on the histograms in chapter 6 and the values for the mean and the variance are given in tables in the same chapter.

Chapter 5

Data analysis

Plots that show different aspects of the data from data acquisition with the β emitting source and without it are shown and briefly explained in this chapter. Hit maps show the accumulated hits that were registered for each layer. These hits sometimes generated clusters of hits next to each other in a single frame, the different cluster sizes are also shown in this chapter. Hit maps and cluster size plots are produced using ROOT.

5.1   Hit maps

5.1.1   Hit maps from Strontium-90

Data taking with the Strontium-90 source at around 1 mm from the first layer (layer 0) resulted in the following hit maps shown in figure 5.1.   As it can be seen in the aforementioned figure, the particle hits become more and more sparse and spread with increasing number of layers in the particles' path. The parameters were 10×10^5 triggers, with $10\,\mu$s between each two triggers (TRIGGER_DELAY), the STROBE_DURATION was also $\approx 10\,\mu$s. This resulted in the acquisition time of 1 s. As it can be seen from the hit maps, the source was positioned close to the center of layer 0, most of the hits are therefore close to the middle of the axis on both columns and rows axes. The hit map in layer 3 only has hits on the bottom part, because the other half is where the ALPIDE with chip ID 7 is located. This ALPIDE was not used, so in the plots of hit counts and cluster counts, the numbers for layer 3 are doubled to represent the entire layer.

With larger distances from the source, the hits registered become more dispersed through the layers, as it can be seen in figure 5.2. To produce this plot, the source was positioned at distances of approximately, 1 mm, 1 cm and 5 cm and data acquisition was done for 1 s.

Data acquisition was carried out three more times for the Strontium-90 source where the position of the source was changed between acquisitions in order to study the effect of source position in number of tracks found and the data offsets that were calculated based on that. For acquiring data with this source for 10 minutes, the parameters were 6×10^7 triggers, with $10\,\mu$s between each two triggers (TRIGGER_DELAY), the STROBE_DURATION was also $\approx 10\,\mu$s. The hit maps for data where the source was ≈ 1 mm above layer 0, are shown in the following figures. In figure 5.3 the source is
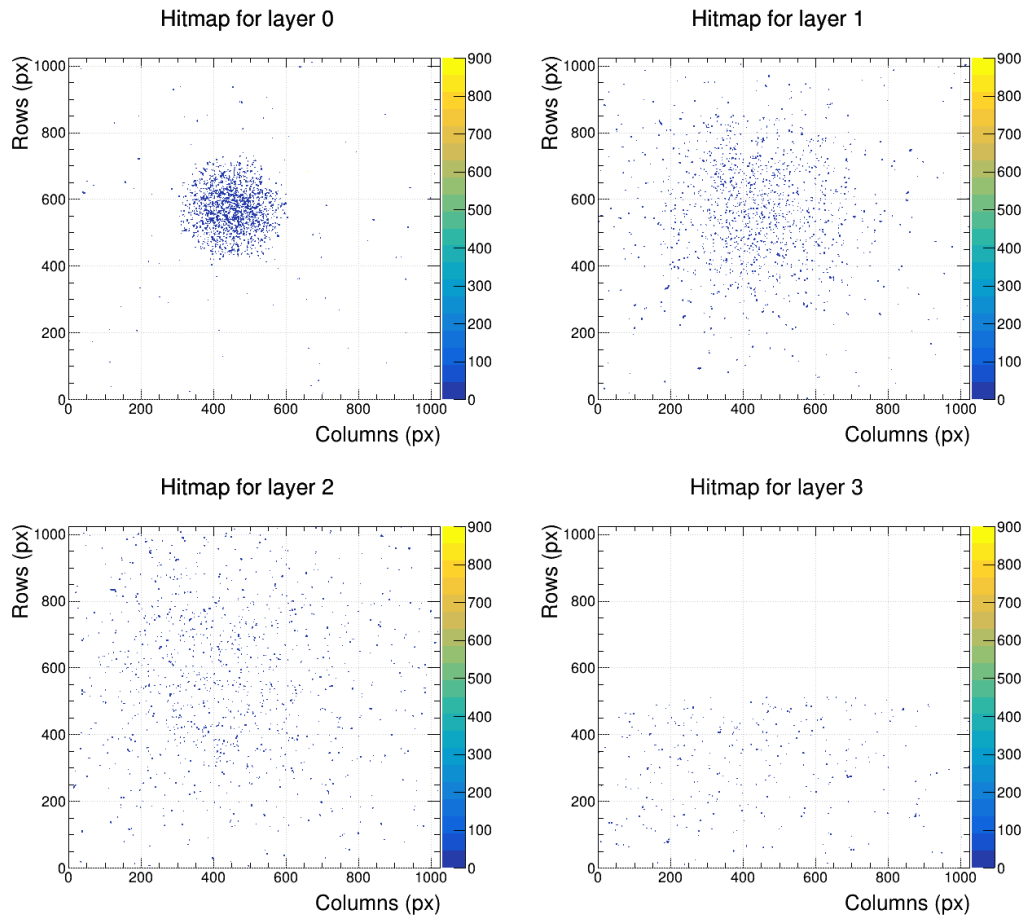
Figure 5.1: Hit maps for the different layers of the mTower. Layer 3 consists of chip IDs 6 and 7, and because chip ID 7 was not used, the plot only shows hits on one half of the layer. The source was ca. 1 mm away from layer 0.
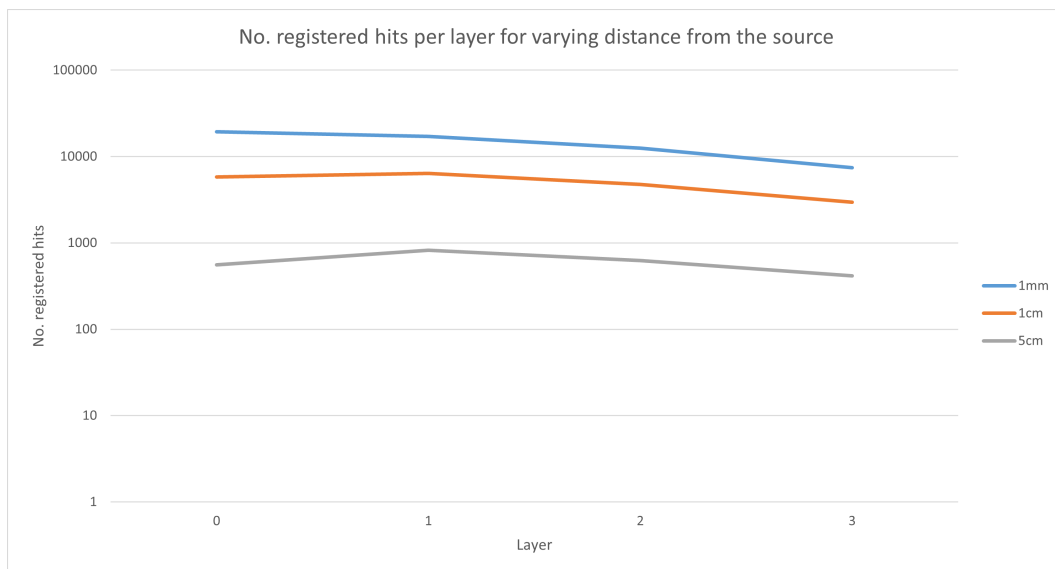
Figure 5.2: Number of hits per layer with varying distance from the source. Each line represents a distance from the source shown in the legend on the right. Logarithmic scale on the y-axis is used and the values for layer 3 are multiplied by 2.

above the center of layer 0, and in figure 5.5, the source is positioned approximately over the center of chip ID 0. Two data acquisitions were done where the source was positioned above the center of one ALPIDE (chip ID 0 and chip ID 1) in each run. This was done to study the tracks and offsets on one side of the mTower at a time.
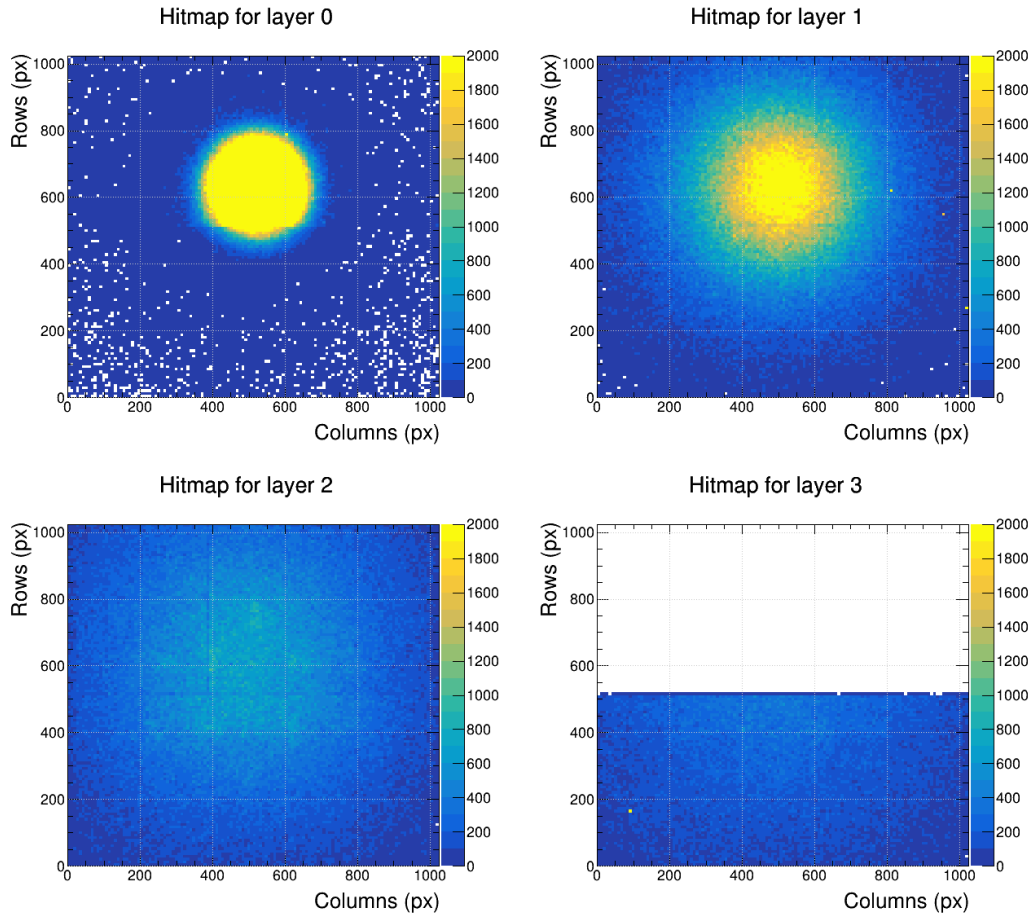
Figure 5.3: Hit maps for the different layers of the mTower. Layer 3 consists of chip IDs 6 and 7, and because 7 doesn't work, it only shows half the layer. The source was ca. 1 mm away from the center of layer 0. Data acquisition lasted 10 minutes.

The number of clusters found in the different layers of the mTower from the Strontium-90 source is shown in figure 5.4. The clusters in frames without enough cluster centers to make a track were not included.

5.1.2 Hit maps from cosmic muons

Accumulated hits from 65 hours of data acquisition without a radioactive source is shown in the hit maps of figure 5.6. The parameters for the data acquisition were 2.34×10^8 triggers, with 1 ms between each two triggers, the STROBE_DURATION was also ≈ 1 ms. Since muons scatter much less compared to electrons, the hit maps of the different layers look very similar, however the number of hits per layer differs as shown in figure 5.7. Number of clusters per layer is also shown in figure 5.8. Comparison of figure 5.7 with figure 5.8 shows that most of the difference comes from single hit pixels that are most likely caused by noise rather than particle hits. The clusters from frames
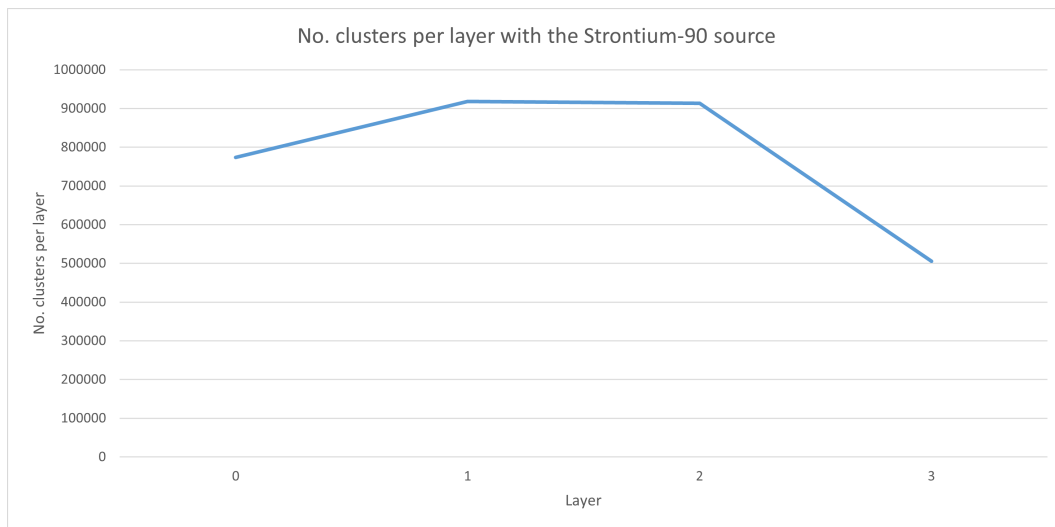
Figure 5.4: Number of clusters per layer for the same data as shown in 5.3, but the clusters from the frames without clusters in all the first three layers are omitted. The value for layer 3 is multiplied by 2.
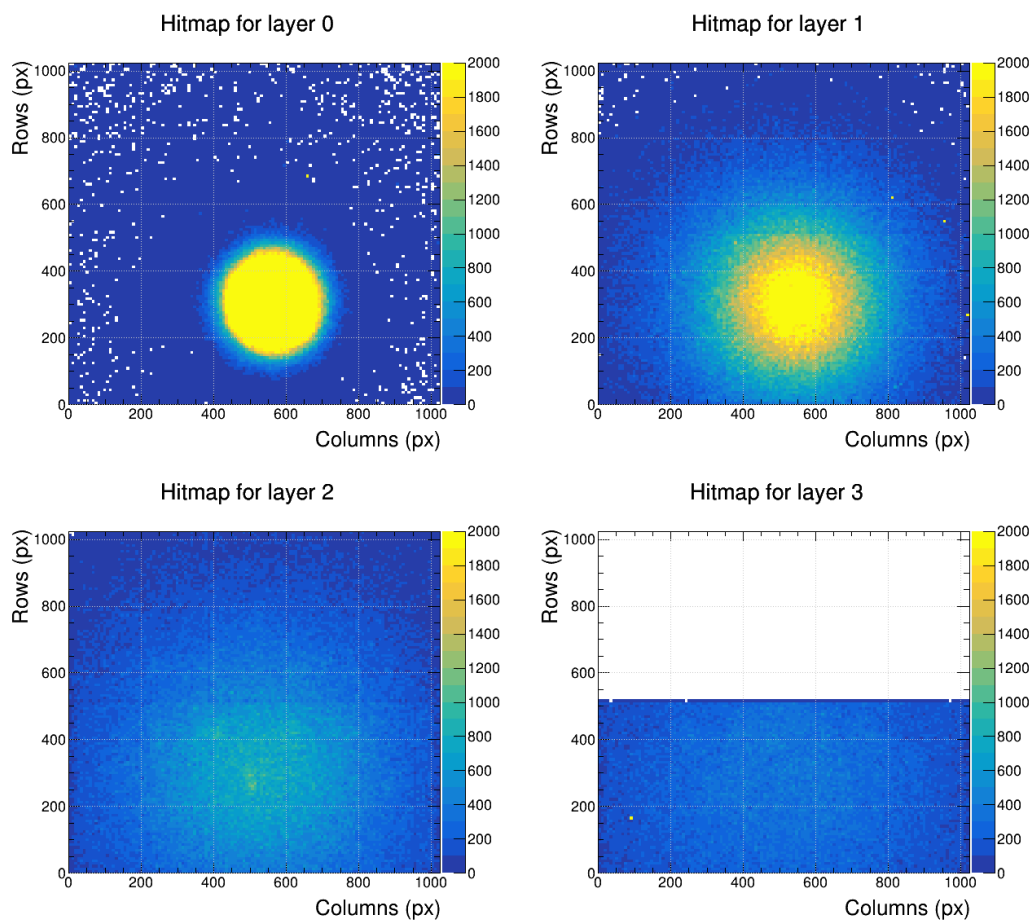
Figure 5.5: Hit maps for the different layers of the mTower. The source was ca. 1 mm away from the center of chip ID 0 in layer 0. Data acquisition lasted for 10 minutes.

without clusters in all the first three layers were not included. The plot in figure 5.8 closely resembles figure 5.4.
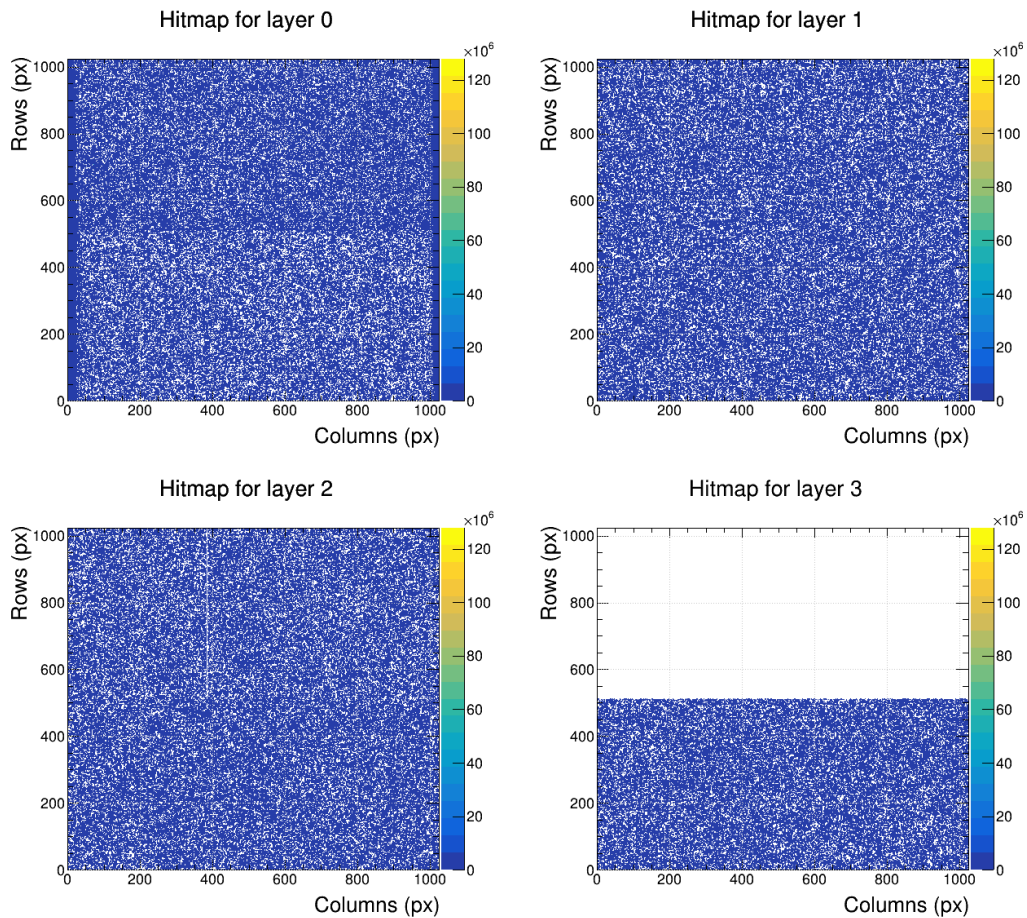
Figure 5.6: Hit maps showing the different layers of the mTower. Layer 3 only has one working ALPIDE.

5.2 Cluster size

The cluster sizes for the different ALPIDEs for data taken with the Strontium-90 β source is shown in figure 5.9 where the average cluster size is ≈ 4.9 pixels. There are more smaller clusters than bigger ones, as it can be seen in the figure, but there is no general trend in the cluster sizes. The ALPIDE chip that stands out in figure 5.9 is the one with ID 0, who has much fewer clusters that are larger than 40 pixels, compared to all the other ALPIDEs. The values given in the statistics box of the histograms are given in table 5.1 for better readability.

The cluster sizes in the mTower's ALPIDEs from cosmic muon detection are shown in the histogrms of figure 5.10. The histograms shown in figure 5.10 generally show a decreasing number of clusters for increasing cluster size, similar to the ones for the electrons from Strontium-90, but there is also a small peak around cluster size 35 for ALPIDEs with IDs 0 and 1. For ALPIDEs with IDs 2 and 3, the number of clusters seems to flatten after cluster size 40. The reason for these deviations from the general trend was not studied closely, but they are likely caused by the angle of the muon

Figure 5.7: Number of clusters per layer of the mTower registered by the ALPIDEs from cosmic muon detection. For layer 3, the number of hits is multiplied by 2.
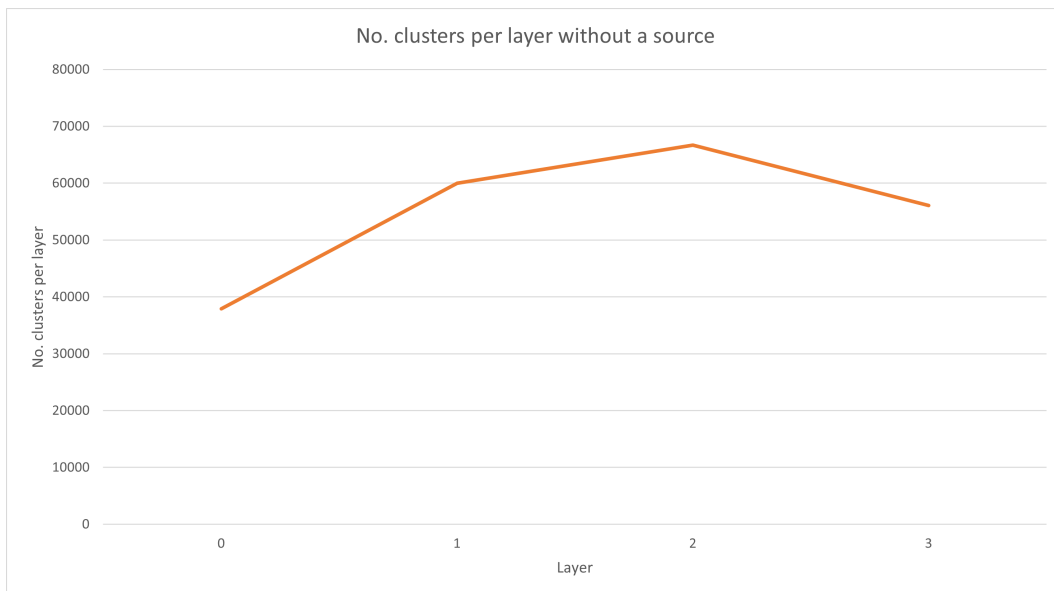
Figure 5.8: Number of clusters per layer of the mTower registered by the ALPIDEs from cosmic muons detection. The clusters from frames without clusters in all the first three layers were not included. For layer 3, the number of hits is multiplied by 2.

Table 5.1: The number of clusters, the mean cluster size and the standard deviation of the mean for each ALPIDE chip from electrons, as shown in figure 5.9. The means of these values are given in the last row.

Chip ID	Number of clusters	Mean cluster size [pixels]	Standard Deviation [pixels]
0	7.3×10^4	3.9	2.7
1	1.3×10^6	4.6	3.6
2	3.4×10^5	5.7	4.3
3	9.4×10^5	5.0	3.8
4	3.5×10^5	5.4	4.0
5	5.9×10^5	4.6	3.5
6	2.6×10^5	5.1	3.9
Mean	$\mathbf{5.5 \times 10^5}$	**4.9**	**3.7**
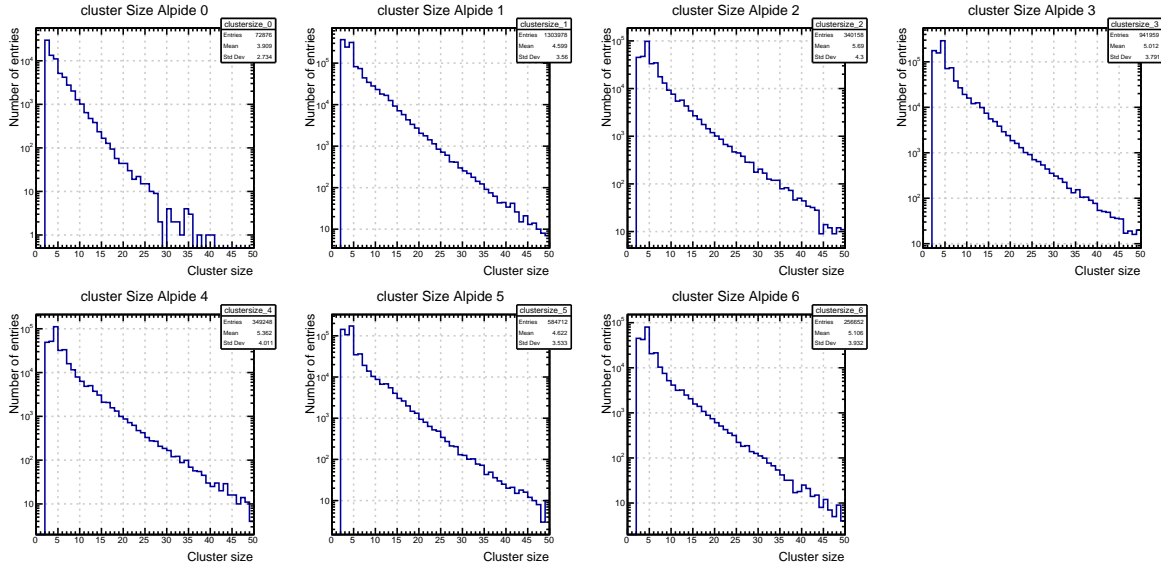
Figure 5.9: Cluster sizes for ALPIDE sensors in the mTower for data taken with the Strontium-90 β source. The duration of data acquisition was 10 minutes.

trajectories that are nearly parallel to the ALPIDEs xy plane and therefore leave a long trail in the ALPIDEs, where many pixels register hits.
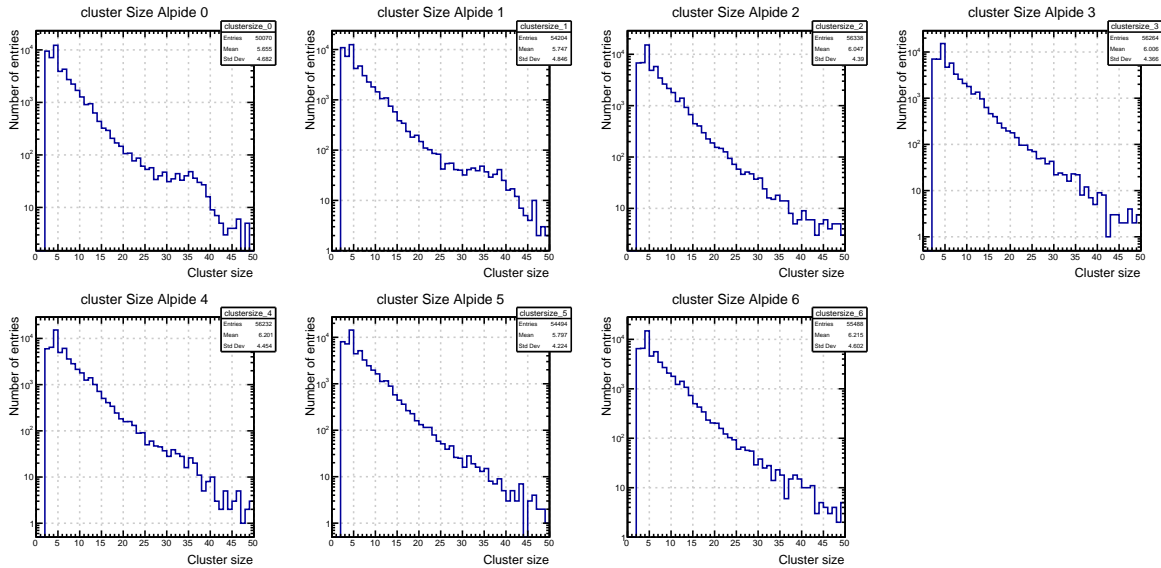
Figure 5.10: Cluster sizes for ALPIDE sensors in the mTower from data taken with cosmic muons. The duration of the data acquisition was 65 hours.

The number of clusters, the mean cluster size and the standard deviations given in figure 5.10 are given in table 5.2 for better readability. The average number of clusters, means and standard deviations is also calculated and given in the table.

The number of clusters in the data set from data acquisition with the β source generally decreases, except for the chips with IDs 0 and 1 which are in the same layer. There is a significant different between these ALPIDEs number of clusters, because the source position was not exactly over the center of the layer and covered more of chip ID 1 than ID 0. For the data from muon detection, the number of clusters does not

Table 5.2: The number of clusters, the mean cluster size and the standard deviation of the mean for each ALPIDE chip from cosmic muons, as shown in figure 5.10. The means of these values are given in the last row.

Chip ID	Number of clusters	Mean cluster size [pixels]	Standard Deviation [pixels]
0	5.0×10^4	5.7	4.7
1	5.4×10^4	5.7	4.8
2	5.6×10^4	6.0	4.4
3	5.6×10^4	6.0	4.4
4	5.6×10^4	6.2	4.5
5	5.5×10^4	5.8	4.2
6	5.6×10^4	6.2	4.6
Mean	$\mathbf{5.5 \times 10^4}$	**6.0**	**4.5**

change significantly from one ALPIDE to the next.

The mean cluster size is not the same for the different ALPIDEs from the same data set and there does not seem to be a general trend as it both increases and decreases from one ALPIDE in one layer to the next one in another layer. The only noteworthy thing is between the two data sets, which is that the mean cluster size for muons is larger than that of electrons from the Strontium-90 source, which is expected from the much higher energies of muons. The mean cluster size for the cosmic muon data is ≈ 6.0 pixels compared to ≈ 4.9 for the electrons.

Chapter 6

Results and discussion

In this chapter, the tracks found in the data from data acquisition with the β emitting source and from cosmic muons are shown and the residuals from these tracks, meaning distances between the tracks found and the points in the different layers to these tracks are studied. The tracks are found from two different approaches and the results from each track finding approach is presented separately. The angle limitation for the slopes is specified by ϕ_{max}. A track starting in layer 0, has to have a slope that is inside of the range specified by ϕ_{max} as it is shown in figure 4.7.

6.1 Tracks

6.1.1 Tracks from the straight line approach

With an offset limit of 1 mm for both x and y directions, the straight line track finding algorithm was used to find tracks in the data with the β source and the data from cosmic muon detection. The angle limit was varied and is specified for each plot. The number of tracks found from each source and some of the parameters that influence the number of tracks are given in table 6.1. The source column specifies the radiation source, side specifies if both sides of the layers in the mTower were used in track finding or only one (left: ALPIDE's with ID's 0,2,4 and 6, right: ALPIDE's with ID's 1,3 and 5), ϕ_{max} is the maximum angle allowed by the angle limitation explained in section 4.2.2 and "No. tracks" is the number of tracks that the straight line approach to track finding was able to find.

Table 6.1: Number of tracks found by the straight line track finder for different data sets and two angle limits.

Source	Side	ϕ_{max}	No. tracks
Beta	Left	8.5°	1530
Beta	Right	8.5°	4259
Beta	Both	160°	304678
Beta	Both	8.5°	4282
Muon	Both	160°	17761
Muon	Both	8.5°	320

Tracks from Strontium-90

The straight line track finding algorithm with the largest possible angle limit ($\phi_{max} = 160°$), was able to find 304678 tracks in the data acquired with the Strontium-90 source during 10 minutes. The first 100 number of these tracks are shown in figure 6.1.
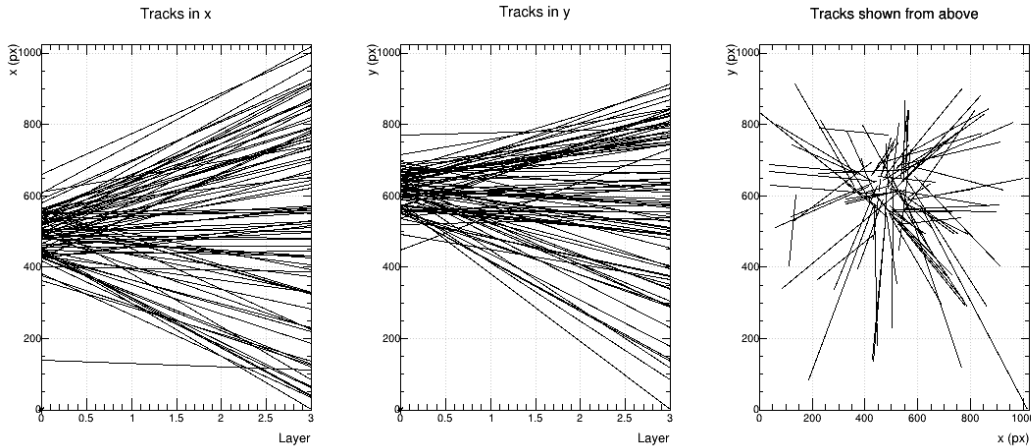
Figure 6.1: Plot of 100 tracks found in the same data set as shown in the hit maps in figure 5.3 where the source was above the center of layer 0 and the angle limitation was $\phi_{max} = 160°$.

Number of tracks found with $\phi_{max} = 8.5°$ was 4282, and the first 100 of these tracks are shown in figure 6.2. As the figure shows, these tracks are located in a much smaller part of the x and y plots, due to the limitation of the angle ϕ_{max}.
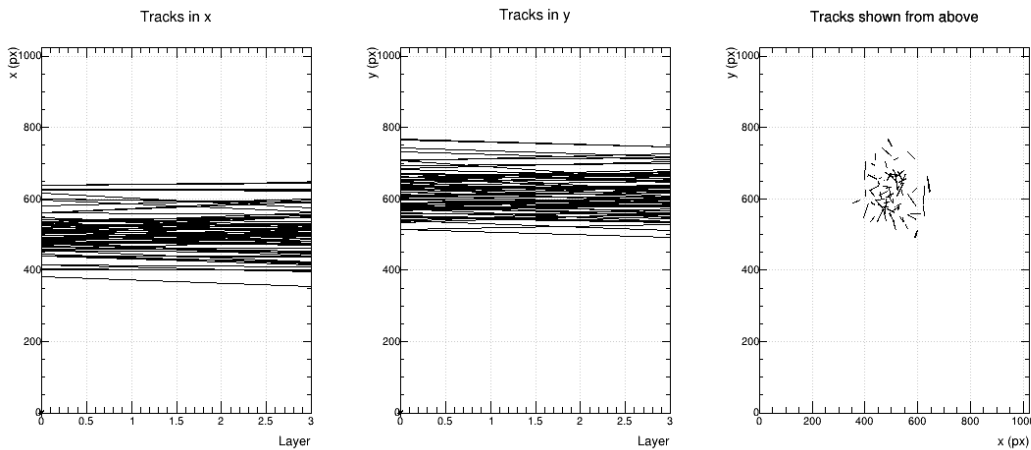
Figure 6.2: Plot of the first 100 tracks found with $\phi_{max} = 8.5°$ in the same data set as shown in the hit maps in figure 5.3 where the source was above the center of layer 0.

Keeping all parameters the same for data acquisition, the source was moved above the center of chip ID 0, and data was taken for 10 minutes. This was repeated after moving the source above the center of chip ID 1. The position given here was only visually estimated.

Tracks from cosmic muons

The straight line track finding algorithm with the angle limitation $\phi_{max} = 160°$ found 17761 tracks from cosmic muon detection. 100 of these tracks are shown in figure 6.3.
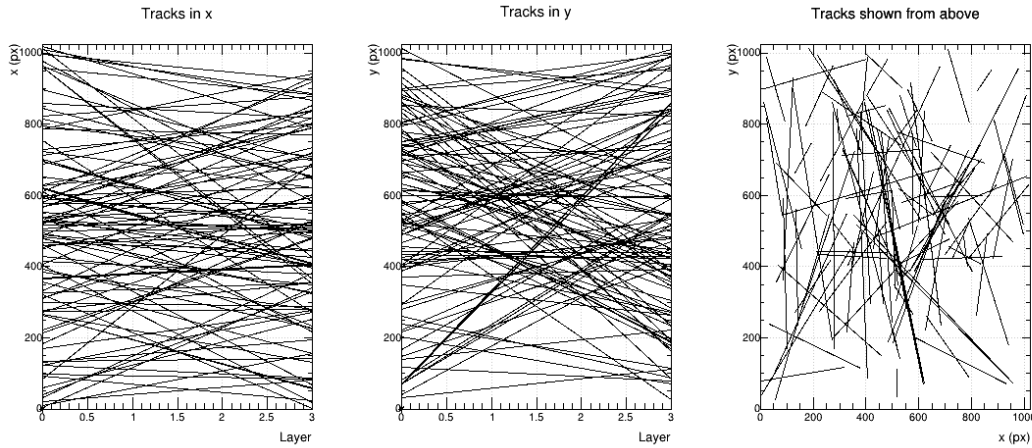
Figure 6.3: Plot of 100 tracks found with the angle limitation $\phi_{max} = 160°$, in the same data set as shown in the hit maps in figure 5.6, from detection of cosmic muons.

The number of tracks found from cosmic muon detection with $\phi_{max} = 8.5°$, was 320 and the first 100 of these are shown in figure 6.4

The plots in figures 6.3 and 6.4 show how the muon tracks come from many different angles and how the angle limitation removes the ones that are outside of the range when $\phi_{max} = 8.5°$.

6.1.2   Tracks from the fit track finding approach

The tracks from the fit approach were visually very similar to the ones from the straight line approach. Therefore, only the number of tracks found from this approach will be shown in this section. The number of tracks found by the fit approach with different sources, in different sides of the layers and with two different slope limitations given by the angle ϕ_{max} is given in table 6.2. The columns of table 6.2 have the same definitions as for table 6.1.
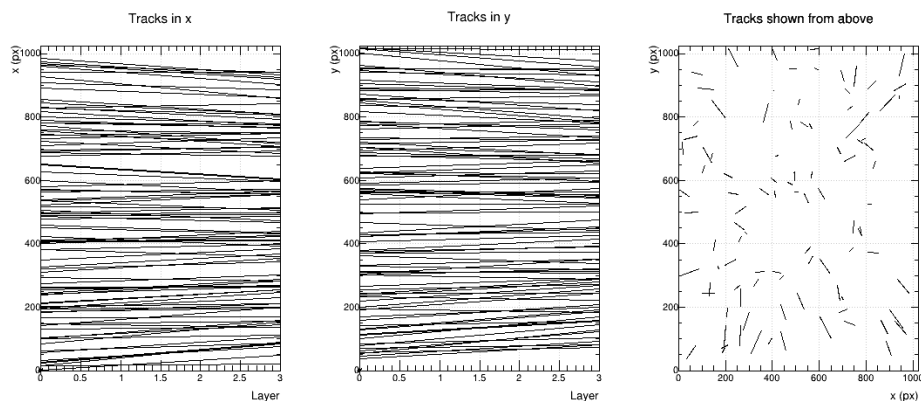
Figure 6.4: The first 100 tracks found by the straight line track finding algorithm from cosmic muons with $\phi_{max} = 8.5°$.

Table 6.2: Number of tracks found by the straight line track finder for different data sets and two angle limits.

Source	Side	ϕ_{max}	No. tracks
Beta	Left	8.5°	5312
Beta	Right	8.5°	5871
Beta	Both	160°	452033
Beta	Both	8.5°	5838
Muon	Both	160°	23145
Muon	Both	8.5°	390

6.2 Residuals calculated from tracks

Based on the tracks shown in section 6.1, the residuals in the different layers were calculated and plotted as the histograms shown in the following. The results are shown for the straight line and fit approaches to track finding.

The distributions of residuals from the data with the Strontium-90 source are much wider than the ones from muons, because of that the x-axis shows a wider range of values in order to show a bigger part of the distributions.

6.2.1 Residuals from Strontium-90

Straight line track finding approach

The residuals calculated based on data taken with the Strontium-90 source which was positioned at ca. 1 mm distance from the center of layer 0 (visual estimation) are shown in figure 6.5. A fit was performed on each of the one-dimensional residual histograms to find the most likely offset value in x and in y dimensions separately. The fits are superimposed on the histograms. The angle limitation was $\phi_{max} = 160°$. To produce this plots, several bin sizes were tested, and the final choice was a bin size which is equal to the pixel size in each direction (see section 3.3.4 in chapter 3), and the peak which is going beyond the red curve of the fit is an artefact of this choice. The other bin sizes that were tested produced other artefacts.
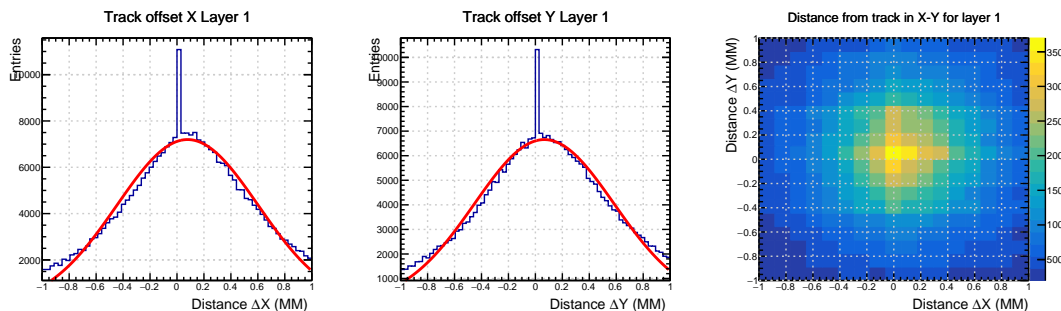
Figure 6.5: Residuals from layer 1 in x and y direction based on data taken with the Strontium-90 source which was positioned at ca. 1 mm distance from the center of layer 0. The angle limitation was $\phi_{max} = 160°$

The residuals from the tracks with the angle limitation, $\phi_{max} = 8.5°$, are shown in the histograms in figure 6.6. Some of the tracks that were used to make these histrograms are shown in figure 6.2.
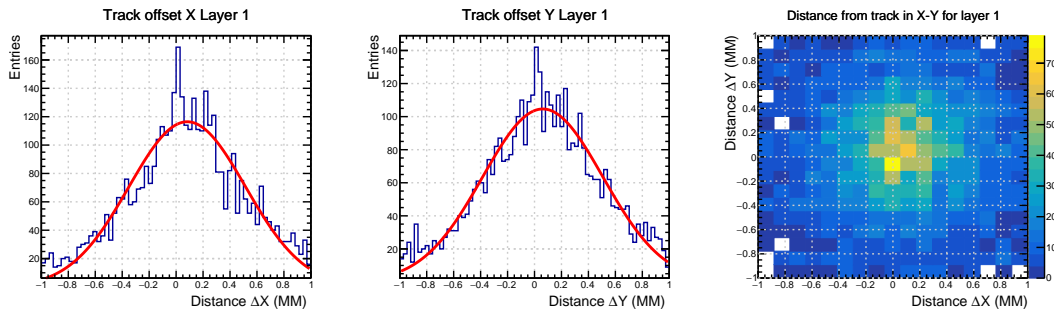
Figure 6.6: Residuals from layer 1 in x and y direction based on the tracks in the data taken with the Strontium-90 source which was positioned at ca. 1 mm distance from the center of layer 0. The angle limitation was $\phi_{max} = 8.5°$

The mean and variance of the fit over each histogram shown in figures 6.5 and 6.6 are shown in table 6.3 with their uncertainties. The straight line approach was used to find the tracks and because of that, only residuals from the tracks in layer 1 were calculated. The same data set was used but the angle limitation was changed between the two runs.

Table 6.3: The results of the fits over the histograms of residuals in layer 1 from the data with the β emitting source centered above layer 0.

Layer	No. tracks	Source	ϕ_{max}	Mean_x [µm]	Variance_x [µm]	mean_y [µm]	Variance_y [µm]
1	304678	beta	160°	80 ± 10	520 ± 10	70 ± 10	520 ± 10
1	4282	beta	8.5°	80 ± 10	430 ± 20	60 ± 10	450 ± 10

The residuals were also calculated for the data where the source was positioned above one side of layer 0 (centered approximately above the center of one ALPIDE at a time). The residuals are shown in figures 6.7 and 6.8 for the data where the source was positioned above the half of layer 0 with chip ID 0 and chip ID 1, respectively. For these data sets only the angle limitation $\phi_{max} = 8.5°$ was used, since it was shown from table 6.3 that the variance of the fit becomes smaller this way and the width of the distribution decreases. This increases the confidence in the calculated mean value from the fit.

The mean and variance of the fit over the histograms shown in figures 6.7 and 6.8 are shown in table 6.4. Although, the tracks found in the data set from when the Strontium-90 source was positioned above the side of the layer 0 with chip ID 0, allowed for calculation of residuals in half of layer 3, the algorithm did not have this implemented, because the other half of layer 3 was not used. This was because of the problematic chip ID 7 explained in section 3.2.
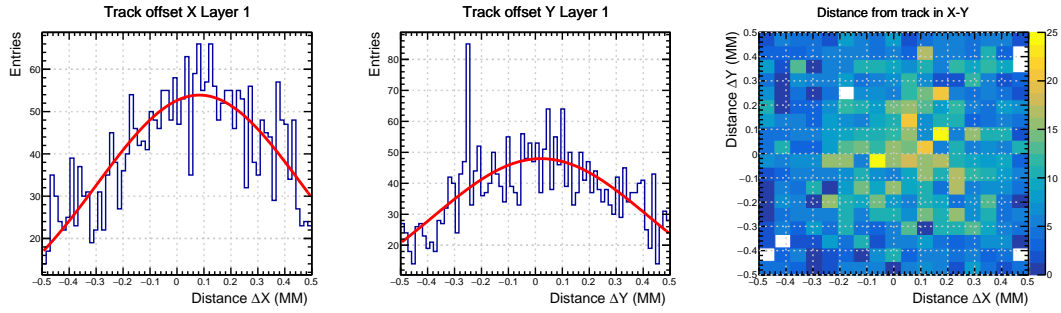
Figure 6.7: Residuals from layer 1 in x and y direction based on tracks with the angle limitation, $\phi_{max} = 8.5°$, from data taken with the Strontium-90 source which was positioned at ca. 1 mm distance from the center of chip ID 0 in layer 0.
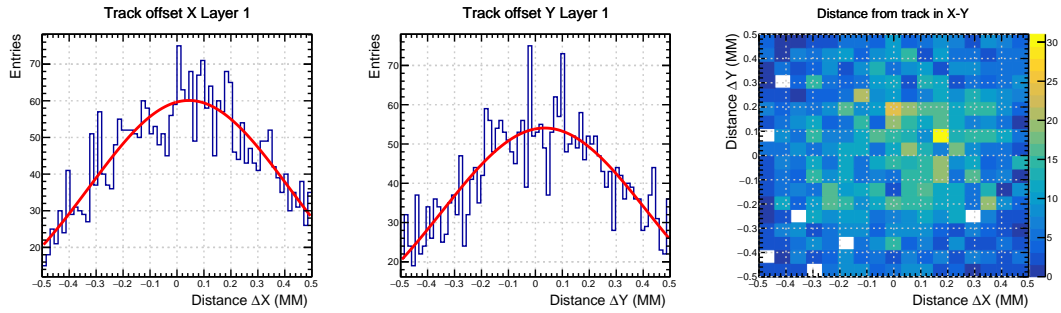
Figure 6.8: Residuals from layer 1 in x and y direction based on tracks with the angle limitation, $\phi_{max} = 8.5°$, from data taken with the Strontium-90 source which was positioned at ca. 1 mm distance from the center of chip ID 1 in layer 0.

Table 6.4: The results of the fits over the histograms of residuals in layer 1 from the data sets with the β emitting source centered over chip ID 0 and chip ID 1 above layer 0.

Sr-90 position	Layer	No. tracks	Source	ϕ_{max}	Mean_x [µm]	Variance_x [µm]	mean_y [µm]	Variance_y [µm]
Over chip ID 0	1	3864	beta	8.5°	130 ± 20	440 ± 20	40 ± 20	460 ± 20
Over chip ID 1	1	4259	beta	8.5°	90 ± 10	430 ± 10	60 ± 10	450 ± 20

Fit track finding approach

The residuals based on tracks found from the fit track finding approach for all possible layers are shown in this section. Only residuals from tracks with the angle limitation $\phi_{max} = 8.5°$ were used to produce the plots in order to reduce the width of the distribution as it was also mentioned for the results of the straight line approach. Figure 6.9 belongs to the data set where the Strontium-90 source was positioned above the center of layer 0 at the distance of ≈ 1 mm.

As shown in figure 6.9, the histograms of residuals from the data set where the Strontium-90 source was used, were fitted. The fit approach to track finding was used, which found tracks from cluster centers in layers 0, 1 and 2 and the angle limitation was kept at $\phi_{max} = 8.5°$. The purpose of the 2-dimensional histograms was to visualize the correspondence of the histograms for x and y, but this histogram and the ones like it were not used for calculation of residuals or fitting. The means and variances of fits for the different histograms from the data where the source was above the center of layer 0 are given in table 6.5. Although residuals were calculated for layer 3, the points in that layer were not used in the fit to make the tracks. In the case of the fit over the histogram for layer 3 in the y direction, the fit did not converge in multiple attempts and the mean and the variance were therefore not found. For layer 1, the means and the variances found are very similar to the ones found from the straight line approach with the same angle limitation of $\phi_{max} = 8.5°$, given in table 6.3.

Table 6.5: *The results of the fits over the histograms of residuals in all layers from the data with the β emitting source centered above layer 0. The residuals are from the fit approach to track finding.*

Layer	Mean_x [µm]	Variance_x [µm]	mean_y [µm]	Variance_y [µm]
0	-28 ± 7	172 ± 8	-21 ± 5	172 ± 6
1	60 ± 10	340 ± 10	40 ± 10	340 ± 10
2	-28 ± 7	172 ± 8	-21 ± 5	172 ± 6
3	300 ± 300	1300 ± 700	DID NOT CONVERGE	DID NOT CONVERGE

6.2.2 Residuals from cosmic muons

Straight line track finding approach

The residuals calculated based on tracks from cosmic muon detection from the straight line approach to track finding are shown in figure 6.10. The angle limitation was $\phi_{max} = 160°$. Since the width of the distribution for muons is much less than the width of the residual distribution for electrons, the x-axis only shows half the distance compared to the plots for electrons.

When including only the tracks with the angle limitation $\phi_{max} = 8.5°$, the residual plots were as shown in figure 6.11. It is clear that the width of the residual distribution reduces a lot when only tracks with the angle limitation $\phi_{max} = 8.5°$ from muons are used as opposed to $\phi_{max} = 160°$.

The mean and variance of the fit over each histogram shown in figures 6.10 and 6.11 are shown in table 6.6 with their uncertainties. The straight line approach was used to find the tracks and because of that, only residuals from the tracks in layer 1
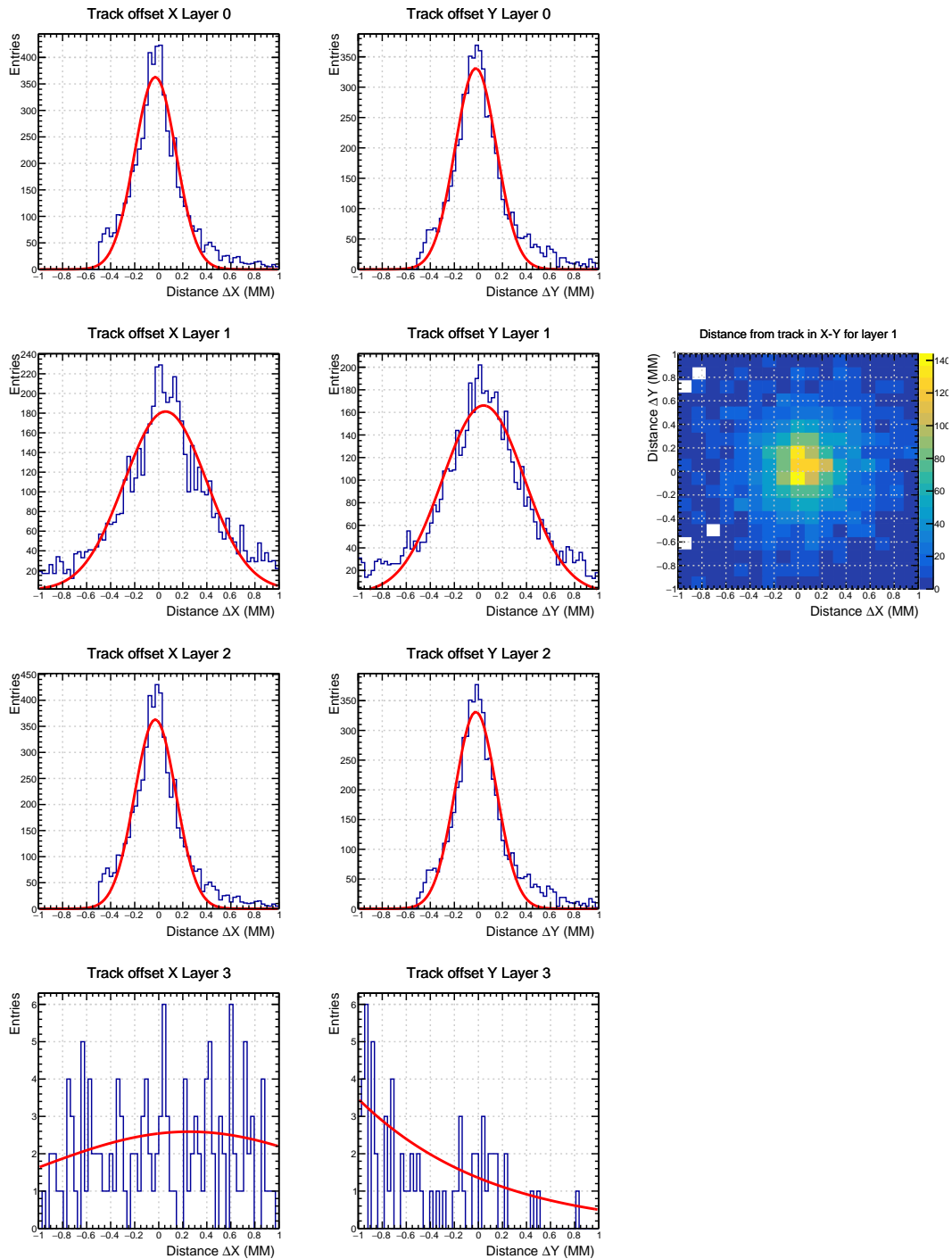
Figure 6.9: Residuals from all possible layers in x and y direction based on tracks with the angle limitation, $\phi_{max} = 8.5°$, found by the fit track finding approach in the data taken with the Strontium-90 source which was positioned at ca. 1 mm from the center of layer 0.
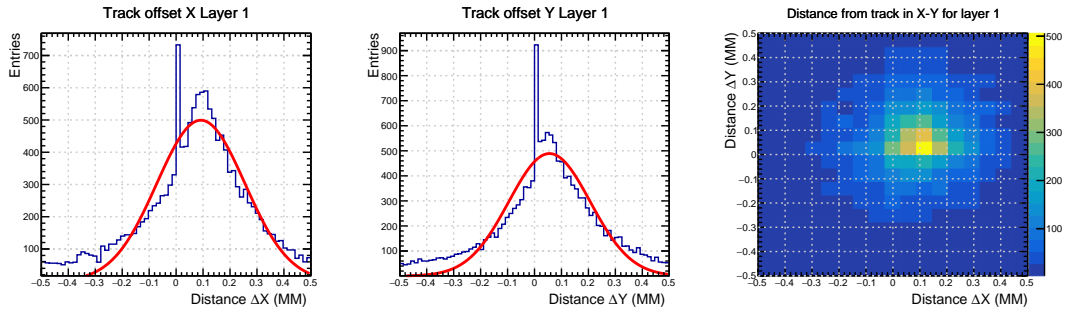
Figure 6.10: Residuals of layer 1 in x and y direction based on data from detection of cosmic muons with the angle limitation $\phi_{max} = 160°$.

Figure 6.11: Residuals of layer 1 in x and y direction based on only tracks with the angle limitation $\phi_{max} = 8.5°$ from data from detection of cosmic muons.

were calculated. The same data set was used but the angle limitation was changed between the two runs.

Table 6.6: The results of the fits over the histograms of residuals in all possible layers from the data set from cosmic muon detection from the tracks of the straight line approach.

Layer	ϕ_{max}	Mean_x [µm]	Variance_x [µm]	mean_y [µm]	Variance_y [µm]
1	160°	92 ± 7	160 ± 8	56 ± 7	150 ± 10
1	8.5°	88 ± 1	29 ± 1	58 ± 2	31 ± 2

Fit track finding approach

The residuals calculated based on the fit approach to track finding are shown in figure 6.12. For this data set, only tracks with the angle limitation $\phi_{max} = 8.5°$ were used in order to reduce the width for the residual distribution.

The histograms shown in figure 6.12 were fitted by a weighted Gaussian distribution. The means and variances for the fits shown in the figure with their uncertainties are given in table 6.7. Tracks only used cluster centers in layers 0, 1 and 2, and the residuals calculated for layers 3 were calculated even though the cluster centers of this layer were not used in the track finding using the fit approach.
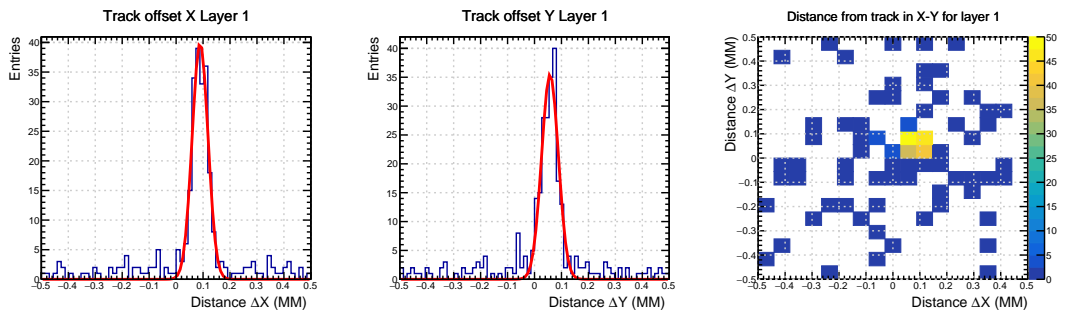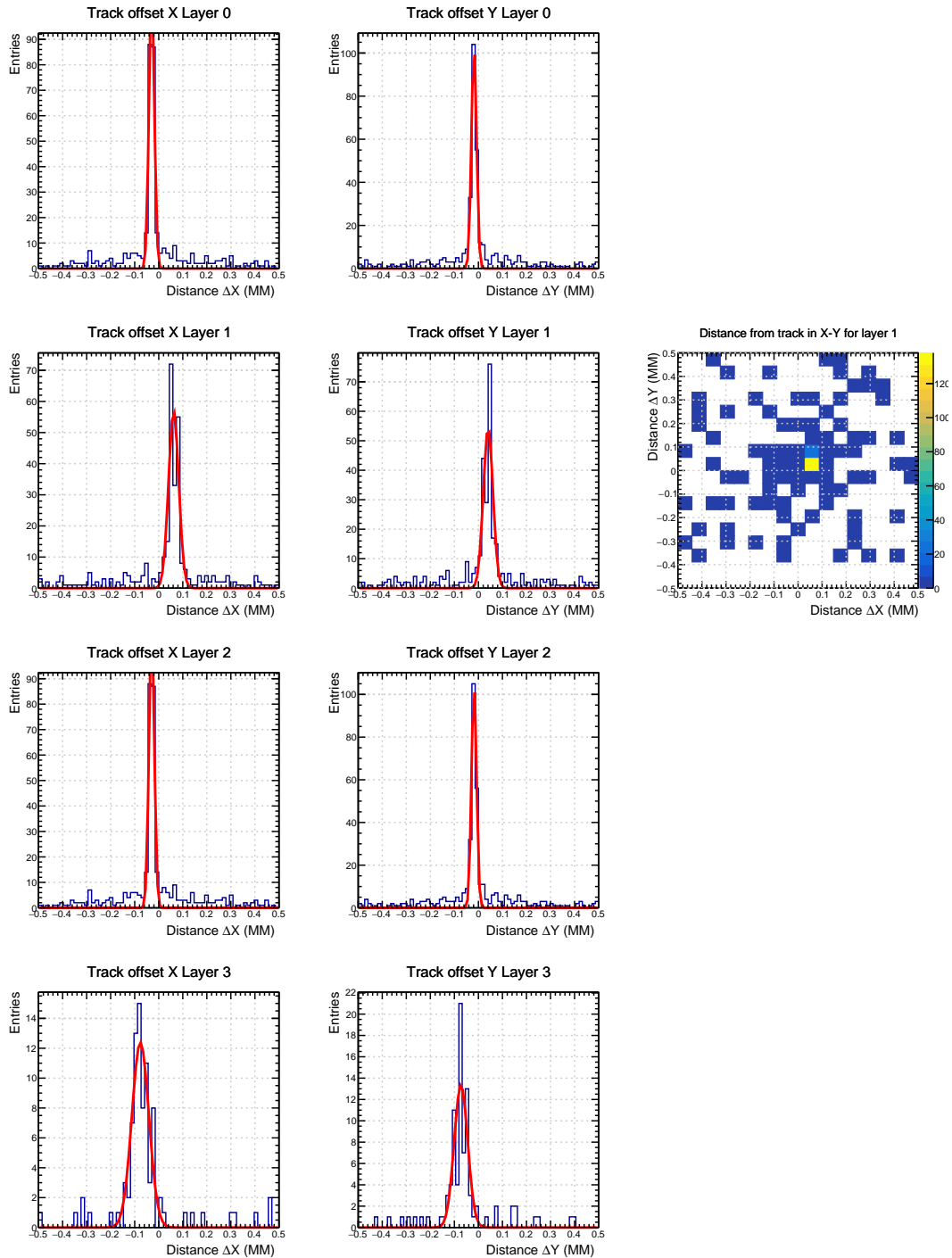
Figure 6.12: Residuals of layer 1 in x and y direction based on only tracks with the angle limitation $\phi_{max} = 8.5°$ from data from detection of cosmic muons.

Table 6.7: The results of the fits over the histograms of residuals in all possible layers from the data set from cosmic muon detection. The tracks were found using the fit approach to track finding.

Layer	Mean_x [μm]	Variance_x [μm]	mean_y [μm]	Variance_y [μm]
0	-29.5 ± 0.4	10.9 ± 0.5	-18.3 ± 0.4	10.6 ± 0.4
1	62 ± 2	21 ± 2	40 ± 2	20 ± 2
2	-29.5 ± 0.4	10.9 ± 0.5	-18.2 ± 0.4	10.4 ± 0.4
3	-76 ± 4	35 ± 6	-73 ± 5	28 ± 5

6.3 Visualization of the misalignments

The misalignments of the layers in the mTower were calculated from the different data sets. Here the most accurate results are visualized in the sketch shown in figure 6.13. As it can be seen in the figure, the distance between the left side of the line for layer 1 and the left side of the line for layer 0 and 2 are 90 μm apart. This is in agreement with the results from both track finding approaches. The straight line approach uses layer 0 and 2 as its reference coordinate system and gives the value 90 μm, and the fit track finder uses the same reference coordinate system as shown in figure 6.13 and because of that places layer 0 and 2 at about -30 μm in this coordinate system, while it places layer 1 at 60 μm. This comparison can not be done for layer 3, since it is not part of the straight line track finder in any way.
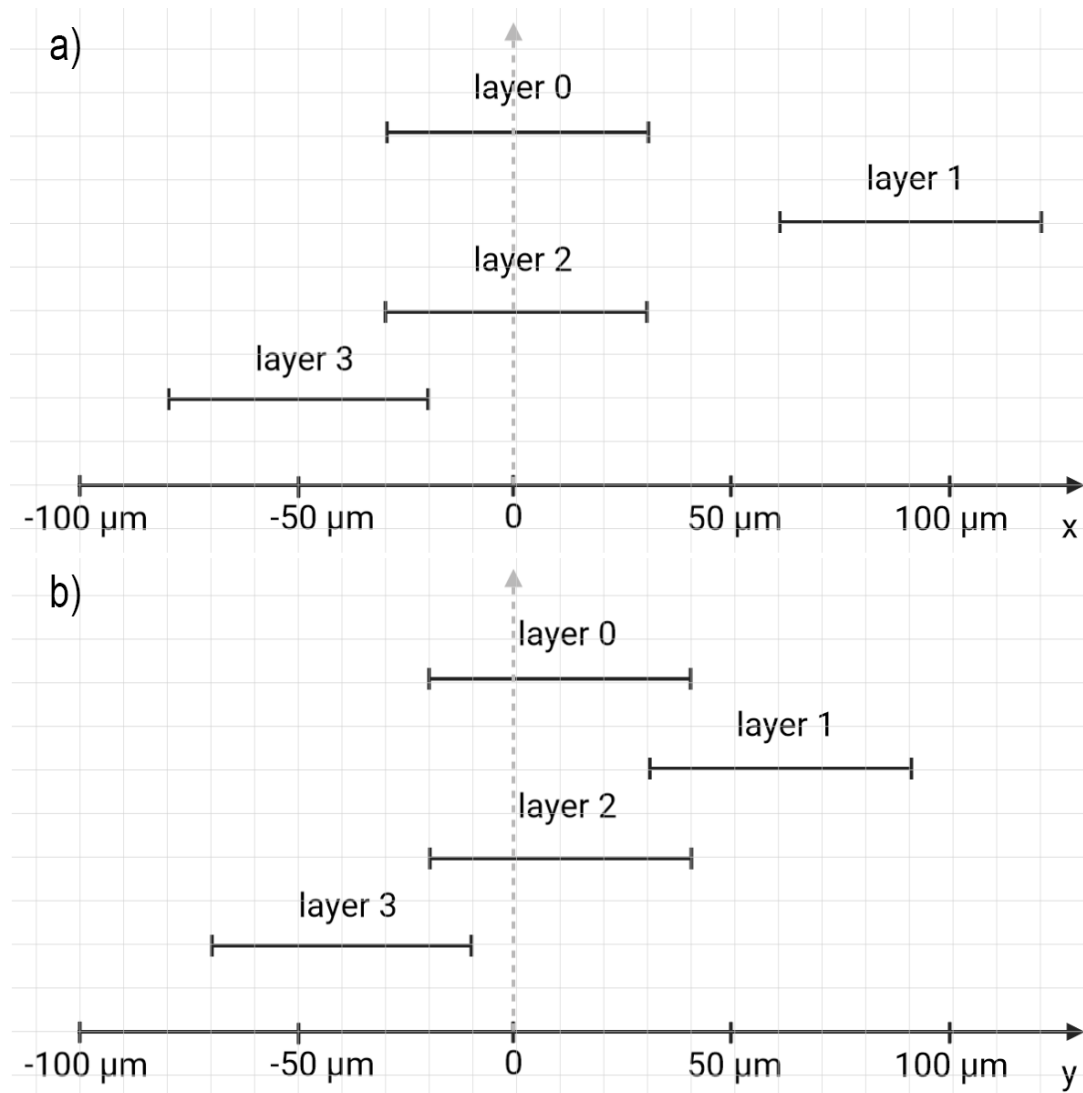
Figure 6.13: Visualization of the layer misalignments in a global coordinate system. For each layer a line with the length 60 μm is drawn, which is approximately the length of two pixels. a) Misalignments in the x-direction b) Misalignments in the y-direction. The vertical axis is not to scale and the values on the horisontal axis are rounded up to the closest 10 μm.

6.4 Discussion

The results of the track findings and the offset histograms, given that there are many tracks, show a Gaussian distribution. This was in agreement with the expectation that the radioactive decay from a β emitting source and from cosmic muons is statistical in nature. The decays in a β source results in a spherical radiation pattern and the ALPIDE chips only covered a small part of this sphere, so that with the activity of about 12 kBq, at most 304678 tracks were found with the most inclusive parameters during 10 minutes of data acquisition with the setup.

The number of tracks found from the data sets acquired with the β emitting source was much larger than the cosmic muon data. For the same number of tracks, electrons were excepted to give a wider Gaussian distribution compared to muons because of multiple Coulomb scattering and because of the lower electron energies compared to the cosmic muons. This was seen in the results.

The muon data resulted in values with much less uncertainties due to the smaller width of the Gaussian distribution as expected from the theory. The theoretical width of the distributions due to multiple Coulomb scattering, σ_{MSC}, were 1623 μm for 0.5 MeV electrons and 1.2 μm for 1 GeV muons after passing 1 layer of ALPIDEs. In addition to this, the resolution uncertainty is, $\sigma_{res} \approx \frac{30}{\sqrt{12}}$ μm, which is about 9 μm. The expected total uncertainty is given by $\sigma_{tot}^2 = \sigma_{MSC}^2 + \sigma_{res}^2$.

The expected σ_{tot} was 1623 μm for 0.5 MeV electrons and 9.1 μm for 1 GeV muons. These values are the totalt uncertainties in a perfectly aligned detector, but the values calculated for the mTower in the x-direction in layer 1 were at best 340 ± 10 μm for electrons from Strontium-90 and 21 ± 2 μm for cosmic muons. This means that the uncertainties achieved for the data from the β source were about at worst 3 times smaller than what was expected for 0.5 MeV electrons, but twice as expected for 1 GeV muons. The uncertainties for layer 0 and 2 were smaller for both radiation sources, which made the them closer to the expected uncertainties for the muons, but deviated even more for the case of the data from electrons.

Two causes can be pointed out for this deviations between the expectations and the final results. Firstly, neither the muons or the electrons were from a mono-energetic beam. Secondly, the limitation put to the distance from the track in the x and y direction was 1 mm, which itself is smaller than the expected width of the distribution for 0.5 MeV electrons. This cut removes tracks with large angle scattering and thus results in a too narrow residual distribution. In the case of muons, the measured width agrees with the expectation. These factors made it so that there were higher energetic electrons from the Strontium-90 source that did not scatter as much as electrons with 0.5 MeV energy would, and that the electron tracks that could widen the residual distribution further, were rejected. In the case of muons, the number of tracks could have been the reason for the wider distribution than the expectation.

Two approaches were used to find the particle tracks traversing the layers in the mTower. The means and variances of the residuals calculated based on these tracks and from the fit approach resulted in similar values when all parameters were the same as for the straight line approach, but layer 3 stood out in all data sets because its uncertainties of the calculated mean and variances of the residuals in that layer were at least one order of magnitude higher than the ones for the other layers. This was due to extrapolation in

that layer since the hits in layer 3 were not part of the fit used to make the tracks.

The fits over the residual histograms resulted in the mean and variance values with variations of several pixel widths, but there was agreement in the sign of the values achieved. For example, all the offset results from the different runs with the straight line track finder were positive for layer 1 in the x-direction and they ranged from 50 $\pm$ 10 µm (80 µm -30 µm to achieve the value in the global coordinate system) to 62 $\pm$ 2 µm in the global coordinate system shown in figure 6.13. The positive value of the mean of the distribution was also true for the fit approach for layer 1. There was overlap between the means of the residuals in the results from all the different data sets when adjusted for the different coordinate systems and when the uncertainties of these values are taken into account.

The residuals that were achieved from the straight line track finding approach were relative to layers 0 and 2, which can themselves be misaligned relative to each other and give a biased alignment if used. The residuals from the fit track finding approach were relative to the tracks that were found. The residuals were calculated based on cluster centers and there was no measures taken to take multiple Coulomb scattering of electrons and muons into account. The residuals calculated are therefore a combination of the misalignments of the layers and the residual values from scatterings of the particles, but as shown earlier in this discussion, for the muons, the resolution uncertainty was much bigger than the uncertainty due to multiple Coulomb scattering.

Based on the general trends in the results it can be said that the four layers are definitely not 100% aligned mechanically and software alignment is necessary. The results also make it clear that measures need to be taken to reduce the effect of multiple Coulomb scattering from the residual values, especially if low energetic particles are used for tracks. Using cosmic muons allows to disentangle the effects due to misalignment, and due to multiple Coulomb scattering and position resolution.

The main limitation of the methods used is their system of reference. Since the relative misalignments of the layers of the mTower was obtained in a local coordinate system with the ALPIDEs as the points of reference, the values cannot be directly used to adjust hits in a global coordinate system of the entire setup. The results found also lack information about the position of layers in the z direction, incident to both x and y directions for all the ALPIDEs. In the case of layer 3, before finding a fix for the non-working half with ID 7, it would be hard to compare the result with the other layers, because there is less information from this layer and that makes the uncertainties of the values for the layer higher than the other layers.

There are ways to use the algorithms developed for this thesis to find the misalignments of layers in a coordinate system that covers the entire Bergen pCT DTC. One solution would be to collimate the incoming particles and use two scintillators or pixel detectors in the collimated path so that the direction and position of the charged particle before entering the layers of the setup would be known. This way, the fitting approach to track finding would be able to find the residuals in all layers simultaneously. A sketch of this concept is shown in figure 6.14.
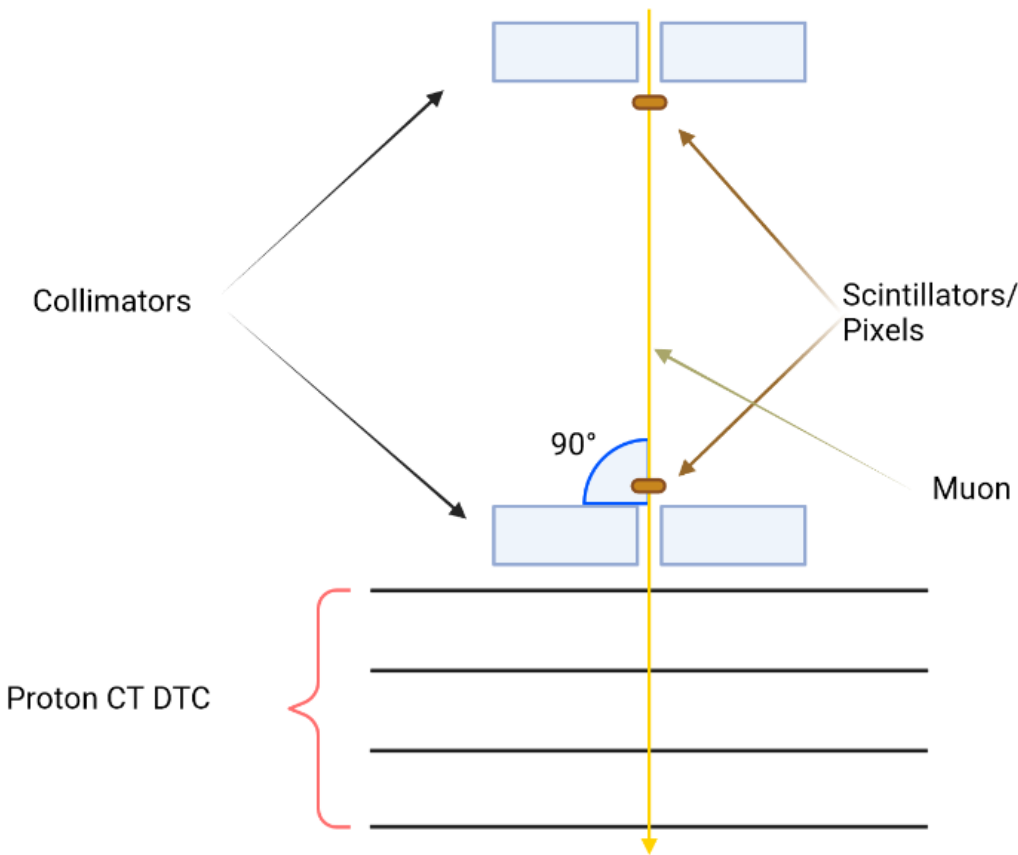
Figure 6.14: The concept of a collimated setup with scintillators for the alignment of a pCT DTC.

Chapter 7

Conclusions and future work

Data was taken with a β emitting source and from cosmic muons were detected using the mTower's ALPIDE sensors. Two track finding approaches were used, one with fixed points in two layers and one that was a fit. The residuals from the tracks found were calculated and the histograms of residuals were fitted to give the mean and the variance of the Gaussian distribution for each data set. The results were relative misalignments of layers.

Most of the results were in agreement with each other, but because of the bug at ALPIDE with ID 7, the results for layer 3 have much higher uncertainties, even in the data set from muon which gave the smallest uncertainties and smallest variances for all the layers.

The final step of aligning the layers of the mTower was not achieved because since the position of the radiation sources and the direction of the particles were not known in any other way than by what was detected by the ALPIDEs, the tracks that were found were not necessarily placed where the particle trajectories truly would have been. The concept using collimators and scintillators or an alternative therefore must be used to eliminate this uncertainty. Then the fitting approach to track finding would be able to find misalignments of all the layers in a way that all layers can be adjusted.

An alternative method of alignment is described by the Millepede II program from DESY. This program calls the parameters belonging to a track "local" parameters, and the parameters that belong to the entire system "global" parameters. It performs an overall least squares fit with all the global and local parameters from all the events in the data set to determine all of the parameters simultaneously. The way this is done is to reduce the problem of finding the misalignments to a matrix equation where the answer is found by solving a symmetric n-by-n matrix. The dimension of the matrix is given by the number of global parameters, n, irrespective of the total number of local parameters and the algorithm does this reduction without any approximations. Millepede II is both faster and more efficient than the approaches used to find the residuals in this thesis and is therefore a better choice for the alignment of the detector from Bergen pCT collaboration [35].

Appendix A

Appendix A

A.1 Activity

Current source activity is given eq.A.1:

$$A_t = A_0 \times e^{-\frac{\ln 2}{T_{1/2}} \times t} \tag{A.1}$$

Where A_t is the current activity, A_0 is the initial activity, $T_{1/2}$ is the half life and t is the time elapsed since the initial activity was measured.

A.2 Normal distribution

Normal distributions are one of the results of the central limit theorem. This theorem states that the sum of a large number of independent and random variables will approach a normal distribution. A normal distribution, also known as a Gaussian distribution, is described by its mean (μ) and standard deviation (σ) as it can be seen in eq.A.2. The mean is the value in the middle of the curve on the x-axis and the distribution is symmetrical about the line $x = \mu$. Figure A.1 shows the general normalized form of a normal distribution, which means that $\mu = 0$ and $\sigma = 1$ [36].

$$f(x; \mu, \sigma) = \frac{1}{\sqrt{2\pi}\sigma} e^{\frac{-(x-\mu)^2}{2\sigma^2}} \tag{A.2}$$
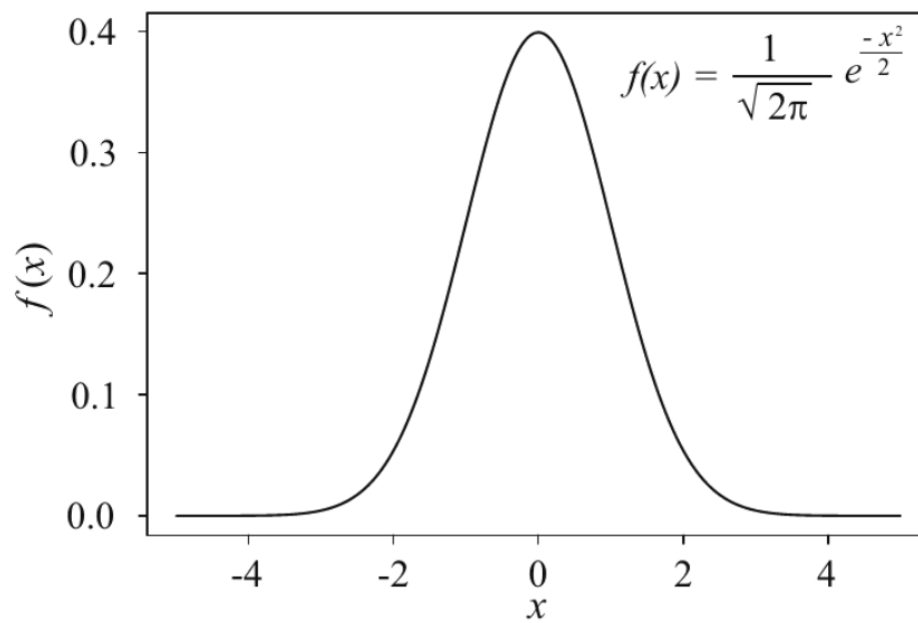
Figure A.1: A unit Gaussian distribution, a Gaussian distribution where $\mu = 0$ and $\sigma = 1$. The figure is from [36].

Appendix B

Extra plots

The plots shown in the results chapter are selected results for two of the four data sets. The plots shown in this appendix were included for the interested reader.

B.1 Hit maps

In figure B.1, the source is positioned over the center of chip ID 1. The data acquisition parameters were exactly the same as for figure 5.3 and figure 5.5 and the only difference was the source position.

A hit map of cluster center positions is shown in figure B.2. It shows that the cluster center positions correspond with the pixels that registered the most number of hits as shown in figure B.1.

B.2 Track plots

Tracks were found from all the data sets acquired with and without the source. Some of these were shown in the results chapter to show how tracks from Strontium-90 and muons were distributed in the setup and how the angle limitation affected these. Additional plots similar to the ones in that chapter are shown here.

B.2.1 Tracks from the straight line approach

Tracks from the data acquired with the Strontium-90 source above the center of chip ID 0 is shown in B.3.

Moving the source above the center of chip ID 1 resulted in the tracks shown in figure B.4. When only looking for incident tracks, 4259 tracks were found from this run.

B.2.2 Tracks from the fit approach

With an offset limit of 1 mm for both x and y directions, the fit track finding algorithm found 5838 tracks in the data with the β source (see figure B.5) and 390 in the data without the source (see figure B.8). This is when only incident tracks were found.
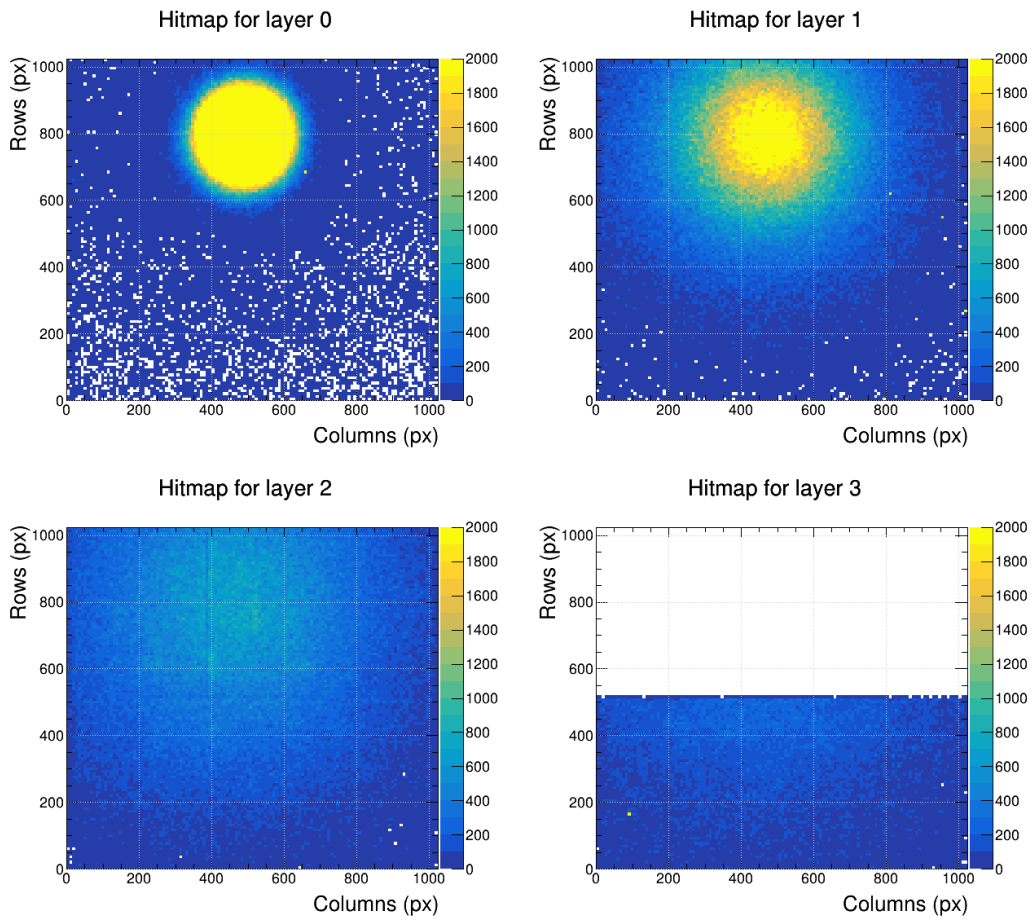
Figure B.1: Hit maps for the different layers of the mTower. Layer 3 consists of chip IDs 6 and 7, and because 7 doesn't work, it only shows half the layer. The source was ca. 1 mm away from the center of chip ID 1 on layer 0. Data acquisition lasted 10 minutes.
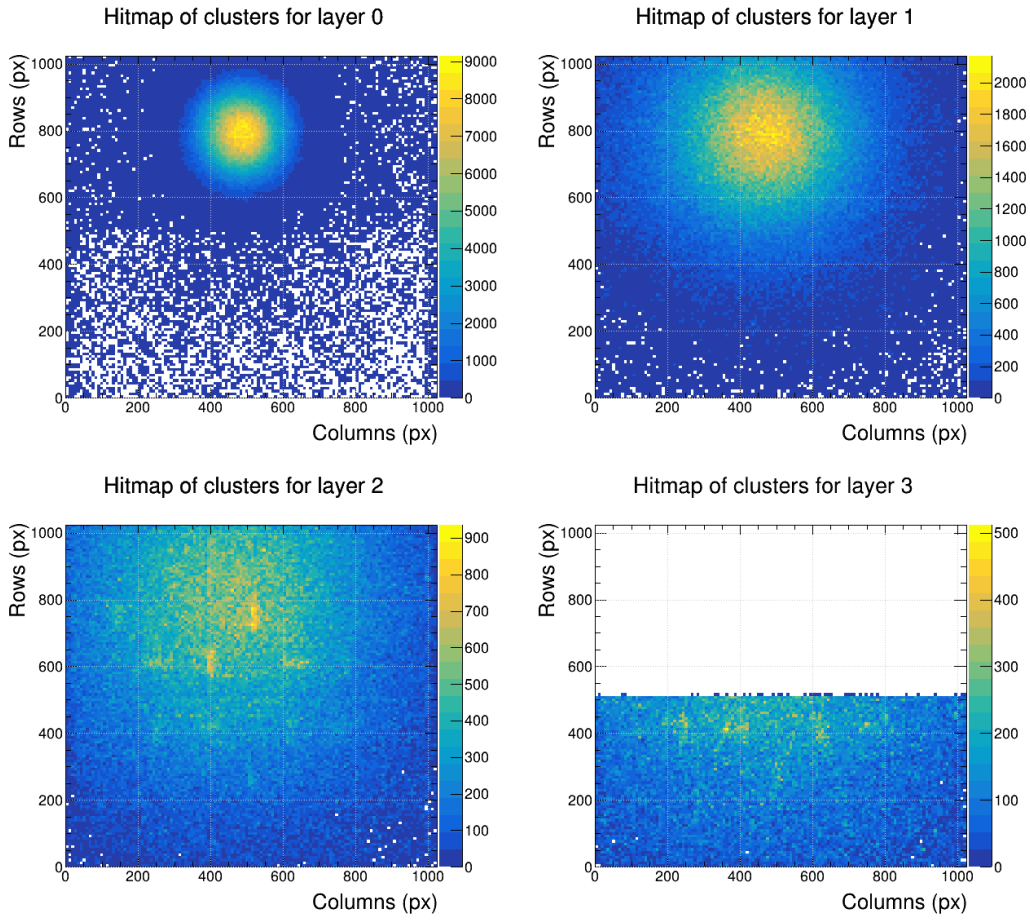
Figure B.2: Hit maps of cluster centers for the different layers of the mTower. The source was ca. 1 mm away from the center of chip ID 1 on layer 0. Data acquisition lasted 10 minutes.

Figure B.3: Plot of the first thousand tracks with $\phi_{max} = 8.5°$ found in the same data set as shown in the hit maps in figure 5.5 where the source was above the center of chip ID 0 in layer 0.
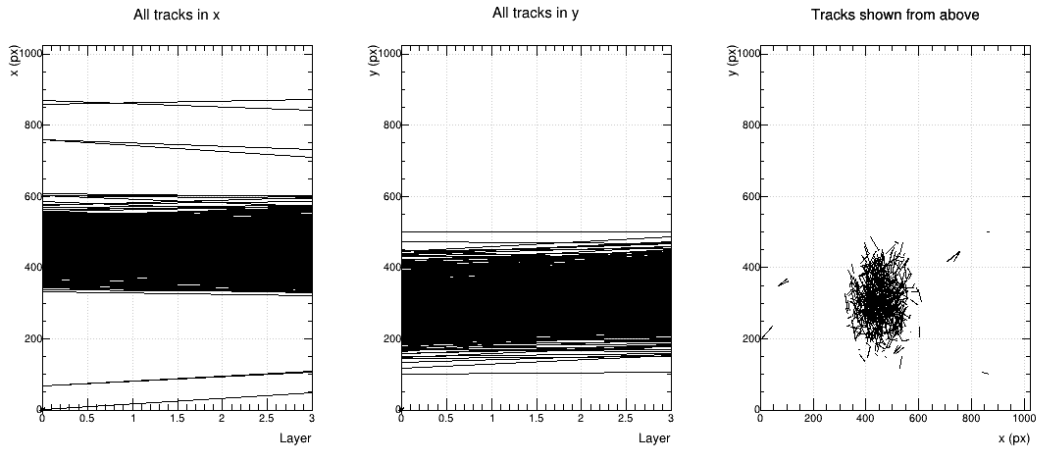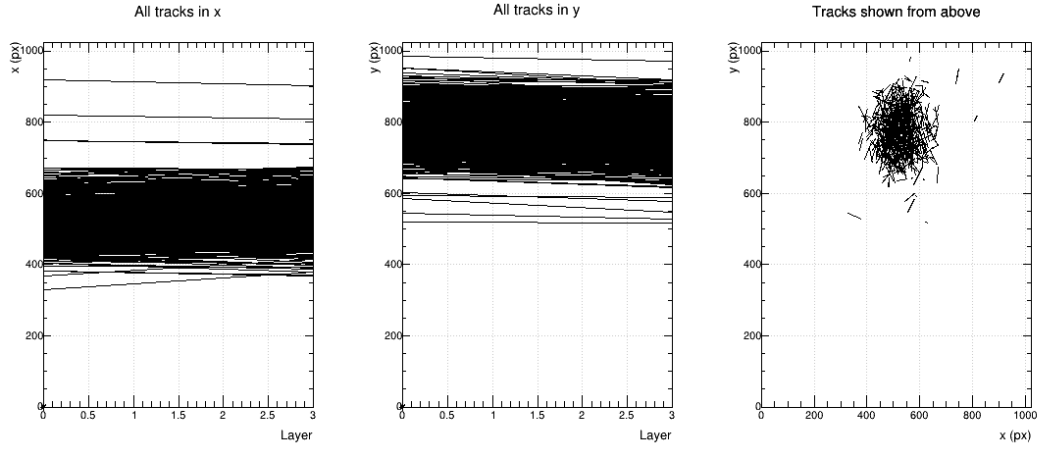
Figure B.4: Plot of the first thousand $\phi_{max} = 8.5°$ tracks found in the same data set as shown in the hit maps in figure B.1 where the source was above the center chip ID 1 in layer 0.
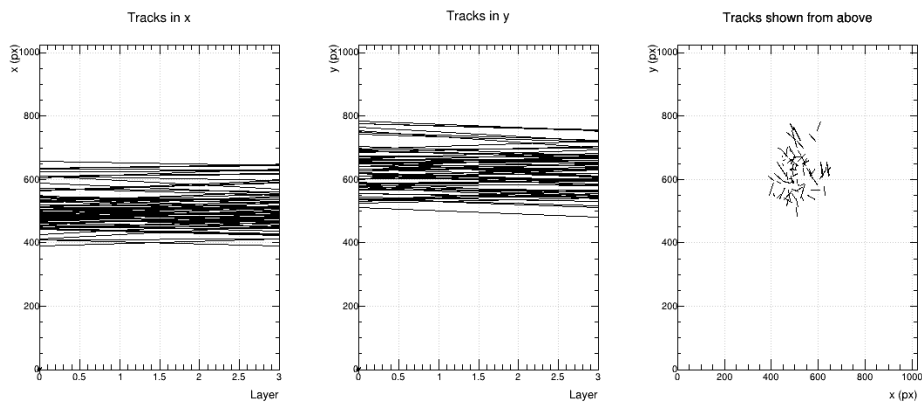

Figure B.5: The first thousand tracks found from the Strontium-90 source by the fit approach track finding algorithm. The source was centered above layer 0.
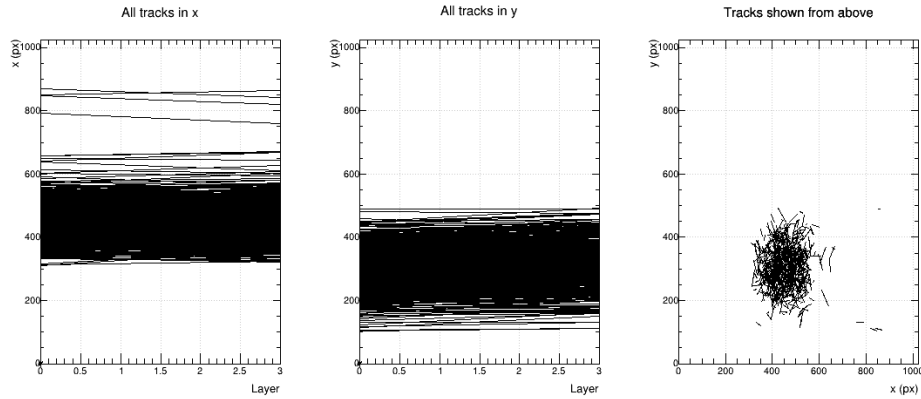
Figure B.6: The first thousand incident tracks found from the Strontium-90 source by the fit approach track finding algorithm. The source was centered above chip ID 0 in layer 0.
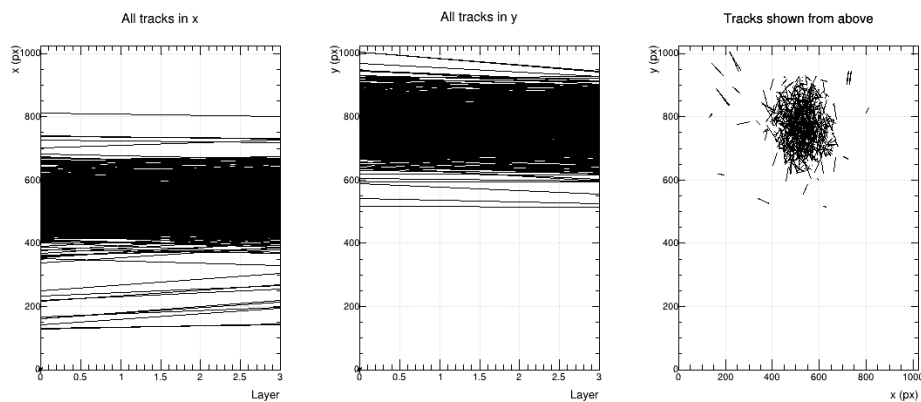

Figure B.7: The first thousand tracks found from the Strontium-90 source by the second approach track finding algorithm with $\phi_{max} = 8.5°$. The source was centered above chip ID 1 in layer 0.

Moving the Strontium-90 source above the center of the ALPIDE with chip ID 0, resulted in 5312 tracks found by the fit approach with $\phi_{max} = 8.5°$. The first thousand of these tracks are shown in figure B.6.

Moving the Strontium-90 source above the center of the ALPIDE with chip ID 0, resulted in 5871 tracks found by the fit approach with $\phi_{max} = 8.5°$. The first thousand of these tracks are shown in figure B.6.

The fit track finding approach found 390 tracks in the muon data set with $\phi_{max} = 8.5°$. These are shown in figure B.8.

B.3   Residuals

The *beta* emitting was moved to increase the number of electrons passing through one side of the mTower at a time, then tracks were found using only the data from ALPIDEs from that side of the setup. This was to see if the results would be the same between the two side. Figure B.9 belongs to the data set where the Strontium-90 source was positioned above the center of the ALPIDE with chip ID 0 in layer 0. The tracks were found only on the side of the mTower where the ALPIDEs had the IDs 0,2,4 and 6.

Figure B.10 belongs to the data set where the Strontium-90 source was positioned
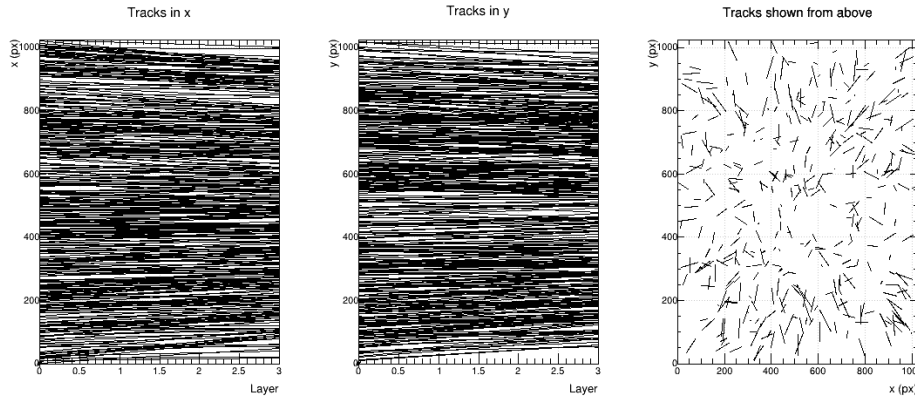
Figure B.8: The tracks found by the second approach track finding algorithm in absence of a source with $\phi_{max} = 8.5°$.

above the center of the ALPIDE with chip ID 1 in layer 0. Only the data from one side of the mTower with chip IDs 1, 3 and 5 was used to find tracks using the fit approach.

The means and variances of fits for the different histograms from the data where the source was over the center of chip ID 0 above layer 0 are given in table B.1.

Table B.1: The results of the fits over the histograms of offsets in all possible layers from the data with the β emitting source centered over chip ID 0 above layer 0. The offsets are from the fit approach to track finding.

Layer	Mean_x [μm]	Variance_x [μm]	mean_y [μm]	Variance_y [μm]
0	-46 ± 7	175 ± 8	-15 ± 6	180 ± 7
1	90 ± 10	350 ± 20	30 ± 10	360 ± 10
2	-46 ± 7	175 ± 8	-15 ± 6	180 ± 7
3	-70 ± 50	890 ± 80	-70 ± 60	1100 ± 100

The means and variances of fits for the different histograms from the data where the source was over the center of chip ID 1 above layer 0 are given in table B.2. Cluster centers in layers 0,1 and 2 on the side of the mTower with chip IDs 1,3,5 were used for track finding with the fitting approach to track finding.

Table B.2: The results of the fits over the histograms of offsets in all possible layers from the data with the β emitting source centered over chip ID 1 above layer 0. The offsets are from the fit approach to track finding.

Layer	Mean_x [μm]	Variance_x [μm]	mean_y [μm]	Variance_y [μm]
0	-35 ± 6	173 ± 7	-20 ± 6	172 ± 7
1	70 ± 10	350 ± 10	40 ± 10	340 ± 10
2	-35 ± 6	173 ± 7	-20 ± 6	172 ± 7

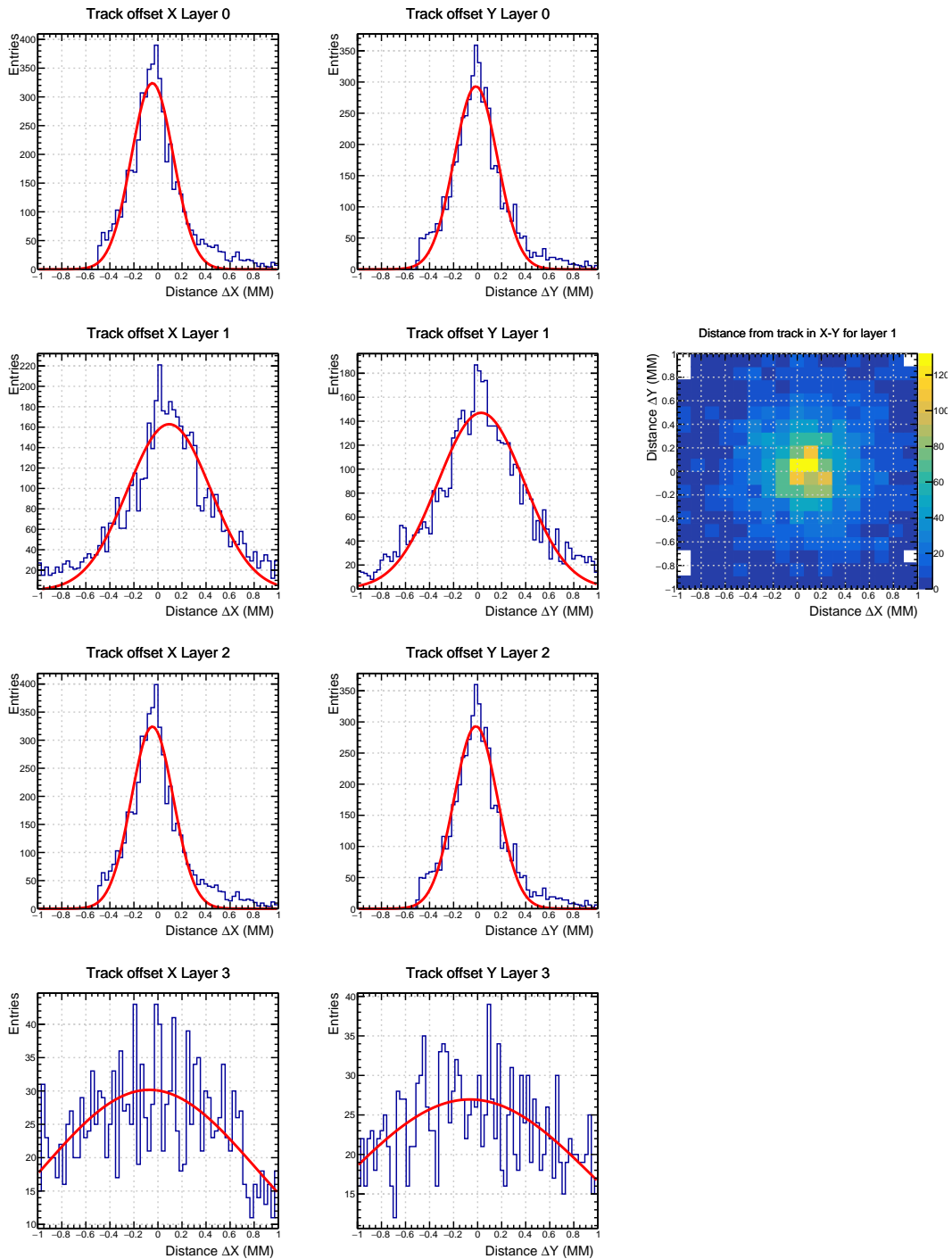*Figure B.9: Residuals of all possible layers in x and y direction based on tracks with the angle limitation, $\phi_{max} = 8.5°$, found by the fit track finding approach from data taken with the Strontium-90 source which was positioned at ca. 1 mm distance from the center of chip ID 0 in layer 0. Only the data from one side of the mTower with chip IDs 0,2,4 and 6 is used.*

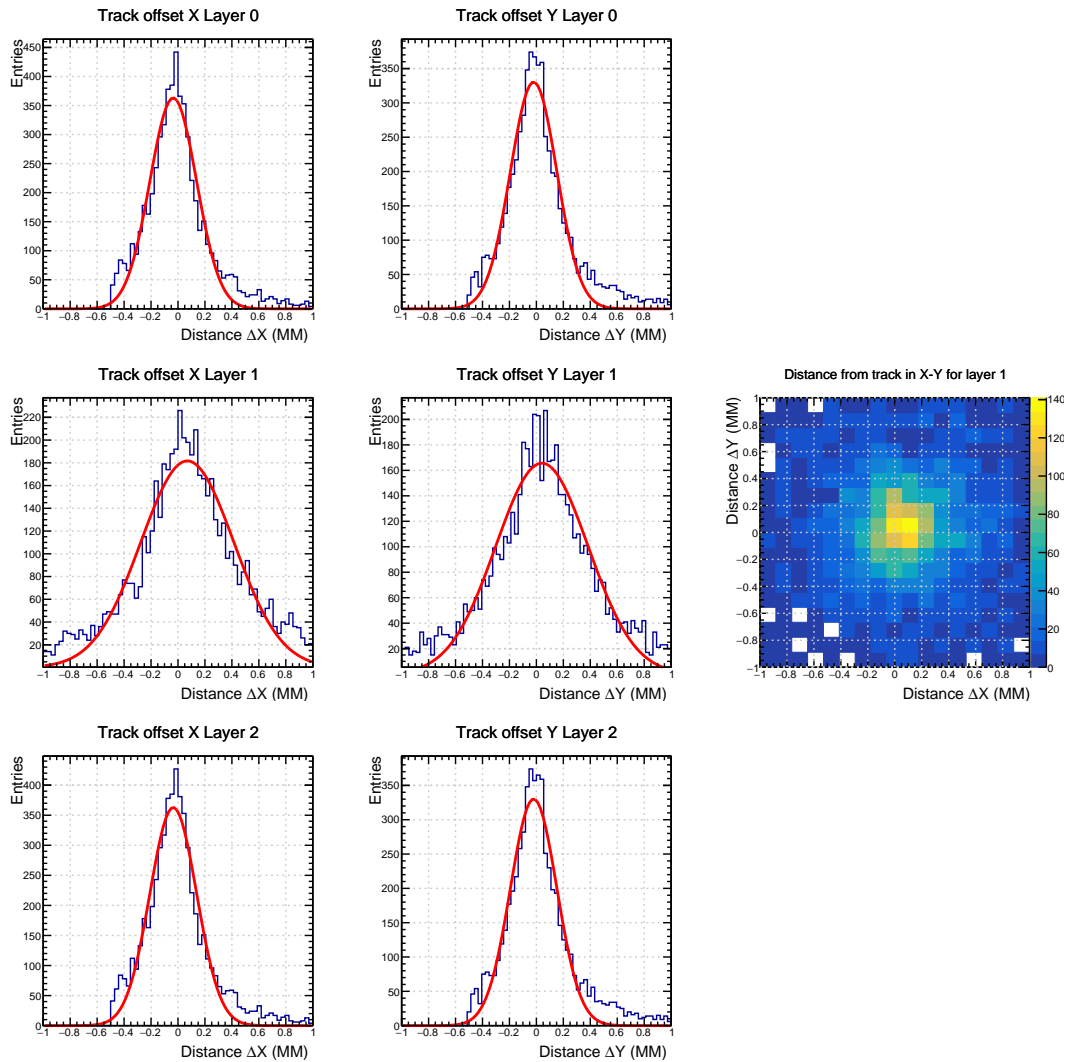*Figure B.10: Residuals in x and y direction for all layers based on tracks with the angle limitation $\phi_{max} = 8.5°$ from data taken with the Strontium-90 source which was positioned at ca. 1 mm distance from the center of chip ID 1 in layer 0 were found by the fit track finding approach. Only the data from one side of the mTower with chip IDs 1, 3 and 5 was used.*

Bibliography

[1] Norwegian Government. *Etablering av Protonsentre i Bergen og Oslo, [Eng.: Establishment of Proton Centers in Bergen and Oslo]*. 2017. [online] URL (visited on 26/4/2023).

[2] J. Alme et al. "A High-Granularity Digital Tracking Calorimeter Optimized for Proton CT". In: *Frontiers in Physics* 8 (2020), p. 568243. DOI: 10.3389/fphy.2020.568243.

[3] W. R. Leo. *Techniques for nuclear and particle physics experiments: a how-to approach*. Springer Science & Business Media, 2012. ISBN: 978-3-642-57920-2.

[4] R. L. Workman et al. "Review of Particle Physics". In: *PTEP* 2022 (2022), p. 083C01. DOI: 10.1093/ptep/ptac097.

[5] C. Amsler et al. *Physics Letters B667, 1 (2008) and 2009 partial update for the 2010 edition*. 2009. [online] URL (visited on 16/4/2023).

[6] H. Paganetti. *Proton Beam Therapy*. 2399-2891. IOP Publishing, 2017. ISBN: 978-0-7503-1370-4. DOI: 10.1088/978-0-7503-1370-4.

[7] D. R. Grimes, D. R. Warren, and M. Partridge. "An Approximate Analytical Solution of the Bethe Equation for Charged Particles in the Radiotherapeutic Energy Range". In: *Scientific Reports* 7.1 (2017), p. 9781. DOI: 10.1038/s41598-017-10554-0.

[8] H. Kumada. "Accelerator Systems for Proton Radiotherapy". In: *Proton Beam Radiotherapy: Physics and Biology*. Ed. by K. Tsuboi, T. Sakae, and A. Gerelchuluun. Singapore: Springer Singapore, 2020, pp. 85–96. ISBN: 978-981-13-7454-8. DOI: 10.1007/978-981-13-7454-8_8.

[9] N. B. Smith and A. Webb. *Introduction to Medical Imaging: Physics, Engineering and Clinical Applications*. Cambridge University Press, 2010. ISBN: 978-0-521-19065-7.

[10] G. Poludniowski, N. Allinson, and P. Evans. "Proton Radiography and Tomography with Application to Proton Therapy". In: *The British journal of radiology* 88.1053 (2015), p. 20150134. DOI: 10.1259/bjr.20150134.

[11] D. R. C. Röhrich. *Private communications*. 2022.

[12] ALICE-ITS ALPIDE development team. *ALPIDE operations manual*. version 0.3, DRAFT. 2015. [online] URL (visited on 9/4/2023).

[13] O. S. Grøttvik. "Design and Implementation of a High-Speed Readout and Control System for a Digital Tracking Calorimeter for proton CT". PhD thesis. University of Bergen, 2021. [online] URL.

[14] *Users Guide for UG1224 (v1.5) for AMD Virtex UltraScale+ FPGA VCU118 Evaluation Kit*. 2023. [online] URL (visited on 2/5/2023).

[15] Aim-T.T.I. *Data sheet for QL series II DC Power Supplies*. [online] URL (visited on 2/5/2023).

[16] T. Bodova. *Private communications*. 2022.

[17] N. H. Sabah. *Electronics : Basic, Analog, and Digital with PSpice*. First edition. Boca Raton, FL: CRC Press, 2010, pp. 105–107. ISBN: 978-1-4200-8707-9.

[18] E. Tutorials. *PN Junction Theory*. [online] URL (visited on 15/5/2023).

[19] R. Turchetta et al. "CMOS Monolithic Active Pixel Sensors (MAPS): Developments and future outlook". In: *Nuclear Instruments and Methods in Physics Research Section A: Accelerators, Spectrometers, Detectors and Associated Equipment* 582.3 (2007). VERTEX 2006, pp. 866–870. ISSN: 0168-9002. DOI: 10.1016/j.nima.2007.07.112.

[20] L. Rossi et al. *Pixel detectors: From fundamentals to applications*. Springer Science & Business Media, 2006. ISBN: 978-3-540-28332-4. DOI: 10.1007/3-540-28333-1.

[21] B. Abelev et al. *Technical Design Report for the Upgrade of the ALICE Inner Tracking System*. Tech. rep. 8. ALICE Collaboration, 2014, p. 087002. DOI: 10.1088/0954-3899/41/8/087002.

[22] L. Maczewski. "Measurements and Simulations of MAPS (Monolithic Active Pixel Sensors) Response to Charged Particles - a Study Towards a Vertex Detector at the ILC". In: *arXiv preprint arXiv:1005.3710* (2010). DOI: 10.48550/arXiv.1005.3710.

[23] V. N. Eikeland. "Characterization of the ALPIDE Detector with Proton Beams for the Development of a Prototype Computed Tomography Machine at the University of Bergen". MA thesis. University of Bergen, 2018. [online] URL.

[24] M. Mager and ALICE collaboration. "ALPIDE, the Monolithic Active Pixel Sensor for the ALICE ITS Upgrade". In: *Nuclear Instruments and Methods in Physics Research Section A: Accelerators, Spectrometers, Detectors and Associated Equipment* 824 (2016). Frontier Detectors for Frontier Physics: Proceedings of the 13th Pisa Meeting on Advanced Detectors, pp. 434–438. ISSN: 0168-9002. DOI: 10.1016/j.nima.2015.09.057.

[25] G. A. Rinella, ALICE collaboration, et al. "The ALPIDE pixel sensor chip for the upgrade of the ALICE Inner Tracking System". In: *Nuclear Instruments and Methods in Physics Research Section A: Accelerators, Spectrometers, Detectors and Associated Equipment* 845 (2017), pp. 583–587. DOI: 10.1016/j.nima.2016.05.016.

[26] J. Alme et al. "Performance of the electromagnetic pixel calorimeter prototype Epical-2". In: *Journal of Instrumentation* 18.01 (2023), P01038. DOI: 10.1088/1748-0221/18/01/P01038.

[27] R. Brun and F. Rademakers. *ROOT - An Object Oriented Data Analysis Framework*. Proceedings AIHENP'96 Workshop, Lausanne, Sep. 1996, v6.26/6. 2022. DOI: 10.5281/zenodo.3895860.

[28] Bergen PCT Collaboration. *Production Tests Repository for Bergen PCT*. https://git.app.uib.no/Alfred.Abbasi/production_tests/-/tree/dev_alfred?ref_type=heads. Password protected. 2023.

[29] Bergen PCT Collaboration. *Wiki for the proton CT project*. [online] URL (visited on 28/4/2023).

[30] J. Nam et al. "Study on the Characteristics of a Scintillator for Beta-ray Detection using Epoxy Resin". In: *EPJ Web of Conferences* 153 (2017), p. 07005. DOI: 10.1051/epjconf/201715307005.

[31] M. Berger et al. *ESTAR: Stopping Power and Range Tables for Electrons*. National Institute of Standards and Technology (NIST). 2017. DOI: 10.18434/T4NC7P.

[32] F. Cuna et al. "A 103 drift velocity monitoring chamber". In: *Journal of Instrumentation* 15.09 (2020), p. C09007. DOI: 10.1088/1748-0221/15/09/C09007.

[33] G. Bonomi et al. "Applications of cosmic-ray muons". In: *Progress in Particle and Nuclear Physics* 112 (2020), p. 103768. ISSN: 0146-6410. DOI: 10.1016/j.ppnp.2020.103768.

[34] M. Tanabashi et al. "Review of Particle Physics". In: *Physical Review D* 98.3 (2018). Particle Data Group Collaboration, pp. 1–1898. DOI: 10.1103/PhysRevD.98.030001.

[35] V. Blobel. *Millepede II - Draft Manual*. 2007. [online] URL (visited on 11/6/2023).

[36] O. Behnke et al. *Data Analysis in High Energy Physics: a Practical Guide to Statistical Methods*. John Wiley & Sons, 2013. ISBN: 3-527-65343-0.